Sensitivity Calculation Based on the Adjoint Variable Method for the Transient Nonlinear Electroquasistatic-Thermal HVDC Cable Joint Problem

TECHNISCHE UNIVERSITÄT DARMSTADT

Electrical Engineering and Information Technology Department

Sensitivity Calculation Based on the Adjoint Variable Method for the Transient Nonlinear
Electroquasistatic-Thermal HVDC Cable Joint Problem

Accepted doctoral thesis by Maren Greta Ruppert-Schmidt

Date of submission: 24.06.2024
Date of thesis defense: 20.11.2024

Darmstadt, Technische Universität Darmstadt

Erklärungen laut Promotionsordnung

§ 8 Abs. 1 lit. c PromO

Ich versichere hiermit, dass die elektronische Version meiner Dissertation mit der schriftlichen Version übereinstimmt.

§ 8 Abs. 1 lit. d PromO

Ich versichere hiermit, dass zu einem vorherigen Zeitpunkt noch keine Promotion versucht wurde. In diesem Fall sind nähere Angaben über Zeitpunkt, Hochschule, Dissertationsthema und Ergebnis dieses Versuchs mitzuteilen.

§ 9 Abs. 1 PromO

Ich versichere hiermit, dass die vorliegende Dissertation selbstständig und nur unter Verwendung der angegebenen Quellen verfasst wurde.

§ 9 Abs. 2 PromO

Die Arbeit hat bisher noch nicht zu Prüfungszwecken gedient.

Darmstadt, 24.06.2024

_____

Maren Greta Ruppert-Schmidt

Danksagung

Abstract

Germany's transition to green energy requires new transmission infrastructure, including underground High-Voltage Direct Current (HVDC) technology. HVDC cable joints, which interconnect cable segments, are the most vulnerable part of these systems due to installation errors and electric field stresses. Since the length of individual cable segments is limited to 1.5–2 km due to transportation constraints, a large number of cable joints is required. As a result, the reliability of these joints is critical to the overall performance of the system. This dissertation contributes to enhancing the reliability of HVDC cable joints by developing simulation tools aimed at facilitating future advancements in joint design and reliability assessment.

The dissertation begins with a discussion on electrothermal modeling of HVDC cable joints during steady-state and transient operations. A freely available electrothermal solver is implemented, specifically tailored for HVDC cable joint simulation. The solver addresses challenges such as field- and temperature-dependent material properties and the multi-rate nature of the transient electrothermal problem. It is validated against commercial software using a 320 kV HVDC cable joint specimen, with brief analyses conducted for both steady-state and transient operations.

The dissertation focuses on developing simulation tools for efficient sensitivity computation, which are vital for design and optimization. Two complementary methods for sensitivity computation are implemented: the direct sensitivity method, which scales with the number of investigated design parameters, and the adjoint variable method, which scales with the number of investigated quantities of interest but is independent of the number of design parameters. The derivation of the adjoint variable method for transient electroquasistatic-thermal problems represents a core contribution of this thesis.

The dissertation also demonstrates how simulation can estimate model parameters from experimental data using an inverse problem approach, highlighting the role of measurement data quality. It discusses factors such as measurement sensitivity, data points, and noise corruption.

Finally, the dissertation provides a comprehensive literature review on modeling and simulation approaches for slow polarization processes in HVDC cable joints. This chapter reviews various methodologies from the literature, aiming to enhance the accuracy of

simulations and analyses for HVDC insulation systems exposed to prolonged unidirectional electric fields.

By providing tools for simulation-aided design, this dissertation aims to enable more effective and reliable approaches to HVDC cable joint development. In doing so, it supports the broader goal of improving energy transmission infrastructure and contributing to a stable and sustainable energy supply.

Abstract

Deutschlands Umstellung auf erneuerbare Energien erfordert eine moderne Übertragungsinfrastruktur, einschließlich der Nutzung unterirdischer Hochspannungs-Gleichstrom-Übertragungs (HGÜ)-Technologie. HGÜ-Kabelmuffen, welche Kabelsegmente miteinander verbinden, sind aufgrund von Installationsfehlern und elektrischen Feldbelastungen die fehleranfälligsten Komponenten dieser Systeme. Da die Länge einzelner Kabelsegmente aufgrund von Transportbeschränkungen auf 1.5–2 km begrenzt ist, ist eine große Anzahl von Kabelmuffen erforderlich. Daher ist die Zuverlässigkeit der Kabelmuffen entscheidend für die Zuverlässigkeit des Gesamtsystems. Diese Dissertation trägt durch die Entwicklung von Simulationswerkzeugen, welche künftige Fortschritte im Design robuster Kabelmuffen ermöglichen, zur Verbesserung der Zuverlässigkeit von HGÜ-Kabelmuffen bei.

Zu Beginn wird eine elektrothermische Modellierung von HGÜ-Kabelmuffen im stationären und transienten Betrieb vorgestellt. Ein eigens entwickelter, frei verfügbarer elektrothermischer Löser wird eingeführt, der speziell auf die Herausforderungen der HGÜ-Simulation zugeschnitten ist, wie z.B. feld- und temperaturabhängige Materialeigenschaften und stark unterschiedliche elektrische und thermische Zeitskalen. Dieser Löser wird am Beispiel einer 320 kV-HGÜ-Kabelmuffe validiert und eine kurze Analyse des elektrothermischen Verhaltens vorgestellt.

Ein Schwerpunkt der Dissertation liegt auf der Entwicklung von Simulationswerkzeugen zur effizienten Berechnung von Sensitivitäten, die für das Design und die Optimierung von Kabelmuffen unerlässlich sind. Zwei komplementäre Methoden werden vorgestellt: die direkte Sensitivitätsmethode, die mit der Anzahl der untersuchten Designparameter skaliert, und die adjungierte Methode, die mit der Anzahl der untersuchten Zielgrößen skaliert, aber unabhängig von der Anzahl der Designparameter ist. Die Herleitung der adjungierten Methode für transiente elektrothermische Probleme ist ein wesentlicher Beitrag dieser Arbeit.

Zusätzlich wird gezeigt, wie durch Simulationen Modellparameter aus experimentellen Daten mittels inverser Probleme ermittelt werden können. Dabei wird die Bedeutung der Messdatenqualität betont und es werden Faktoren wie Messsensitivität, Anzahl der Datenpunkte und Rauschverfälschung diskutiert.

Abschließend bietet die Dissertation einen umfassenden Literaturüberblick über beste-

hende Modellierungs- und Simulationsansätze für langsame Polarisationsprozesse in HGÜ-Kabelmuffen. Ziel ist es, die Genauigkeit der Simulationen und Analysen für HGÜ-Isolationssysteme unter langanhaltenden unidirektionalen elektrischen Feldern zu verbessern.

Durch die Bereitstellung von Werkzeugen für simulationsgestützte Designverfahren zielt diese Dissertation darauf ab, effektivere und zuverlässigere Ansätze für die Entwicklung von HGÜ-Kabelmuffen zu ermöglichen. Damit unterstützt sie das übergeordnete Ziel einer stabilen und nachhaltigen Energieversorgung.

Contents

Abbreviations, Acronyms and Symbols

Abbreviations and Acronyms

1D one-dimensional

2D two-dimensional

3D three-dimensional

AC alternating current

AVM adjoint variable method

DC direct current

DoF degrees of freedom

DSM direct sensitivity method

EPDM ethylene propylene diene monomer

EQS electroquasistatic

EQST electroquasistatic-thermal

FE Finite Element

FEM Finite Element Method

FGM field grading material

HV high voltage

HVAC high voltage alternating current

HVDC high voltage direct current

PDE partial differential equation

PNP Poisson-Nernst-Planck

PDC Polarization-Depolarization-Current

QoI quantity of interest

SiR silicone rubber

XLPE cross-linked polyethylene

Symbols

A	finite element operator; definition see (6.30a)
B	finite element operator; definition see (8.22)

c_p	specific heat capacity
c_V	volumetric heat capacity
$\boldsymbol{D}$	electric displacement field
$\mathrm{d}\Omega$	differential volume element
$\mathbf{d}\boldsymbol{S}$	differential surface element
$\mathrm{d}t$	differential time step
δ	Dirac function
Δt	time step size
Δt_el	electric time step size
Δt_th	thermal time step size
$\boldsymbol{E}$	electric field
E	electric field strength
E_z	z-component of the electric field
E_ϱ	ϱ-component of the electric field
e_rel	relative deviation
ε	permittivity
ε_r	relative permittivity
$\bar{\bar{\varepsilon}}_\mathrm{d}$	differential permittivity tensor
ε_0	vacuum permittivity
ϕ	electric scalar potential
ϕ_0	initial condition of ϕ
ϕ_fixed	Dirichlet potential at $\Gamma_\mathrm{D,el}$

φ	angular coordinate
G_k	k-th quantity of interest
$\Delta G_{1\%,j}$	normalized sensitivity
g_k	functional defining G_k
$\Gamma_{\mathrm{D,el}}$	electric Dirichlet boundary
$\Gamma_{\mathrm{D,th}}$	thermal Dirichlet boundary
$\Gamma_{\mathrm{N,el}}$	electric Neumann boundary
$\Gamma_{\mathrm{N,el}}$	thermal Neumann boundary
Γ	Gamma function
$\boldsymbol{J}$	electric current density
$\boldsymbol{J}_{\mathrm{n,fixed}}$	normal current density at $\Gamma_{\mathrm{N,el}}$
$\boldsymbol{J}_{\mathrm{tot}}$	total current density
$\boldsymbol{J}_{\mathrm{C}}$	conduction current density
$\boldsymbol{J}_{\mathrm{D}}$	displacement current density
$\boldsymbol{J}_{\mathrm{ext}}$	extended current density
$\boldsymbol{J}_{\mathrm{P}}$	polarization current density
$\boldsymbol{J}_k$	polarization current density of the k-th polarization process
$\boldsymbol{K}$	stiffness matrix; definition see (4.9)
λ	thermal conductivity
$\boldsymbol{M}$	mass matrix; definition see (5.7)
N_i	i-th nodal shape function
N_{node}	number of mesh nodes

$\boldsymbol{n}_{\mathrm{el}}$	unit vector at $\Gamma_{\mathrm{N,el}}$
$\boldsymbol{n}_{\mathrm{th}}$	unit vector at $\Gamma_{\mathrm{N,th}}$
Ω	computational domain
$\partial\Omega$	boundary of the computational domain
p_{Joule}	Joule loss density
p_j	j-tj design parameter
$\boldsymbol{p}$	vector of design parameters
$\boldsymbol{p}_0$	currently implemented parameter configuration
$\boldsymbol{P}$	dielectric polarization
$\boldsymbol{P}_k$	k-th polarization process
$\dot{\boldsymbol{q}}$	heat flux density
$\boldsymbol{r}$	position vector
ϱ	radial coordinate
ρ	density
σ	electric conductivity
$\overline{\overline{\sigma}}_{\mathrm{d}}$	differential conductivity tensor
σ_{FGM}	electric conductivity of the field grading material
$\boldsymbol{s}$	load vector; definition see (4.10)
t	time
t_{s}	initial simulation time
t_{f}	final simulation time
t_{rise}	time at which the switching impulse peaks

$t_{\text{rise},50\%}$	time at which the switching impulse rises to 50% of its peak voltage
$t_{\text{fall},50\%}$	time at which the switching impulse has declined to 50% of its peak voltage
θ	temperature
θ_{fixed}	Dirichlet temperature at $\Gamma_{\text{D,th}}$
θ_0	initial condition of θ
τ_k	time constant of the k-th polarization process
U_{switch}	switching impulse voltage
u_i	i-th degree of freedom of the finite element approximation of ϕ
u_i'	i-th degree of freedom of the finite element approximation of the sensitivity of ϕ
$\boldsymbol{u}$	vector of degrees of freedom of finite element approximation of ϕ
$\boldsymbol{u}'$	vector of degree of freedom of the finite element approximation of ϕ'
v_i	i-th degree of freedom of the finite element approximation of θ
$\boldsymbol{v}$	vector of degrees of freedom of finite element approximation of θ
$w_{\text{el},k}$	k-th electric adjoint variable
$w_{\text{th},k}$	k-th thermal adjoint variable
$w_{\text{el},k,i}$	i-th degree of freedom of finite element approximation of $w_{\text{el},k}$
$\boldsymbol{w}_{\text{el},\boldsymbol{k}}$	vector of degrees of freedom of finite element approximation of $w_{\text{el},k}$
$w_{\text{th},k,i}$	i-th degree of freedom of finite element approximation of $w_{\text{th},k}$
$\boldsymbol{w}_{\text{th},\boldsymbol{k}}$	vector of degrees of freedom of finite element approximation of $w_{\text{th},k}$
$\boldsymbol{x}_{\text{el}}$	right hand side of adjoint problem; definition see (6.30b)
$\boldsymbol{x}_{\text{th}}$	right hand side of adjoint problem; definition see (6.30c)
$\boldsymbol{X}$	finite element operator of the Debye-FEM approach; definition see (8.21)

z z-coordinate

z_i i-th Raviart-Thomas shape function

1 Introduction

1.1 Motivation

The transition to green energy is a critical component of Germany's strategy to combat climate change and achieve sustainable energy independence. Central to this strategy is the Energiewende, a policy initiative aimed at transforming the country's energy system. Key targets outlined in the Energy Expansion Act (EEA) include significant increases in renewable energy production, with a particular emphasis on wind energy [1]. The northern part of Germany, with its favorable wind conditions, is poised to play a leading role in this energy transition [2, 3]. However, the integration of wind energy on a large scale necessitates the development of new transmission infrastructure to transport the electric power from the north to other parts of the country [4, 3]. High voltage direct current (HVDC) technology has been identified as the most efficient method for long-distance power transmission, motivating the decision for several new HVDC transmission lines (see Fig. 1.1) [5, 6, 3, 4].

In 2015, a significant political choice was made to prioritize underground cable systems over overhead transmission lines for the new HVDC projects (see Fig. 1.2a) [7, 8]. This decision was influenced by public resistance to overhead lines and by the perceived benefits of underground systems in terms of aesthetics and reduced land use conflicts [9]. However, the design and implementation of underground HVDC cable systems remain an area of active research [10, 11, 12]. One of the most critical aspects of these systems is the reliability of the cable joints.

Cable joints are considered the most vulnerable components in HVDC transmission lines [11, 9, 3, 6]. HVDC cable joints may fail due to the following reasons: on-site installation errors, charge accumulation, polarization effects, and high internal electric field stresses

Figure 1.1: Planned high voltage direct current transmission lines in Germany (Figure taken from [13]).

[12, 14, 3]. The failure of HVDC cable joints is especially critical due to the large number of joints required along a transmission route. This necessity arises from the immense weight of the cable drums, which limits underground cables to segments of 1-1.5 kilometers in length (see Fig. 1.2b) [15, 16]. Given the high number of joints, ensuring their individual reliability is paramount to the overall reliability of the transmission system. A single joint failure can result in extended downtime, significantly impacting the electrical energy supply [8].

This thesis focuses on the development of simulation tools to aid in the design of HVDC cable joints, aiming to mitigate the issues leading to joint failures and enhance their overall reliability. Through this research, the thesis contributes to the broader goal of ensuring a stable and efficient green energy transition in Germany.
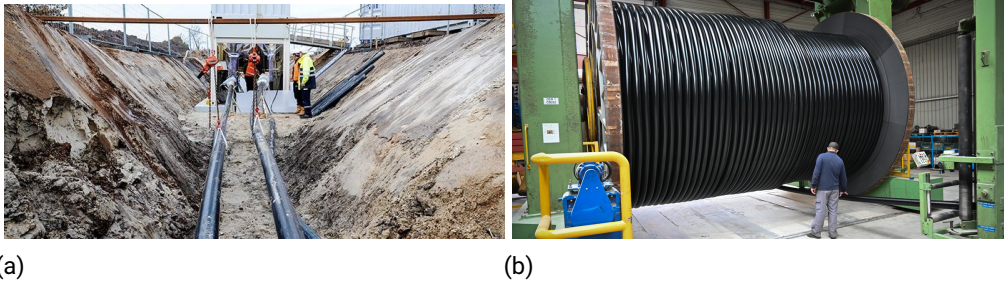
Figure 1.2: (a) Construction site of an underground cable system (Figure taken from [17]). (b) Cable drum of a HVDC cable (Figure taken from [18]).

1.2 Overview

This dissertation presents a comprehensive study on the electrothermal modeling and simulation of HVDC cable joints, with a particular focus on both steady-state and transient operations. The work is organized into the following chapters:

Chapter 2 provides background information on HVDC cable joint technology. This chapter sets the foundation for understanding the technical aspects and challenges in HVDC cable joint design.

Chapter 3 introduces the 320 kV lead example used throughout the thesis, a model provided by [12]. This example serves as a consistent reference point for the discussions and simulations presented in subsequent chapters.

Chapter 4 details the electrothermal modeling and simulation approach for HVDC cable joints during steady-state operation. It describes the implementation of a nonlinear coupled electrothermal solver within *Pyrit* [19], a freely available Finite Element (FE) framework developed at the Institute of Accelerator Science and Electromagnetic Fields at the TU Darmstadt. The solver is validated against a reference solution obtained via the commercial software COMSOL Multiphysics®, and the electrothermal behavior of the lead example during steady-state operation is discussed briefly.

Chapter 5 expands the modeling approach to transient operations, such as switching impulse events. The chapter describes the implementation of a transient nonlinear coupled

electrothermal solver in *Pyrit* and discusses the benefits of a multi-rate time integration scheme. The solver is validated using COMSOL Multiphysics®, and the transient electrothermal behavior of the 320 kV lead example during switching impulse operation is analyzed.

Chapter 6 explores different approaches for efficient sensitivity computation, focusing on the derivation of the direct sensitivity method (DSM) and the adjoint variable method (AVM) for coupled transient electrothermal problems. The derivation of the AVM, which is a core contribution of this thesis and published in [20, 21, 22], is discussed in detail. The chapter also covers the discretization and multi-rate implementation of the AVM. The AVM is applied to compute the sensitivities of the 320 kV lead example during switching impulse operation and the sensitivites are validated against results obtained by the direct sensitivity method implemented in *Pyrit* as well as finite difference computations in COMSOL Multiphysics®.

Chapter 7 demonstrates the application of simulation for estimating material parameters from measurement data. An inverse problem approach is used to estimate the thermal conductivities of the joint's insulating materials based on mock-up temperature measurements.

Chapter 8 reviews various approaches for modeling and simulating slow polarization processes and evaluates their suitability for application to HVDC cable joint simulation.

Chapter 9 concludes the dissertation with a summary of the findings and suggests directions for future research.

2 Background on HVDC Cable Joints

In the realm of HVDC power transmission via underground cables, cable joints play a critical role in connecting short cable segments to span long distances. This chapter introduces the general setup of a cable joint, and discusses different materials and field grading concepts.

2.1 Structure of a Cable Joint

The purpose of a cable joint is to securely connect two cable segments while ensuring mechanical strength to prevent damage or separation and offering protection against environmental factors such as moisture. The basic structure of a cable joint consists of several key components and is depicted in Fig. 2.1. The cables themselves consist of copper conductors (domain 3), an insulation layer (domain 2) and a grounded outer sheath (domain 1). At the joint, the copper conductors are exposed by partially removing the cable insulation and sheath. The exposed conductors are then connected by a conductor clamp (domain 4) which is covered by a semi-conductive shielding electrode (domain 5) in order to ensure a smooth electric field distribution. The core of the joint is made up of insulating material (domain 6), and the joint is completed by a semi-conductive outer sheath (domain 7), which is connected to ground potential.

2.2 HVDC Insulation Materials

Insulation systems of HVDC cable joints face distinct challenges compared to alternating current (AC) systems. The unidirectional direct current (DC) voltage can cause the accu-
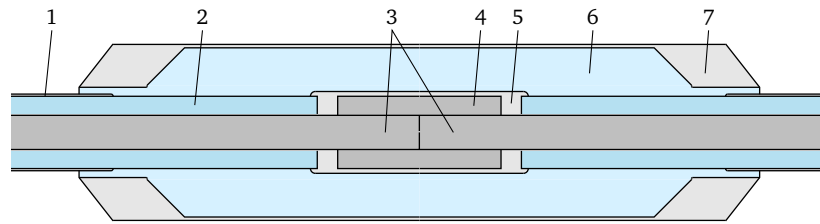
Figure 2.1: Basic structure of a cable joint: (1) grounded semi-conductive outer cable sheath (2) cable insulation (3) conductors (4) conductor clamp (5) semi-conductive deflector (6) joint insulation (7) grounded semi-conductive outer joint sheath (adapted from [12, 23]). The conducting, semi-conducting and insulating materials are highlighted in dark gray, light gray, and blue, respectively.

mulation of space charges, leading to local electric field enhancements and an increased risk of breakdown [24, 25]. In addition, the constant high electric field stresses in HVDC systems degrade insulation materials more rapidly than the alternating stresses in high voltage alternating current (HVAC) systems [26]. Finally, the electric field distribution in HVDC joints is highly dependent on the electric conductivity of the materials, which often varies strongly with temperature, leading to unpredictable field variations and increased failure rates [3, 27].

Research on the failure mechanisms of HVDC cable joints is an ongoing effort. A key focus area is the development of advanced insulation materials with better thermal and electrical properties, enhanced resistance to polarization, and lower charge accumulation tendencies. Insulation in high voltage (HV) cable joints typically utilizes either silicone rubber (SiR) or ethylene propylene diene monomer (EPDM) [11, 28, 29]. SiR is preferred for HVAC cable joints due to its manufacturing benefits [11], higher breakdown strength and wider temperature range of stability of electrical and mechanical properties [28]. In contrast, EPDM is predominantly used for HVDC cable joints because its electrical properties can be tailored to minimize charge accumulation and because EPDM is less complex to compound [29, 28].

Recent advancements in nanotechnology allow for tailored insulation materials with nonlinear fillers [30, 31, 32, 33, 34, 35]. These advancements, coupled with challenges

in manufacturing, installation, operation, and aging, introduce significant variabilities and uncertainties. Therefore, design optimization based solely on prototyping and experimentation is impractical. It is essential to develop and apply dedicated measurement and advanced simulation approaches for HVDC cable joints. In the long run, these methods will provide new insights into the nonlinear electrothermal behavior, incorporate the latest developments in material science and manufacturing technologies and translate these insights into design rules and strategies.

2.3 Electric Field Grading

(a) Cable end without field grading.

(b) Cable joint with geometric field grading.

(c) Cable joint with nonlinear resistive field grading.

(d) Cable termination with refractive field grading.
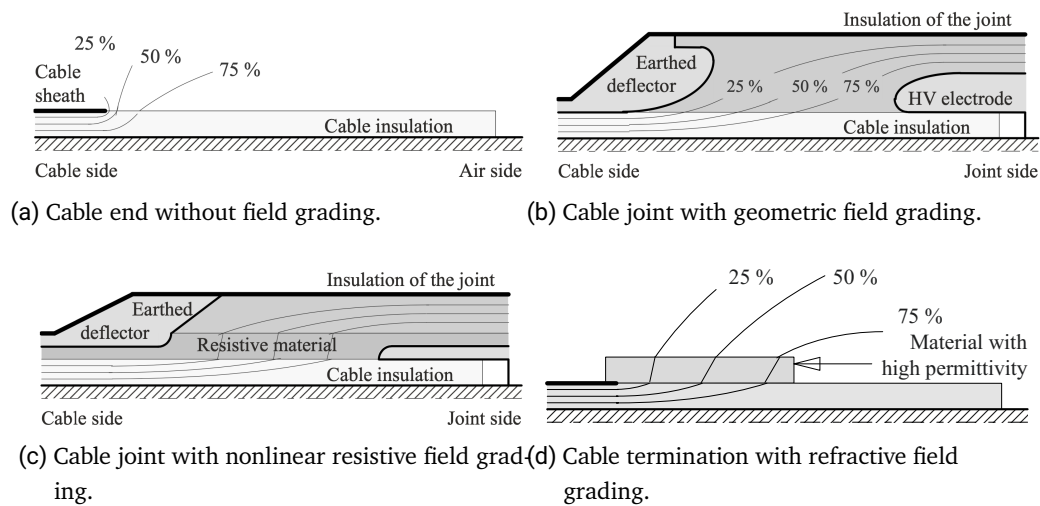
Figure 2.2: Schematic representation of equipotential lines near the end of the grounded cable sheath for different types of field grading [5].

Modern cable joint designs rely heavily on the principle of field grading, i.e. balancing the electric field stress at material interfaces and within the insulation materials in order to prevent a dielectric breakdown [3, 5]. In HVDC systems, the two main field grading approaches are geometric field grading and nonlinear resistive field grading [3, 5, 29]. It is crucial to select a field grading strategy that is appropriate for both steady-state DC

operation as well as transient overvoltages [3, 5].

Figure 2.2a shows the equipotential lines at the end of a cable segment. It can be seen that near the grounded cable sheath, a strong voltage drop and, as a result, strong electric field stresses occur. Geometric field grading reduces this voltage drop by extending the grounded outer cable sheath with a curved deflector, as shown in Figure 2.2b. This deflector, embedded in the joint insulation and connected to ground potential, mitigates the field stress along the material interface. However, challenges include the increased size of the device and the inability to optimize field grading for different operating conditions due to the fixed shape of the electrodes [3, 5].

An alternative approach is nonlinear field grading, which uses a layer of field grading material (FGM). The conductivity of the FGM layer increases significantly beyond a switching field strength, as illustrated in Fig. 2.3 [12, 3, 36]. Placed between the cable and joint insulations, the FGM layer balances the electric field distribution by becoming more conductive in high-stress areas, thus redistributing the voltage drop to less stressed regions (see Fig. 2.2c) [3, 5, 36]. The dynamic adaptability of the FGM layer to different field distributions provides a distinct advantage over geometric field grading, and it requires minimal volume [3, 5]. Potential issues include the temperature-dependent conductivity of FGMs, which can cause Joule heating, posing potential threats to the joint's thermal stability and long-term performance [3, 5, 36].

Refractive field grading is often used in HVAC cable joints. In the HVDC context, it often appears as a side effect to nonlinear resistive field grading, since most FGMs feature higher permittivities than insulation materials [3]. Field refraction reduces the normal component of the electric field inside the FGM, resulting in a lower field strength at the end of the cable sheath (see Figure 2.2d). Refractive field grading is only effective during transient processes, when the fields are dominated by displacement currents.

Field grading remains a complex and evolving area of research due to its many dependencies and challenges [11, 23, 10, 12, 36]. For example, even small variations in the dimensions and placement of geometric field grading components can substantially influence the overall breakdown behavior of cable accessories [37]. Consequently, designing effective field grading is a primary challenge in the development of HVDC cable joints.

Accurate modeling and simulation of electric field and temperature distributions are

indispensable for developing effective field grading strategies. This understanding helps to reduce reliance on empirical knowledge and simplifies the design process by providing deeper insights into the electrothermal behavior of HVDC cable joints.
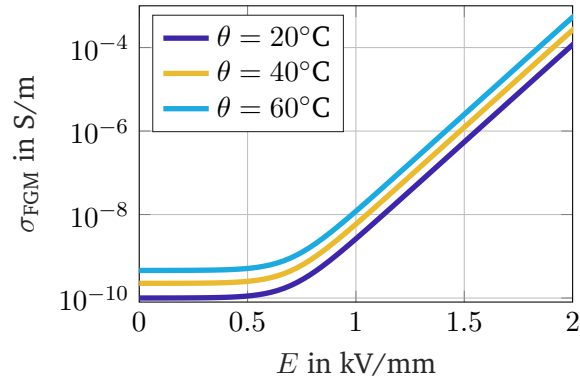
Figure 2.3: Nonlinear field-dependent conductivity of the FGM. The FGM conductivity is described by the analytic function (3.1).

3 Lead Example

In this thesis, the realistic 320 kV HVDC cable joint specimen with a nonlinear FGM grading concept presented in [12, 15] serves as the lead example. Figure 3.1 depicts a cut of the cable joint in a cylindrical coordinate system (ϱ, φ, z), where the dash-dotted line indicates rotational symmetry along the z-axis. To allow for a two-dimensional (2D) axisymmetric simulation approach, three-dimensional (3D) details such as screws or conductor bundeling have been neglected. The joint connects two cables, each comprising a copper conductor (domain 4), a semi-conductive inner shield (domain 3), an insulation layer (domain 2), and a grounded outer sheath (domain 1). The conductors are connected by an aluminum connector (domain 5), which is encased by a semi-conductive shielding electrode (domain 6). The cable's primary insulation is made of cross-linked polyethylene (XLPE), while the main insulation of the joint body (domain 7) is made from insulating SiR. The semi-conductive layers (domain 1, 3, 6, and 9) are made of semi-conductive SiR. Both the outer sheath of the cable joint (domain 9) and the outer semiconductor of the cable (domain 1) are connected to ground potential. A layer of nonlinear FGM (domain 8) is placed between the insultation layers of the cable and the joint. The joint is placed 2 m below the ground and surrounded by a 30 cm thick base layer of sand.

The conductivity of the FGM is highly variable and depends on the electric field strength, E in kV/mm, and the temperature, θ in K. It is given by the analytic function [36, 38]

$$\sigma_{\mathrm{FGM}}(E, \theta) = p_1 \frac{1 + p_4^{(E-p_2)p_2^{-1}}}{1 + p_4^{(E-p_3)p_2^{-1}}} \exp(-p_5(\theta^{-1} - \theta_{\mathrm{amb}}^{-1})), \qquad (3.1)$$

with the parameters $p_1 = 10^{-10}$ S/m, $p_2 = 0.7$ kV/mm, $p_3 = 2.4$ kV/mm, $p_4 = 1864$ and $p_5 = 3713.59$ K and $\theta_{\mathrm{amb}} = 293.15$ K. The field dependence at a fixed temperature is shown
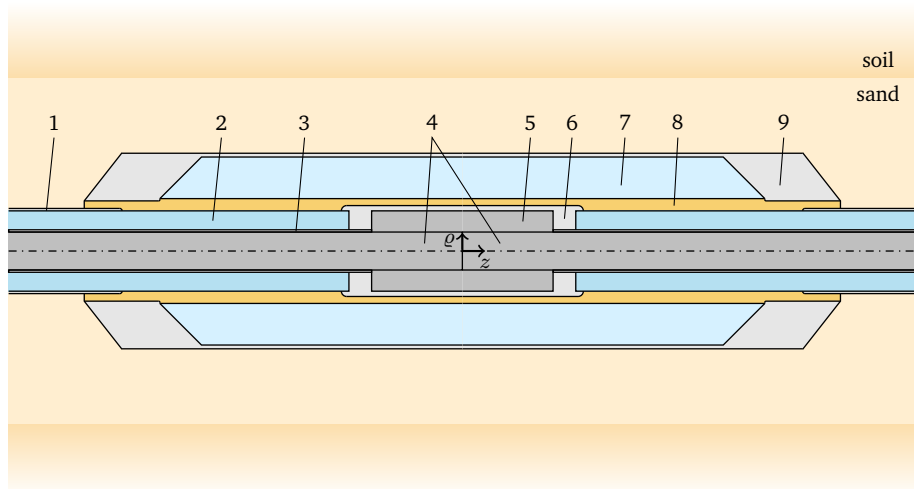
Figure 3.1: Schematic of the investigated HVDC joint in the ϱ-z-plane (adapted from [12, 15]). The colors indicate conductive materials (dark gray), semi-conductive layers (light gray), insulating materials (blue) and the FGM material layer (yellow).

in Fig. 2.3 [39]. The remaining material characteristics are summarized in Table 3.1 and Table 3.2.

Table 3.1: Electric HVDC Cable Joint Material Parameters [12].

domain	electric conductivity σ in S/m	relative permittivity ε_r
outer cable sheath (1)	1.0	10
cable insulation (2)	$1.0 \cdot 10^{-15}$	2.3
inner cable shield (3)	1.0	10
cable conductors (4)	$6.0 \cdot 10^7$	1
connector (5)	$3.8 \cdot 10^7$	1
shielding electrode (6)	1.0	10
joint insulation (7)	$5.0 \cdot 10^{-13}$	10
FGM (8)	see (3.1)	10
outer joint sheath (9)	1.0	10
sand	–	–
soil	–	–

Table 3.2: Thermal HVDC Cable Joint Material Parameters [12].

domain	thermal conductivity λ in W/(m·K)	density ρ in kg/m^3	specific heat capacity c_p in J/(kg·K)
outer cable sheath (1)	0.25	1160	1250
cable insulation (2)	0.3	963	2500
inner cable shield (3)	0.25	1050	1250
cable conductors (4)	400	8960	385
connector (5)	238	2700	900
shielding electrode (6)	0.25	1050	1250
joint insulation (7)	0.22	1100	1230
FGM (8)	0.5	1100	1500
outer joint sheath (9)	0.25	1160	1250
sand	0.54	2200	835
soil	0.8	1275	1830

4 HVDC Cable Joint in Steady State Operation

HVDC cable joints, when subjected to a constant DC voltage, ultimately attain a resistive-thermal steady state [23]. This chapter delves into the modeling and simulation of this steady state, providing a detailed analysis of the simulation results for the 320 kV specimen introduced in Ch. 3.

4.1 Electrothermal Modeling

The resistive-thermal steady state is characterized by the combination of the stationary current problem and the stationary heat conduction problem. The stationary current problem reads

$$\operatorname{div}(\boldsymbol{J}) = 0 \qquad , \ \boldsymbol{r} \in \Omega\,; \tag{4.1a}$$

$$\boldsymbol{J} = \sigma \boldsymbol{E} \qquad , \ \boldsymbol{r} \in \Omega\,; \tag{4.1b}$$

$$\boldsymbol{E} = -\operatorname{grad}(\phi), \ \boldsymbol{r} \in \Omega\,; \tag{4.1c}$$

$$\phi = \phi_{\text{fixed}} \qquad , \ \boldsymbol{r} \in \Gamma_{\text{D,el}}\,; \tag{4.1d}$$

$$\boldsymbol{J} \cdot \boldsymbol{n}_{\text{el}} = J_{n,\text{fixed}} \qquad , \ \boldsymbol{r} \in \Gamma_{\text{N,el}}\,, \tag{4.1e}$$

where $\boldsymbol{J}$ is the resistive current density, $\boldsymbol{E}$ is the electric field and ϕ is the electric scalar potential. Here, σ is the specific electric conductivity, $\boldsymbol{r}$ is the position vector, and Ω represents the computational domain. The fixed voltages at the Dirichlet boundaries, $\Gamma_{\text{D, el}} \neq \emptyset$, are denoted as ϕ_{fixed}. At the Neumann boundaries, $\Gamma_{\text{N, el}} = \partial\Omega\backslash\Gamma_{\text{D, el}}$, a normal current density, $J_{n,\text{fixed}}$, is defined. The normal unit vector at the Neumann boundaries

Figure 4.1: Illustration of the electric boundary conditions used for the steady-state simulation of the 320 kV cable joint specimen. The Dirichlet boundaries, $\Gamma_{\text{D, el}}$, define the ground potential (blue) at the outer cable sheath and outer joint sheath, as well as the high voltage potential (red) at the copper conductors. The nominal current of $I = 2\,\text{kA}$ through the conductors is prescribed using a Neumann boundary condition (green) with $J_{n,\text{fixed}} = \frac{I}{A_{\text{Cu}}}$, where A_{Cu} is the cross-sectional area of the copper conductors. Homogeneous Neumann conditions, $J_{n,\text{fixed}} = 0$, are applied to all remaining boundaries.

is denoted as $\boldsymbol{n}_{\text{el}}$. For a clearer understanding, Fig. 4.1 illustrates the electric boundary conditions applied during the steady-state simulation of the 320 kV cable joint specimen.

Eliminating $\boldsymbol{J}$ and $\boldsymbol{E}$ yields the potential equation,

$$-\operatorname{div}\left(\sigma \operatorname{grad}\left(\phi\right)\right) = 0 \qquad , \ \boldsymbol{r} \in \Omega \, ; \tag{4.2a}$$

$$\phi = \phi_{\text{fixed}}, \ \boldsymbol{r} \in \Gamma_{\text{D,el}} \, ; \tag{4.2b}$$

$$-\sigma \operatorname{grad}\left(\phi\right) \cdot \boldsymbol{n}_{\text{el}} = 0 \qquad , \ \boldsymbol{r} \in \Gamma_{\text{N,el}} \, . \tag{4.2c}$$

The stationary heat conduction problem reads

$$\operatorname{div}\left(\dot{\boldsymbol{q}}\right) = p_{\text{Joule}} \qquad , \ \boldsymbol{r} \in \Omega \, ; \tag{4.3a}$$

$$\dot{\boldsymbol{q}} = -\lambda \operatorname{grad}\left(\theta\right), \ \boldsymbol{r} \in \Omega \, ; \tag{4.3b}$$

$$\theta = \theta_{\text{fixed}} \qquad , \ \boldsymbol{r} \in \Gamma_{\text{D, th}} \, , \tag{4.3c}$$

$$\dot{\boldsymbol{q}} \cdot \boldsymbol{n}_{\text{th}} = 0 \qquad , \ \boldsymbol{r} \in \Gamma_{\text{N, th}} \, , \tag{4.3d}$$

where θ is the temperature, $\dot{\boldsymbol{q}}$ is the heat flux density, p_{Joule} is the Joule loss density, and λ is the thermal conductivity. θ_{fixed} are the fixed temperatures at the Dirichlet boundaries, $\Gamma_{\text{D, th}} \neq \emptyset$, and $\boldsymbol{n}_{\text{th}}$ is the unit vector at the Neumann boundaries, $\Gamma_{\text{N, th}} = \partial\Omega \backslash \Gamma_{\text{D, th}}$. The two equations (4.1) and (4.3) are coupled along the Joule loss density, $p_{\text{Joule}} = \boldsymbol{J} \cdot \boldsymbol{E}$, and
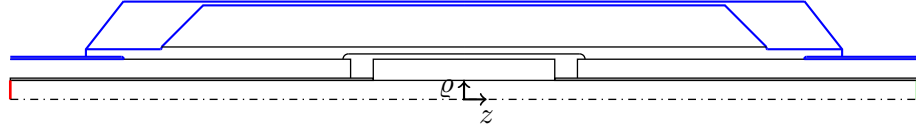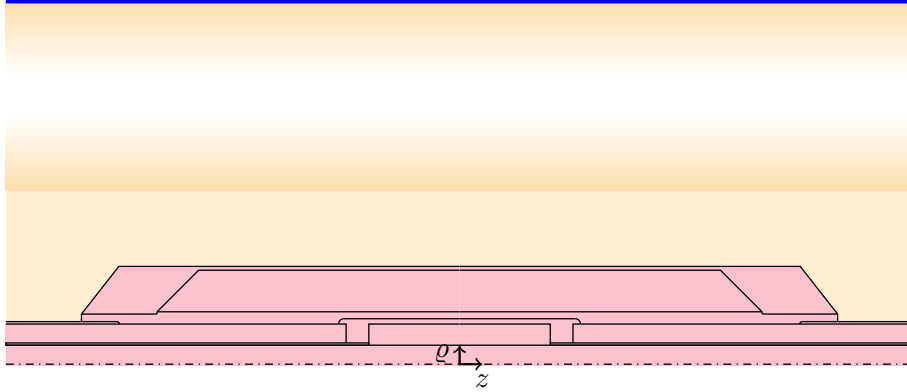
Figure 4.2: Illustration of the thermal excitations and boundary conditions used for the steady-state simulation of the 320 kV cable joint specimen. The primary heat source are the Joule losses within the cable joint (red). Additionally, an ambient temperature of $\theta_{\text{fixed}} = 20°\text{C}$ is assumed at the top of the soil (blue).

the field- and temperature-dependent electric conductivity, i.e. $\sigma = \sigma(\boldsymbol{E}, \theta)$. Eliminating $\dot{\boldsymbol{q}}$ from (4.3) yields

$$- \operatorname{div}\left(\lambda \operatorname{grad}\left(\theta\right)\right) = p_{\text{Joule}}, \ \boldsymbol{r} \in \Omega \, ; \tag{4.4a}$$

$$\theta = \theta_{\text{fixed}}\, , \ \boldsymbol{r} \in \Gamma_{\text{D,th}} \, ; \tag{4.4b}$$

$$-\lambda \operatorname{grad}\left(\theta\right) \cdot \boldsymbol{n}_{\text{th}} = 0 \quad , \ \boldsymbol{r} \in \Gamma_{\text{N,th}} \, . \tag{4.4c}$$

The thermal model of the 320 kV cable joint specimen is illustrated in Fig. 4.2.

4.2 Numerical Approach

4.2.1 Finite Element Discretization

The differential equations describing the electrothermal behavior of a cable joint are formulated as a 2D axisymmetric FE problem. The Finite Element Method (FEM) discretizes the spatial computational domain into simple geometric elements—here, triangular elements that are rotated around the symmetry axis—and approximates the solution using

piecewise polynomial functions. Substituting this approximate solution into the governing partial differential equations transforms the problem into a system of algebraic equations or, for time-dependent problems, a system of ordinary differential equations. For more information about the FEM, see [40, 41].

In this work, the electric scalar potential and the temperature are discretized using linear nodal shape functions, $N_j(\varrho, z)$, i.e.,

$$\phi \approx \sum_j u_j N_j \, ; \tag{4.5}$$

$$\theta \approx \sum_j v_j N_j \, , \tag{4.6}$$

where u_j and v_j are the degrees of freedom (DoF), which are assembled in the vectors $\mathbf{u}$ and $\mathbf{v}$, respectively. The discretized versions of (4.2) and (4.4) according to the Ritz procedure read

$$\mathbf{K}_\sigma \mathbf{u} = 0 \, ; \tag{4.7}$$

$$\mathbf{K}_\lambda \mathbf{v} = \boldsymbol{s}_{p_{\mathrm{Joule}}} \, , \tag{4.8}$$

with

$$[\boldsymbol{K}_{(\cdot)}]_{ij} = \int_\Omega (\cdot) \, \mathrm{grad}\,(N_i) \cdot \, \mathrm{grad}\,(N_j) \, \mathrm{d}\Omega \quad i, j = 1, ..., N_{\mathrm{node}} \, ; \tag{4.9}$$

$$[\boldsymbol{s}_{(\cdot)}]_i = \int_\Omega (\cdot) N_i \, \mathrm{d}\Omega \qquad\qquad i = 1, ..., N_{\mathrm{node}} \, , \tag{4.10}$$

where N_{node} denotes the number of nodes.

4.2.2 Electrothermal Coupling

To accurately capture the resistive-thermal steady state of HVDC cable joints, it is essential to couple the electric and thermal subproblems. This is achieved through a successive substitution scheme, which iteratively updates the solutions of the electric and thermal fields until convergence is reached. The successive substitution scheme is shown in Fig. 4.3 and comprises the following steps: The process begins with an initial guess for the temperature distribution within the cable joint. This initial guess could be a

uniform temperature or an estimated distribution based on prior knowledge. Using this temperature distribution, the temperature-dependent electric conductivities, $\sigma = \sigma(\boldsymbol{E}, \theta)$, are updated. The electric subproblem (4.7) is then solved using the Newton method. Once the electric field and current density are determined, the Joule loss density, which acts as the primary heat source, is calculated using $p_{\text{Joule}} = \boldsymbol{J} \cdot \boldsymbol{E}$. This calculated Joule loss density is then used as an input for the thermal subproblem (4.8), which is then solved. The updated temperature distribution is then fed back into the electric subproblem, and the process is repeated iteratively. This successive substitution continues until a specified convergence criterion is reached or the maximum number of iterations is exceeded.

Starting with a uniform initial temperature guess of $20°$C, and setting the convergence criteria for both the successive substitution method and the Newton method to a relative change in Joule heat, i.e. $\int_{\Omega} p_{\text{Joule}} \, d\Omega$, below $10^{-6}\%$ and $10^{-7}\%$ respectively, the steady-state simulation of the cable joint typically requires 7 successive substitution iterations and a total of 31 Newton iterations.

4.2.3 Implementation and Solver Validation

The electrothermal solver and cable joint model are implemented in *Pyrit* [19], a freely available FE framework developed in Python at the Institute of Accelerator Science and Electromagnetic Fields at the TU Darmstadt. *Pyrit* features a template-based structure that allows for a simple and user-friendly simulation workflow. At the same time, it grants access to all FE matrices and basic routines, supporting the implementation of innovative modeling and simulation ideas often found in a research setting, such as the AVM presented in Ch. 6.

The simulations of the cable joint are performed using a mesh consisting of 21663 nodes and 42842 finite elements. The simulation results obtained with *Pyrit* are validated against results obtained using the commercial simulation software COMSOL Multiphysics®. Figure 4.4 presents a comparison between the results from both solvers. Figure 4.4a shows the tangential electric field at the interface between the cable insulation and the layer of FGM (dark blue line in Fig. 4.5). Figure 4.4b illustrates the radial temperature distribution inside the cable joint at $z = 0.405\,\text{m}$ (yellow line in Fig. 4.5). The results from both *Pyrit* and COMSOL Multiphysics® are in very good agreement, confirming the
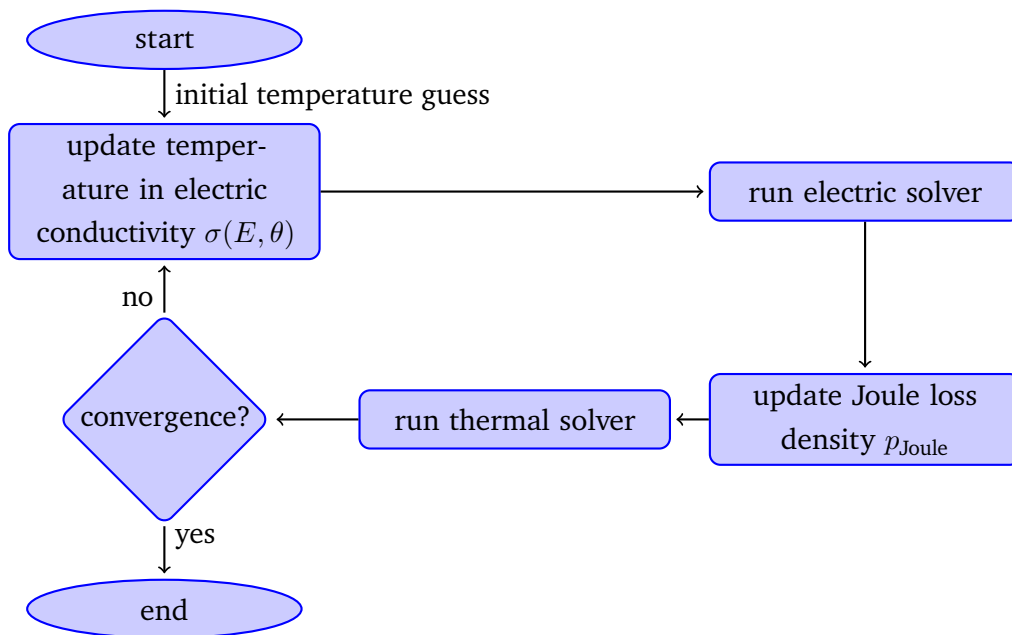
Figure 4.3: Structural diagram of the successive substitution coupling scheme.

accuracy and reliability of the *Pyrit*-based solver. The electrothermal solver has thereby been successfully validated, demonstrating its capability to accurately model the complex interactions within the cable joint under continuous DC operation.

4.3 Electrothermal Analysis

In this section, the electrothermal simulation results of the 320 kV cable joint specimen are discussed. Figure 4.6a shows the electric field distribution inside the cable joint. High field strengths, in the range of several kV/mm, are observed in the cable and the joint insulation. Since the FGM's electric conductivity is significantly higher than those of the cable's and joint's insulation, respectively, the electric field stresses within the FGM layer are low, effectively decoupling the stresses in the cable insulation from those in the joint
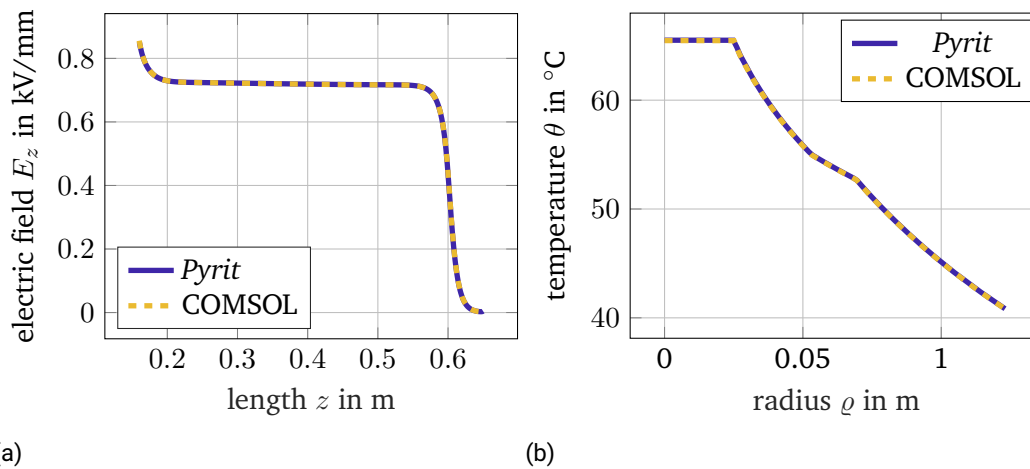
Figure 4.4: Comparison of the simulation results obtained by *Pyrit* and COMSOL Multiphysics®. The left side shows the tangential electric field at the interface between the cable insulation and the FGM. The right side shows the radial temperature distribution at $z = 0.405$ m. The results of both solvers are in very good agreement.

body.

Figure 4.6b shows the temperature distribution inside the cable joint. The temperature ranges from 65.5°C at the copper conductors to 40.6°C inside the joint insulation.

The combined effect of the electric field strength and the temperature leads to an increase in the nonlinear electric conductivity inside the FGM from 10^{-10} S/m up to $5 \cdot 10^{-9}$ S/m. The Joule losses inside the joint's insulation and FGM layer are 2.7 W. For comparison, the losses per meter inside the copper conductors are 34 W/m.

According to [5], tangential electric field stresses at material interfaces are particularly critical. Therefore, Fig. 4.7 shows the tangential electric field stress at (a) the interface between the FGM and the cable insulation (dark blue evaluation path in Fig. 4.5) and (b) at the interface between the FGM and the joint insulation (light blue evaluation path in Fig. 4.5). Generally, the highest tangential field stress is expected to be located near the triple points (red circles in Fig. 4.5). According to Fig. 4.7, during steady-state operation,
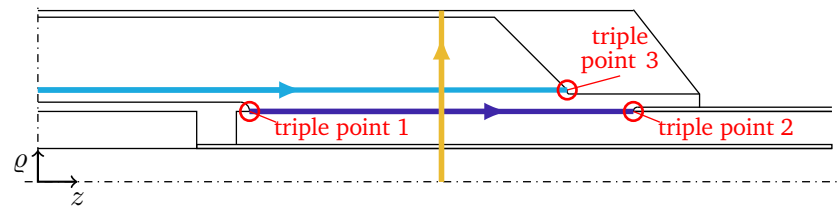
Figure 4.5: Evaluation paths and positions inside the cable joint.

the highest tangential electric field stress of $0.85\,$kV/mm is located at the triple point next to the conductor clamp (triple point 1), closely followed by a stress of $0.81\,$kV/mm at triple point 3 next to the housing of the cable joint. Additionally, to demonstrate the benefits of employing a nonlinear FGM, Fig. 4.7 also shows the tangential electric field stress obtained when the electric conductivity of the FGM is fixed at a constant value of $10^{-10}\,$S/m. It can be seen that the nonlinear behavior of the FGM reduces the maximum tangential field stress at the triple point next to the conductor clamp by nearly 60%, from $2.0\,$kV/mm to $0.85\,$kV/mm.
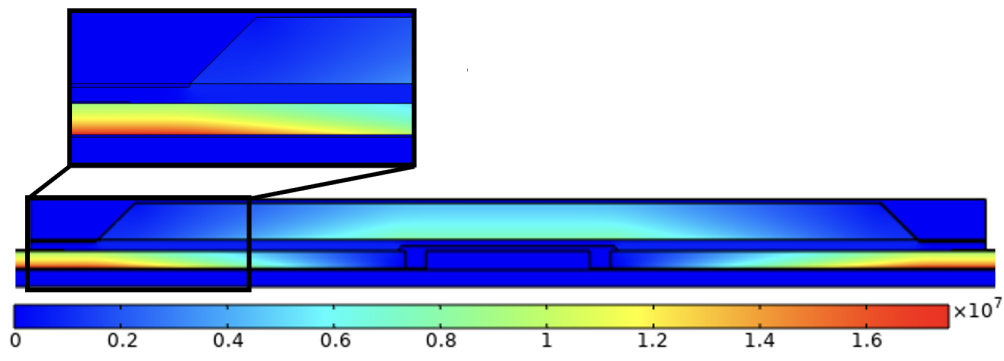
(a) Electric field strength E in V/m.
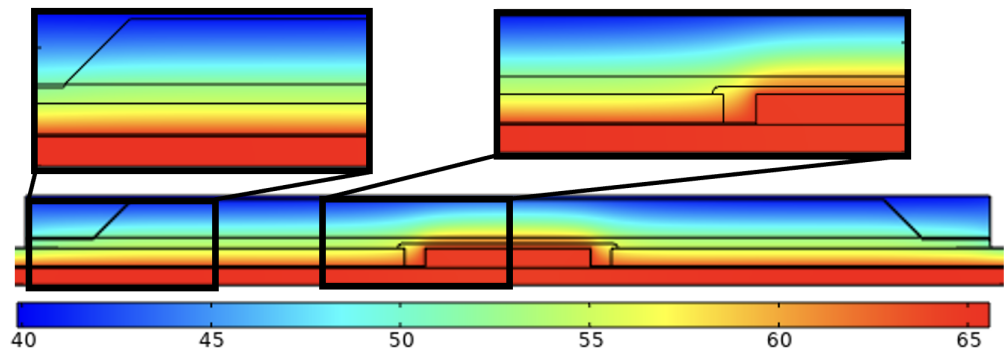
(b) Temperature θ in $^\circ$C.

Figure 4.6: (a) Electric field and (b) temperature distribution inside the 320 kV cable joint specimen during steady-state operation.
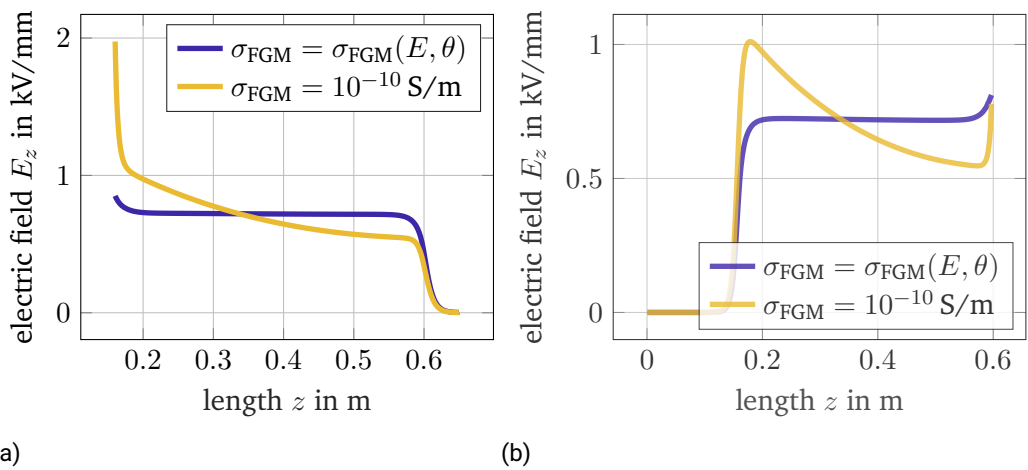
Figure 4.7: Tangential electric field strength at (a) the interface between the FGM and the cable insulation (dark evaluation path in Fig. 4.5) and (b) at the interface between the FGM and the joint insulation (light blue evaluation path in Fig. 4.5). The blue curves represent results for an FGM with a field- and temperature-dependent electric conductivity, while the yellow curves represent results with the FGM's electric conductivity fixed at 10^{-10} S/m.

5 HVDC Cable Joint in Switching Impulse Operation

In this chapter, the electrothermal behavior of HVDC cable joints during impulse operation is explored. This analysis is crucial for understanding the joint's performance and robustness under transient conditions, such as switching operations, which can significantly impact the electric field distribution and thermal stresses within the joint.

5.1 Electrothermal Modeling

The electrothermal behavior of a cable joint that is subjected to transient overvoltages, e.g. a lightning strike or switching operations, can be described by the combination of the transient electroquasistatic (EQS) equation and the transient heat conduction equation [42]. The transient EQS problem is defined as follows:

$$\mathrm{div}\,(\boldsymbol{J}) + \mathrm{div}\,(\partial_t \boldsymbol{D}) = 0 \qquad , \; t \in [t_\mathrm{s}, t_\mathrm{f}], \; \boldsymbol{r} \in \Omega\,; \tag{5.1a}$$

$$\boldsymbol{J} = \sigma \boldsymbol{E} \qquad , \; t \in [t_\mathrm{s}, t_\mathrm{f}], \; \boldsymbol{r} \in \Omega\,; \tag{5.1b}$$

$$\boldsymbol{D} = \varepsilon \boldsymbol{E} \qquad , \; t \in [t_\mathrm{s}, t_\mathrm{f}], \; \boldsymbol{r} \in \Omega\,; \tag{5.1c}$$

$$\boldsymbol{E} = -\,\mathrm{grad}\,(\phi), \; t \in [t_\mathrm{s}, t_\mathrm{f}], \; \boldsymbol{r} \in \Omega\,; \tag{5.1d}$$

$$\phi = \phi_\mathrm{fixed} \qquad , \; t \in [t_\mathrm{s}, t_\mathrm{f}], \; \boldsymbol{r} \in \Gamma_\mathrm{D,el}\,; \tag{5.1e}$$

$$(\boldsymbol{J} + \partial_t \boldsymbol{D}) \cdot \boldsymbol{n}_\mathrm{el} = 0 \qquad , \; t \in [t_\mathrm{s}, t_\mathrm{f}], \; \boldsymbol{r} \in \Gamma_\mathrm{N,el}\,; \tag{5.1f}$$

$$\phi = \phi_0 \qquad , \; t = t_\mathrm{s} \quad , \; \boldsymbol{r} \in \Omega\,, \tag{5.1g}$$

where $\boldsymbol{D}$ is the electric displacement field, and ε represents electric permittivity. The initial and final simulation time are denoted as t_s and t_f, respectively. ϕ_0 denotes the initial

condition of the electric potential, representing the steady state before the transient event (see Ch. 4). Eliminating $\boldsymbol{J}$, $\boldsymbol{D}$ and $\boldsymbol{E}$ yields the EQS potential equation,

$$-\operatorname{div}\left(\sigma \operatorname{grad}\left(\phi\right)\right) - \operatorname{div}\left(\partial_t\left(\varepsilon \operatorname{grad}\left(\phi\right)\right)\right) = 0 \quad , \ t \in [t_s, t_f], \ \boldsymbol{r} \in \Omega\,; \tag{5.2a}$$

$$\phi = \phi_{\text{fixed}}, \ t \in [t_s, t_f], \ \boldsymbol{r} \in \Gamma_{\text{D,el}}\,; \tag{5.2b}$$

$$\left(-\sigma \operatorname{grad}\left(\phi\right) - \partial_t\left(\varepsilon \operatorname{grad}\left(\phi\right)\right)\right) \cdot \boldsymbol{n}_{\text{el}} = 0 \quad , \ t \in [t_s, t_f], \ \boldsymbol{r} \in \Gamma_{\text{N,el}}\,; \tag{5.2c}$$

$$\phi = \phi_0 \quad , \ t = t_s \quad , \ \boldsymbol{r} \in \Omega\,. \tag{5.2d}$$

The transient heat conduction equation reads

$$\partial_t\left(c_V\theta\right) + \operatorname{div}\left(\dot{\boldsymbol{q}}\right) = p_{\text{Joule}} \quad , \ t \in [t_s, t_f], \ \boldsymbol{r} \in \Omega\,; \tag{5.3a}$$

$$\dot{\boldsymbol{q}} = -\lambda \operatorname{grad}\left(\theta\right), \ t \in [t_s, t_f], \ \boldsymbol{r} \in \Omega\,; \tag{5.3b}$$

$$\theta = \theta_{\text{fixed}} \quad , \ t \in [t_s, t_f], \ \boldsymbol{r} \in \Gamma_{\text{D,th}}\,; \tag{5.3c}$$

$$\dot{\boldsymbol{q}} \cdot \boldsymbol{n}_{\text{th}} = 0 \quad , \ t \in [t_s, t_f], \ \boldsymbol{r} \in \Gamma_{\text{N,th}}\,; \tag{5.3d}$$

$$\theta = \theta_0 \quad , \ t = t_s \quad , \ \boldsymbol{r} \in \Omega\,, \tag{5.3e}$$

where $c_V = \rho c_p$ is the volumetric heat capacity, and θ_0 denotes the initial condition of the temperature, i.e. the steady-state temperature distribution before the transient event. The two equations are coupled along the Joule loss density $p_{\text{Joule}} = \boldsymbol{J} \cdot \boldsymbol{E}$ and the field- and temperature-dependent electric conductivity and permittivity, respectively, i.e. $\sigma = \sigma(\boldsymbol{E}, \theta)$ and $\varepsilon = \varepsilon(\boldsymbol{E}, \theta)$. Eliminating $\dot{\boldsymbol{q}}$ gives

$$\partial_t\left(c_V\theta\right) - \operatorname{div}\left(\lambda \operatorname{grad}\left(\theta\right)\right) = p_{\text{Joule}}, \ t \in [t_s, t_f], \ \boldsymbol{r} \in \Omega\,; \tag{5.4a}$$

$$\theta = \theta_{\text{fixed}}, \ t \in [t_s, t_f], \ \boldsymbol{r} \in \Gamma_{\text{D,th}}\,; \tag{5.4b}$$

$$-\lambda \operatorname{grad}\left(\theta\right) \cdot \boldsymbol{n}_{\text{th}} = 0 \quad , \ t \in [t_s, t_f], \ \boldsymbol{r} \in \Gamma_{\text{N,th}}\,; \tag{5.4c}$$

$$\theta = \theta_0 \quad , \ t = t_s \quad , \ \boldsymbol{r} \in \Omega\,. \tag{5.4d}$$

5.2 Numerical Approach

5.2.1 Discretization

The differential equations describing the electrothermal behavior of a cable joint are formulated as a 2D axisymmetric FE problem. The electric scalar potential and the

temperature are discretized using linear nodal shape functions according to (4.5) and (4.6), respectively. The semi-discrete versions of (5.2) and (5.4) according to the Ritz method read

$$\mathbf{K}_\sigma \mathbf{u} + \partial_t \left(\mathbf{K}_\varepsilon \mathbf{u} \right) = 0 \, ; \tag{5.5}$$

$$\mathbf{K}_\lambda \mathbf{v} + \partial_t \left(\mathbf{M}_{c_V} \mathbf{v} \right) = \boldsymbol{s}_{p_{\mathrm{Joule}}} , \tag{5.6}$$

with

$$[\boldsymbol{M}_{(\cdot)}]_{ij} = \int_\Omega (\cdot) N_i N_j \, \mathrm{d}\Omega \;\; i, j = 1, ..., N_{\mathrm{node}} \, . \tag{5.7}$$

The equations (5.5) and (5.6) are further discretized in time using an implicit Euler time stepping scheme, i.e.

$$\Delta t_{\mathrm{el},n+1} \mathbf{K}_\sigma^{n+1} \mathbf{u} + \mathbf{K}_\varepsilon^{n+1} \mathbf{u}^{n+1} = \mathbf{K}_\varepsilon^n \mathbf{u}^n \, ; \tag{5.8}$$

$$\Delta t_{\mathrm{th},n+1} \mathbf{K}_\lambda^{n+1} \mathbf{v}^{n+1} + \mathbf{M}_{c_V}^{n+1} \mathbf{v}^{n+1} = \Delta t_{\mathrm{th},n+1} \boldsymbol{s}_{p_{\mathrm{Joule}}}^{n+1} + \mathbf{M}_{c_V}^n \mathbf{v}^n , \tag{5.9}$$

where the superscripts indicate the time step at which the quantities are evaluated and $\Delta t_{\mathrm{el},n+1}$ and $\Delta t_{\mathrm{th},n+1}$ denote the electric and thermal time step size, respectively.

5.2.2 Multi-Rate Time-Integration

When simulating the transient electrothermal problem, an effective strategy to reduce computational cost involves employing a multi-rate time-integration scheme [43]. A multi-rate approach involves treating the electric and thermal domains as separate subsystems, each with its own time integration step, Δt_{el} and Δt_{th} [43, 44]. With thermal dynamics spanning minutes to hours [37, 27] and electric phenomena occurring on the microsecond to millisecond scale, different time steps are necessary. Smaller steps are used for the electric domain to capture rapid electrical changes, while larger steps suffice for the slower thermal processes. This strategy efficiently simulates the transient electrothermal problem while accurately representing both rapid electrical dynamics and slower thermal responses. The coupling between the two domains is achieved through a weak coupling scheme, as illustrated in Fig. 5.1 [43]. This scheme assumes a proportional relationship between the thermal time step and the smaller electric time step, i.e., $\Delta t_{\mathrm{th}} = N \Delta t_{\mathrm{el}}$, with N being an

arbitrary positive integer. Initially, the electric solver advances N times using the smaller electric time step, Δt_{el}. Subsequently, the Joule loss density is computed, followed by a single thermal time step calculation. After each thermal time step, updates are made to the electric material characteristics, and the electric solver is restarted at the next time interval. This iterative process continues until reaching the final simulation time t_{f}. To handle the nonlinearities inherent in the electric subproblem, a damped Newton method is employed.
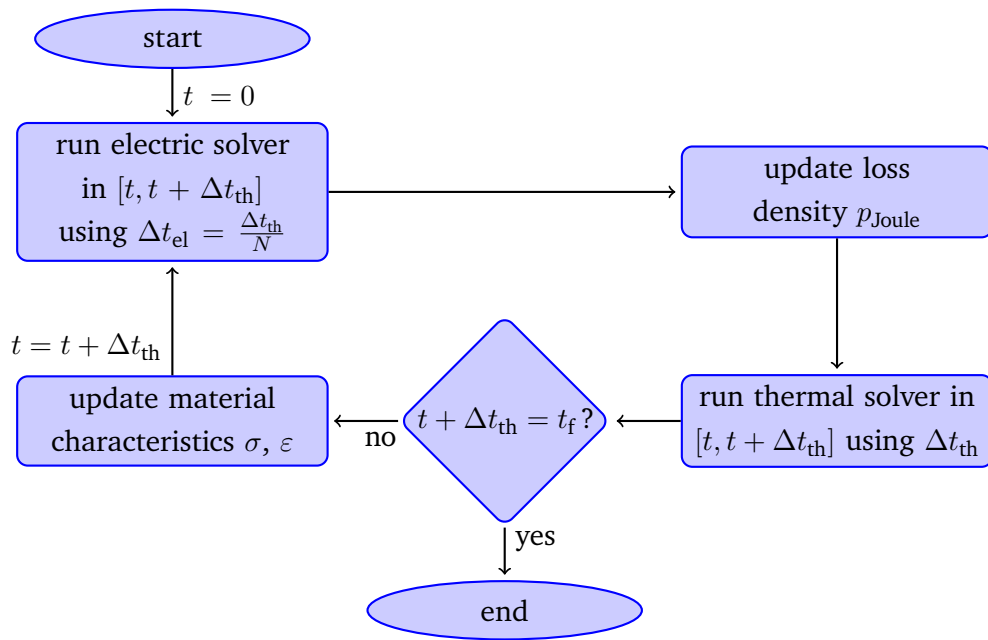
Figure 5.1: Structural diagram of a electrothermal simulation procedure with a weak coupling scheme.

5.2.3 Implementation and Solver Validation

The transient electrothermal solver is implemented for 2D axisymmetric problems in *Pyrit* and validated using the model depicted in Fig. 5.2. The model consists of a layer of FGM
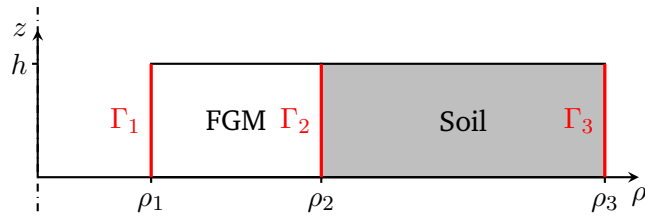
Figure 5.2: Geometry of the validation model in the ρ-z-plane. The symmetry axis is indicated by the dashdotted line.

with an inner radius $\rho_1 = 0.1\,\text{m}$ and an outer radius $\rho_2 = 0.3\,\text{m}$. In z-direction, a height of $h = 0.1\,\text{m}$ is assumed. The FGM is placed between two electrodes, Γ_1 and Γ_2, and surrounded by a layer of soil with $\rho_3 = 1\,\text{m}$. The outer electrode, Γ_2, is set to ground potential and a sinusoidal voltage $U = 150\,\text{kV} + 80\,\text{kV}\sin\left(\frac{2\pi}{300\,\text{s}}t\right)$ is applied to the inner electrode, Γ_1. Furthermore, the inner electrode and the outer boundary of the soil layer, Γ_3, are set to a fixed temperature of $60°\text{C}$ and $20°\text{C}$, respectively. The initial potential and temperature distribution are set to the resistive steady state that corresponds to a DC excitation of $150\,\text{kV}$ (see Fig. 5.3).

(a)

(b)
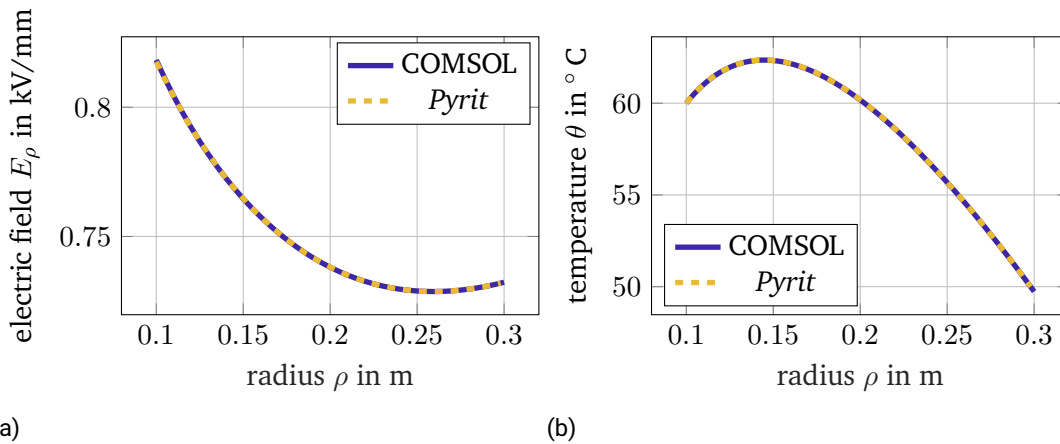
Figure 5.3: Steady-state electric field distribution (a) and temperature distribution (b) along the ρ-axis.

The first step in validating the multi-rate time integration approach involves computing the mean and maximum relative deviation, denoted as e_{rel}, of the electric field along the ρ-axis for different time step sizes, $\Delta t = \Delta t_{el} = \Delta t_{th}$. The relative deviation is computed with respect to a reference solution obtained for a very small time step size of $\Delta t = 0.1\,s$. As shown in Fig. 5.4a, with a time step size of $\Delta t = 0.25\,s$ a relative deviation below 0.01% is achieved. Next, the relative deviation is computed for different thermal time steps while fixing the electric time step at $\Delta t_{el} = 0.25\,s$. Figure 5.4b shows that the solver maintains a maximum relative deviation of approximately 0.01% even when the thermal time step is set twelve times larger than the electric time step, i.e. $\Delta t_{th} = 12\Delta t_{el} = 3\,s$.

Finally, the simulation results obtained with *Pyrit* are compared to results obtained via COMSOL Multiphysics®. Figures 5.5a and 5.5b compare the results for the electric field strength and the temperature at $\rho = 0.15\,m$ over time. The results of both solvers are in very good agreement with a mean and maximum relative deviation of the electric field strength of 0.05 % and 0.1 %, respectively. Thus, the transient electrothermal solver has been successfully validated.

(a)

(b)
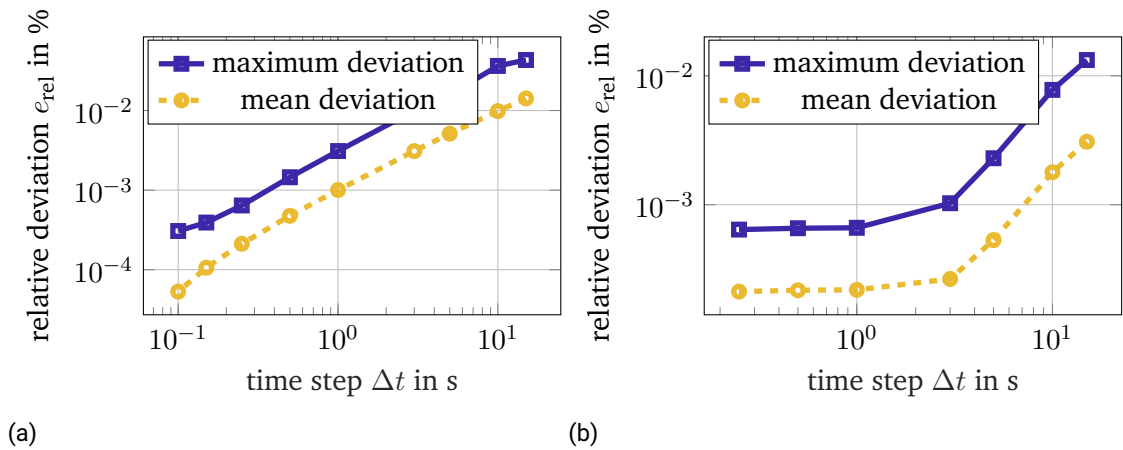
Figure 5.4: (a) Relative deviation of the electric field along the ρ-axis for different time step sizes, $\Delta t = \Delta t_{el} = \Delta t_{th}$. (b) Relative deviation of the electric field along the ρ-axis for different thermal time step sizes, Δt_{th} and a fixed electric time step size $\Delta t_{el} = 0.25\,s$
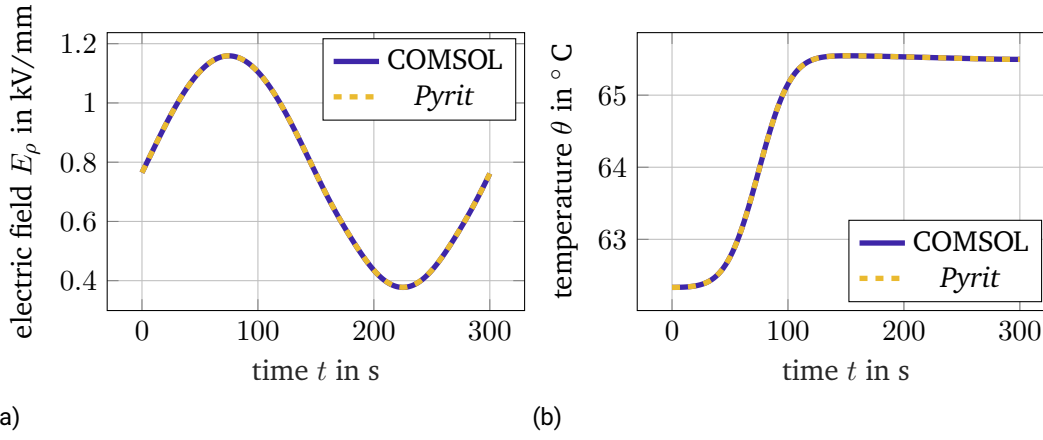
Figure 5.5: Comparison between the results obtained via COMSOL Multiphysics®and *Pyrit*. (a) shows the electric field strength E and (b) the temperature at $\rho = 0.15$ m over time.

5.3 Electrothermal Analysis

In this section, the electrothermal simulation results of the 320 kV cable joint specimen subjected to a switching impulse are discussed. The switching impulse is depicted in Fig. 5.6 and defined according to [5, 10] as

$$U_{\text{switch}}(t) = U_{\text{DC}} + \hat{U}\,\frac{\tau_2}{\tau_2 - \tau_1}\left(\exp\left(-\frac{t}{\tau_2}\right) - \exp\left(-\frac{t}{\tau_1}\right)\right), \qquad (5.10)$$

with $U_{\text{DC}} = 320$ kV, $\hat{U} = 1.15\,U_{\text{DC}} = 368$ kV and the constants $\tau_1 = \frac{250}{2.41}$ µs and $\tau_2 = \frac{2500}{0.87}$ µs. It rises to peak potential of 688 kV within $t_{\text{rise}} = 0.357$ ms and then declines, taking $t_{\text{fall,50\%}} = 2.45$ ms to fall by 50%.

Figure 5.7 shows the tangential electric field at the material interfaces of the FGM and the insulating materials at various time instances during the impulse. Here, time instance $t_{\text{rise,50\%}} = 0.0614$ ms represents the time required for the impulse to reach half its peak value. The simulation results reveal that the electric field distribution during the impulse varies significantly from the steady-state distribution. Notably, the maximum field stress is approximately doubled.

(a)   (b)
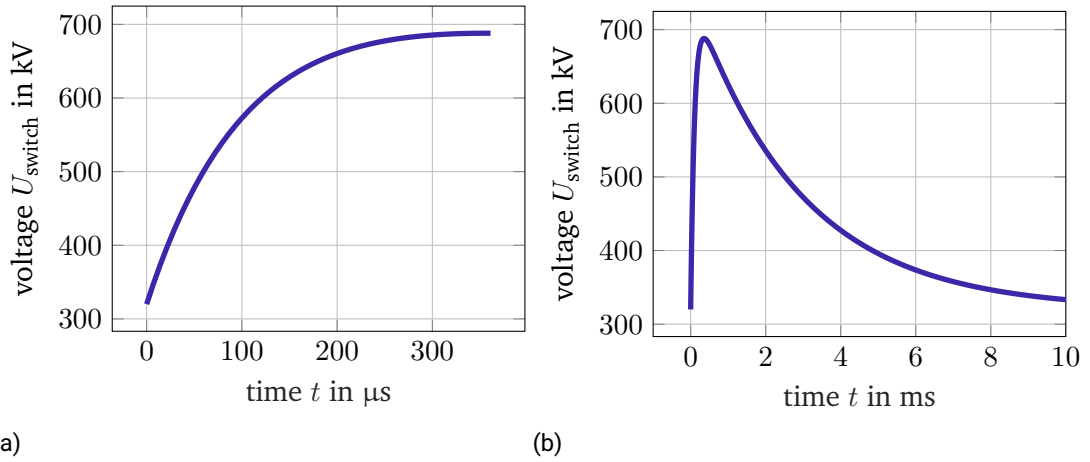
Figure 5.6: Switching impulse overvoltage over time defined according to [5, 10].

Figure 5.8 shows the absolute value of the tangential field electric field at the material interfaces near all three triple points over time. The maximum tangential field stress of 1.75 kV/mm occurs after 0.0916 ms and is located at triple point 1 next to the conductor clamp (see Fig. 4.5). Figure 5.8b shows that after approximately 2.5 s, the electric field returns to its steady-state distribution.

During the switching impulse, the nonlinear conductivity of the FGM increases significantly, reaching a maximum value of $6 \cdot 10^{-7}$S/m compared to the maximum value of $5 \cdot 10^{-9}$S/m observed during steady-state operation. Figure 5.9a shows a substantial increase in Joule losses, which spike from 2.7 W during steady-state operation to a peak of 46 kW after 0.351 ms, i.e. shortly before the impulse peak. Despite this dramatic rise in Joule losses, no significant heating is observed due to the short duration of the impulse, as shown in Fig. 5.9b.
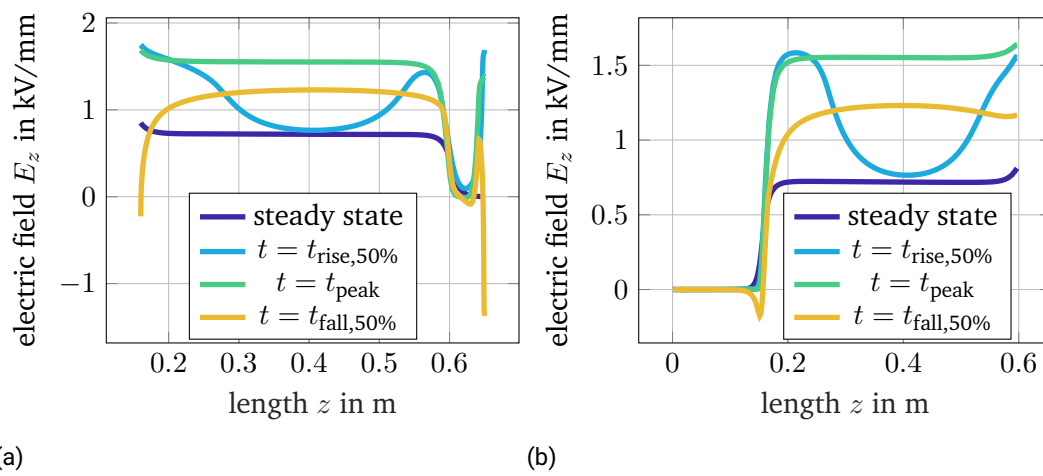
Figure 5.7: Tangential electric field strength at (a) the interface between the FGM and the cable's insulation (dark blue evaluation path in Fig. 4.5) and (b) at the interface between the FGM and the joint's insulation (light blue evaluation path in Fig. 4.5) for different time instances.

(a)

(b)
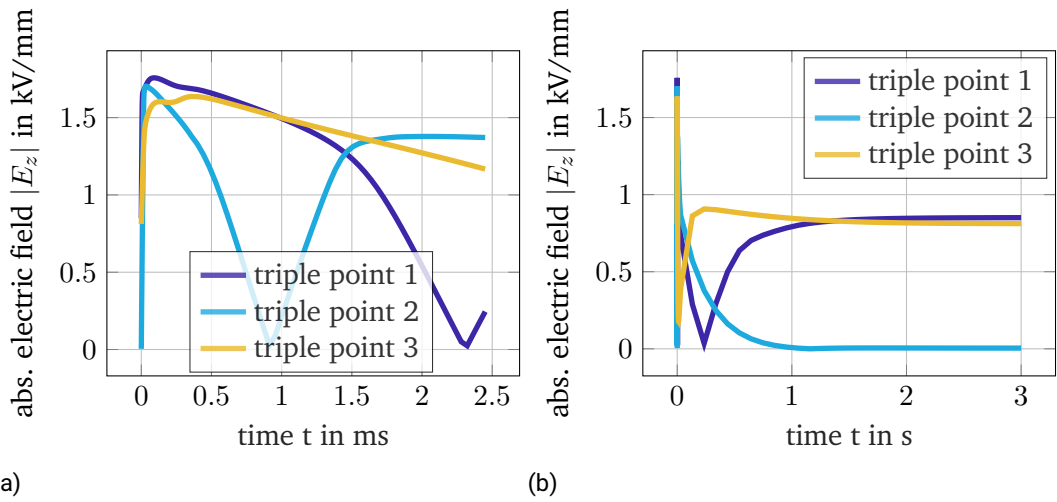
Figure 5.8: Absolute value of the tangential electric field stress at the material interfaces near the three triple points (see Fig. 4.5) over time. For clarity, the figure presents the results across different time scales, with (a) highlighting the interval from 0 ms to $t_{\text{fall,50\%}}$=2.45 ms.

(a)

(b)
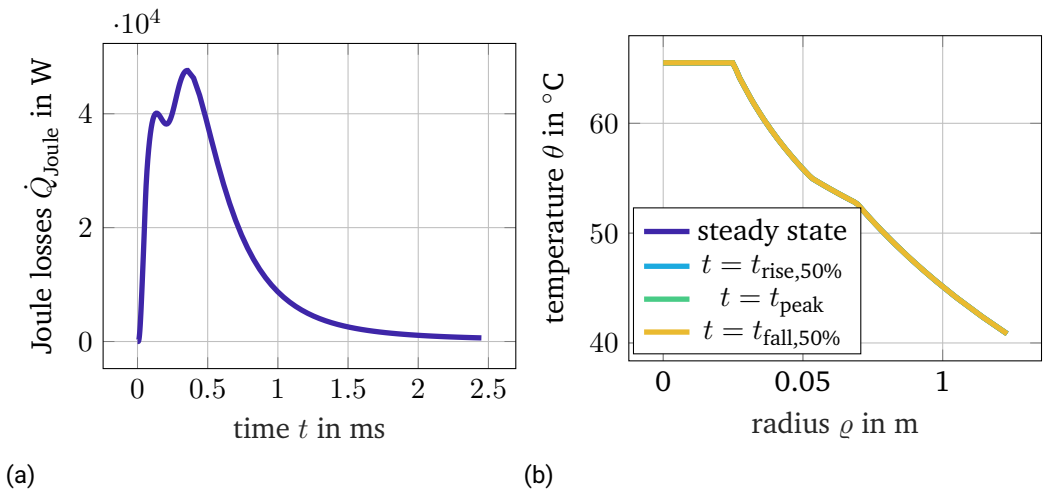
Figure 5.9: (a) The Joule losses $\dot{Q}_{\text{Joule}}$ over time. (b) The radial temperature distribution at $z = 0.405$ m for different time instances.

6 Sensitivity Computation

Advances in material science have enabled the precise tailoring of an FGM's nonlinear conductivity characteristic to fit specific application requirements [45, 36]. When designing an FGM, its material properties are represented by a set of design parameters $\boldsymbol{p} = [p_1, ..., p_{N_{\mathrm{p}}}]$. The performance of the FGM is assessed based on several quantities of interest (QoIs), G_k, where $k = 1, ..., N_{\mathrm{QoI}}$, such as the Joule losses or the electric field stress at critical positions.

Traditionally, practical approaches and rules of thumb have been developed to select the nonlinear conductivity characteristics of FGMs [36]. However, relying on these methods can be limiting, as they often depend on prior knowledge that may not be available for future cable joint designs. Moreover, the nonlinear behavior of FGMs and the need to balance multiple – possibly conflicting – QoIs make manual optimization, e.g. using parameter sweeps, extremely challenging. For example, sweeping the five parameters defining the conductivity characteristic (3.1) with only three values each would already result in $3^5 = 243$ simulations, which is impractical.

A more systematic approach can be achieved by leveraging sensitivity information to guide the design process. Sensitivities quantify how small changes in a design parameter p_j influence a given QoI G_k, expressed as $\frac{\mathrm{d}G_k}{\mathrm{d}p_j}(\boldsymbol{p}_0)$, where $\boldsymbol{p}_0 = [p_{1,0}, ..., p_{N_{\mathrm{p}},0}]$ denotes the current parameter configuration. This information allows the quantification of the influence of individual parameters and enables the comparison of their effects on different QoIs. Sensitivities are the foundation of gradient-based optimization approaches, which can effectively reduce the number of expensive nonlinear coupled transient FE simulations [46].

In this chapter, two complementary methods for the sensitivity computation of HVDC cable joints with respect to material parameters are presented: the DSM and the AVM.

The derivation of the AVM for nonlinear transient coupled electrothermal problems is one of the core contributions of this thesis and has been published in [20, 21, 22].

6.1 Direct Sensitivity Method

One of the most commonly used methods for sensitivity computation is the DSM [47]. The DSM appeals with its simple derivation and straight-forward implementation. The method computes the sensitivities of the electric potential and the temperature, respectively, i.e. $\frac{\mathrm{d}\phi}{\mathrm{d}p_j}(\boldsymbol{p}_0)$ and $\frac{\mathrm{d}\theta}{\mathrm{d}p_j}(\boldsymbol{p}_0)$, from which the sensitivities can then be computed directly according to

$$\frac{\mathrm{d}G_k}{\mathrm{d}p_j}(\boldsymbol{p}_0) = \frac{\partial G_k}{\partial p_j}(\boldsymbol{p}_0) + \frac{\partial G_k}{\partial \phi}\frac{\mathrm{d}\phi}{\mathrm{d}p_j}(\boldsymbol{p}_0) + \frac{\partial G_k}{\partial \theta}\frac{\mathrm{d}\theta}{\mathrm{d}p_j}(\boldsymbol{p}_0), \tag{6.1}$$

where the sensitivity has been written in more detail using the chain rule. The sensitivities $\frac{\mathrm{d}\phi}{\mathrm{d}p_j}(\boldsymbol{p}_0)$ and $\frac{\mathrm{d}\theta}{\mathrm{d}p_j}(\boldsymbol{p}_0)$ are computed by solving the sensitivity formulation. The sensitivity formulation is a system of linear coupled transient partial differential equations (PDEs) obtained by taking the derivative of (5.1) and (5.3) to p_j. Thus, the DSM requires the solution of one additional PDE system for each parameter. Consequently, this approach is efficient if the number of QoIs, N_{QoI}, is larger than the number of parameters, N_{p}. The derivative of (5.1) to p_j reads

$$\mathrm{div}\left(\boldsymbol{J}'\right) + \mathrm{div}\left(\frac{\partial \boldsymbol{D}'}{\partial t}\right) = 0 \qquad\qquad , \, t \in [t_{\mathrm{s}}, t_{\mathrm{f}}], \, \boldsymbol{r} \in \Omega\,; \tag{6.2a}$$

$$\boldsymbol{J}' = \frac{\partial \sigma}{\partial p_j}\boldsymbol{E} + \overline{\overline{\sigma}}_{\mathrm{d}}\boldsymbol{E}' + \frac{\partial \sigma}{\partial \theta}\theta'\boldsymbol{E} \quad , \, t \in [t_{\mathrm{s}}, t_{\mathrm{f}}], \, \boldsymbol{r} \in \Omega\,; \tag{6.2b}$$

$$\boldsymbol{D}' = \frac{\partial \varepsilon}{\partial p_j}\boldsymbol{E} + \overline{\overline{\varepsilon}}_{\mathrm{d}}\boldsymbol{E}' + \frac{\partial \varepsilon}{\partial \theta}\theta'\boldsymbol{E} \quad , \, t \in [t_{\mathrm{s}}, t_{\mathrm{f}}], \, \boldsymbol{r} \in \Omega\,; \tag{6.2c}$$

$$\boldsymbol{E}' = -\mathrm{grad}\left(\phi'\right) \qquad\qquad , \, t \in [t_{\mathrm{s}}, t_{\mathrm{f}}], \, \boldsymbol{r} \in \Omega\,; \tag{6.2d}$$

$$\phi' = 0 \qquad\qquad , \, t \in [t_{\mathrm{s}}, t_{\mathrm{f}}], \, \boldsymbol{r} \in \Gamma_{\mathrm{D,el}}\,; \tag{6.2e}$$

$$\left(\boldsymbol{J}' + \frac{\partial \boldsymbol{D}'}{\partial t}\right) \cdot \boldsymbol{n} = 0 \qquad\qquad , \, t \in [t_{\mathrm{s}}, t_{\mathrm{f}}], \, \boldsymbol{r} \in \Gamma_{\mathrm{N,el}}\,; \tag{6.2f}$$

$$\phi = \phi_0 \qquad\qquad , \, t = t_{\mathrm{s}} \quad , \, \boldsymbol{r} \in \Omega\,. \tag{6.2g}$$

where all quantities are evaluated at $\boldsymbol{p}_0$ and $(\cdot)' = \frac{\mathrm{d}(\cdot)}{\mathrm{d}p_j}$ is used as a shorthand for the full derivatives of of a quantity to p_j, e.g., $\phi' = \frac{\mathrm{d}\phi}{\mathrm{d}p_j}$. The differential electric conductivity and

differential permittivity are denoted by $\overline{\overline{\sigma}}_{\mathrm{d}}$ and $\overline{\overline{\varepsilon}}_{\mathrm{d}}$, respectively. They are defined as [21, 48]:

$$\overline{\overline{\sigma}}_{\mathrm{d}}(\boldsymbol{E}, \theta) = \sigma(\boldsymbol{E}, \theta) \begin{bmatrix} 1 & 0 \\ 0 & 1 \end{bmatrix} + 2 \frac{\mathrm{d}\sigma}{\mathrm{d}E^2}(\boldsymbol{E}, \theta) \boldsymbol{E} \boldsymbol{E}^T \,,$$

$$\overline{\overline{\varepsilon}}_{\mathrm{d}}(\boldsymbol{E}, \theta) = \varepsilon(\boldsymbol{E}, \theta) \begin{bmatrix} 1 & 0 \\ 0 & 1 \end{bmatrix} + 2 \frac{\mathrm{d}\varepsilon}{\mathrm{d}E^2}(\boldsymbol{E}, \theta) \boldsymbol{E} \boldsymbol{E}^T \,,$$

and are evaluated for the operating points defined by the nominal solution. Since the electrode potentials do not depend on material parameters, the Dirichlet boundary condition becomes homogeneous. Eliminating $\boldsymbol{J}'$, $\boldsymbol{D}'$ and $\boldsymbol{E}'$ brings up

$$-\mathrm{div}\big(\overline{\overline{\sigma}}_{\mathrm{d}} \,\mathrm{grad}\,(\phi')\big) - \mathrm{div}\left(\frac{\partial}{\partial t}\big(\overline{\overline{\varepsilon}}_{\mathrm{d}} \,\mathrm{grad}\,(\phi')\big)\right)$$

$$= -\mathrm{div}\left(\frac{\partial \sigma}{\partial p_j} \boldsymbol{E} + \frac{\partial \sigma}{\partial \theta} \theta' \boldsymbol{E}\right)$$

$$\qquad - \mathrm{div}\left(\frac{\partial}{\partial t}\left(\frac{\partial \varepsilon}{\partial p_j} \boldsymbol{E} + \frac{\partial \varepsilon}{\partial \theta} \theta' \boldsymbol{E}\right)\right) \qquad\qquad , \ t \in [t_{\mathrm{s}}, t_{\mathrm{f}}], \ \boldsymbol{r} \in \Omega\,; \qquad (6.3\mathrm{a})$$

$$\phi' = 0 \qquad\qquad\qquad\qquad\qquad\qquad\qquad , \ t \in [t_{\mathrm{s}}, t_{\mathrm{f}}], \ \boldsymbol{r} \in \Gamma_{\mathrm{D,el}}\,; \quad (6.3\mathrm{b})$$

$$\left(-\overline{\overline{\sigma}}_{\mathrm{d}} \,\mathrm{grad}\,(\phi') - \frac{\partial}{\partial t}\big(\overline{\overline{\varepsilon}}_{\mathrm{d}} \,\mathrm{grad}\,(\phi')\big)\right) \cdot \boldsymbol{n}$$

$$= -\left(\frac{\partial \sigma}{\partial p_j} \boldsymbol{E} + \frac{\partial \sigma}{\partial \theta} \theta' \boldsymbol{E} + \frac{\partial}{\partial t}\left(\frac{\partial \varepsilon}{\partial p_j} \boldsymbol{E} + \frac{\partial \varepsilon}{\partial \theta} \theta' \boldsymbol{E}\right)\right) \cdot \boldsymbol{n}, \ t \in [t_{\mathrm{s}}, t_{\mathrm{f}}], \ \boldsymbol{r} \in \Gamma_{\mathrm{N,el}}\,; \quad (6.3\mathrm{c})$$

$$\phi' = \phi'_0 \qquad\qquad\qquad\qquad\qquad\qquad\qquad , \ t = t_{\mathrm{s}} \qquad , \ \boldsymbol{r} \in \Omega\,. \qquad (6.3\mathrm{d})$$

The derivative of (5.3) to p_j reads

$$\frac{\partial}{\partial t}\left(\left(\frac{\partial c_{\mathrm{V}}}{\partial p_j} + \frac{\partial c_{\mathrm{V}}}{\partial \theta} \theta'\right)\theta + c_{\mathrm{V}}\theta'\right) + \mathrm{div}\,(\dot{\boldsymbol{q}}')$$

$$= p'_{\mathrm{Joule}} = \left(\frac{\partial \sigma}{\partial p_j} + \frac{\partial \sigma}{\partial \theta} \theta'\right)E^2 + \boldsymbol{J} \cdot \boldsymbol{E}' + \overline{\overline{\sigma}}_{\mathrm{d}} \boldsymbol{E} \cdot \boldsymbol{E}', \ t \in [t_{\mathrm{s}}, t_{\mathrm{f}}], \ \boldsymbol{r} \in \Omega\,; \qquad (6.4\mathrm{a})$$

$$\dot{\boldsymbol{q}}' = -\frac{\partial \lambda}{\partial p_j} \,\mathrm{grad}\,(\theta) - \frac{\partial \lambda}{\partial \theta} \theta' \,\mathrm{grad}\,(\theta) - \lambda \,\mathrm{grad}\,(\theta') \qquad , \ t \in [t_{\mathrm{s}}, t_{\mathrm{f}}], \ \boldsymbol{r} \in \Omega\,; \qquad (6.4\mathrm{b})$$

$$\theta = 0 \qquad\qquad , t \in [t_{\mathrm{s}}, t_{\mathrm{f}}],\ \boldsymbol{r} \in \Gamma_{\mathrm{D,th}} ; \quad (6.4\mathrm{c})$$

$$\dot{\boldsymbol{q}}' \cdot \boldsymbol{n} = 0 \qquad\qquad , t \in [t_{\mathrm{s}}, t_{\mathrm{f}}],\ \boldsymbol{r} \in \Gamma_{\mathrm{N,th}} ; \quad (6.4\mathrm{d})$$

$$\theta' = \theta'_0 \qquad\qquad , t \in t = t_{\mathrm{s}},\ \boldsymbol{r} \in \Omega . \qquad (6.4\mathrm{e})$$

where, again, all quantities are evaluated at p_0. Eliminating $\dot{\boldsymbol{q}}'$ yields

$$-\boldsymbol{J} \cdot \boldsymbol{E}' - \overline{\overline{\sigma}}_{\mathrm{d}} \boldsymbol{E} \cdot \boldsymbol{E}'$$

$$+ \frac{\partial}{\partial t} \left(\left(\frac{\partial c_{\mathrm{V}}}{\partial p_j} + \frac{\partial c_{\mathrm{V}}}{\partial \theta} \theta' \right) \theta + c_{\mathrm{V}} \theta' \right)$$

$$- \operatorname{div} \left(\frac{\partial \lambda}{\partial \theta} \theta' \operatorname{grad}(\theta) \right) - \operatorname{div} \left(\lambda \operatorname{grad}(\theta') \right) - \frac{\partial \sigma}{\partial \theta} \theta' E^2$$

$$= \operatorname{div} \left(\frac{\partial \lambda}{\partial p_j} \operatorname{grad}(\theta) \right) + \frac{\partial \sigma}{\partial p_j} E^2 \qquad , t \in [t_{\mathrm{s}}, t_{\mathrm{f}}],\ \boldsymbol{r} \in \Omega ; \qquad (6.5\mathrm{a})$$

$$\theta = 0 \qquad\qquad , t \in [t_{\mathrm{s}}, t_{\mathrm{f}}],\ \boldsymbol{r} \in \Gamma_{\mathrm{D,th}} ; \quad (6.5\mathrm{b})$$

$$\dot{\boldsymbol{q}}' \cdot \boldsymbol{n} = 0 \qquad\qquad , t \in [t_{\mathrm{s}}, t_{\mathrm{f}}],\ \boldsymbol{r} \in \Gamma_{\mathrm{N,th}} ; \quad (6.5\mathrm{c})$$

$$\theta' = \theta'_0 \qquad\qquad , t \in t = t_{\mathrm{s}},\ \boldsymbol{r} \in \Omega . \qquad (6.5\mathrm{d})$$

6.2 Adjoint Variable Method

An alternative approach for sensitivity computation is the AVM. The AVM is very efficient when the number of parameters, N_{P}, is greater than the number of quantities of interest (QoIs), N_{QoI} [49, 50]. It has originally been applied for the analysis of electric networks [47] and only recently gained interest in the HV engineering community [51]. In this section, the AVM is derived for nonlinear transient coupled electrothermal problems.

The idea of the AVM is to avoid the separate computation of $\frac{\mathrm{d}\phi}{\mathrm{d}p_j}(\boldsymbol{p}_0)$ and $\frac{\mathrm{d}\theta}{\mathrm{d}p_j}(\boldsymbol{p}_0)$ for each parameter by a clever representation of the QoIs: Each QoI, G_k, is formulated as an integral over the computational domain in space and time, $\Omega \times [t_{\mathrm{s}}, t_{\mathrm{f}}]$, by means of a functional, g_k. Furthermore, the EQS equation (5.1) and the transient heat conduction equation (5.3) are substracted, multiplied by test functions $w_{\mathrm{el},k}$ and $w_{\mathrm{th},k}$, respectively:

$$G_k(\phi, \theta, \boldsymbol{p}) = \int_{t_{\mathrm{s}}}^{t_{\mathrm{f}}} \int_{\Omega} g_k(\phi, \theta, \boldsymbol{r}, t, \boldsymbol{p})\, \mathrm{d}\Omega \mathrm{d}t$$

$$-\int_{t_s}^{t_f}\int_\Omega w_{\text{el},k}(\boldsymbol{r},t)\,\underbrace{\left(\,\text{div}\left(\partial_t\boldsymbol{D}+\boldsymbol{J}\right)\right)}_{\overset{(5.1a)}{=}0}\,\text{d}\Omega\text{d}t$$

$$-\int_{t_s}^{t_f}\int_\Omega w_{\text{th},k}(\boldsymbol{r},t)\,\underbrace{\left(\partial_t\left(c_V\theta\right)+\text{div}\left(\dot{\boldsymbol{q}}\right)-\dot{q}_{\text{Joule}}\right)}_{\overset{(5.3a)}{=}0}\,\text{d}\Omega\text{d}t\,. \tag{6.6}$$

As indicated by the curved brackets, the additional terms are zero by construction. Consequently, the test functions, $w_{\text{el},k}$ and $w_{\text{th},k}$, can be chosen freely without changing the value of the QoIs. Taking the derivative of (6.6) to p_j yields:

$$\begin{aligned}
G_k'(\boldsymbol{p}_0) = &\underbrace{\int_{t_s}^{t_f}\int_\Omega \frac{\partial g_k}{\partial p_j}+\frac{\partial g_k}{\partial\phi}\phi'+\frac{\partial g_k}{\partial\theta}\theta'\,\text{d}\Omega\text{d}t}_{=:①}\\
&\underbrace{-\int_{t_s}^{t_f}\int_\Omega w_{\text{el},k}\,\text{div}\left(\boldsymbol{J}'\right)\,\text{d}\Omega\text{d}t}_{=:②}\underbrace{-\int_{t_s}^{t_f}\int_\Omega w_{\text{el},k}\,\text{div}\left(\frac{\partial\boldsymbol{D}'}{\partial t}\right)\,\text{d}\Omega\text{d}t}_{=:③}\\
&\underbrace{-\int_{t_s}^{t_f}\int_\Omega w_{\text{th},k}\,\text{div}\left(\dot{\boldsymbol{q}}'\right)\,\text{d}\Omega\text{d}t}_{=:④}\\
&\underbrace{-\int_{t_s}^{t_f}\int_\Omega w_{\text{th},k}\left(\frac{\partial}{\partial t}\left(\left(\frac{\partial c_V}{\partial p_j}+\frac{\partial c_V}{\partial\theta}\theta'\right)\theta+c_V\theta'\right)\right)\,\text{d}\Omega\text{d}t}_{=:⑤}\\
&\underbrace{-\int_{t_s}^{t_f}\int_\Omega w_{\text{th},k}p_{\text{Joule}}'\,\text{d}\Omega\text{d}t}_{=:⑥}\,.
\end{aligned} \tag{6.7}$$

The goal is to factor $\phi'(\boldsymbol{p}_0)$ and $\theta'(\boldsymbol{p}_0)$ out and choose $w_{\text{el},k}$ and $w_{\text{th},k}$ such that all unknown terms vanish. First, the second integral ② is investigated. Applying integration by parts leads to

$$② = \int_{t_s}^{t_f}\int_\Omega \text{grad}\left(w_{\text{el},k}\right)\cdot\boldsymbol{J}'\,\text{d}\Omega\text{d}t-\int_{t_s}^{t_f}\int_{\partial\Omega} w_{\text{el},k}\boldsymbol{J}'\cdot\text{d}\boldsymbol{S}\text{d}t \tag{6.8}$$

Substituting (6.2b) and (6.2d) brings up

$$② = \int_{t_s}^{t_f}\int_\Omega \text{grad}\left(w_{\text{el},k}\right)\cdot\left(\frac{\partial\sigma}{\partial p_j}\boldsymbol{E}-\overline{\overline{\sigma}}_\text{d}\,\text{grad}\left(\phi'\right)+\frac{\partial\sigma}{\partial\theta}\theta'\boldsymbol{E}\right)\,\text{d}\Omega\text{d}t$$

$$- \int_{t_{\mathrm{s}}}^{t_{\mathrm{f}}} \int_{\partial \Omega} w_{\mathrm{el},k} \boldsymbol{J}' \cdot \mathrm{d}\boldsymbol{S} \mathrm{d}t \tag{6.9}$$

A second time integrating by parts leads to

$$\begin{aligned}
② &= \int_{t_{\mathrm{s}}}^{t_{\mathrm{f}}} \int_{\Omega} \mathrm{grad}\left(w_{\mathrm{el},k}\right) \cdot \left(\frac{\partial \sigma}{\partial p_j} \boldsymbol{E} + \frac{\partial \sigma}{\partial \theta} \theta' \boldsymbol{E} \right) \mathrm{d}\Omega \mathrm{d}t \\
&+ \int_{t_{\mathrm{s}}}^{t_{\mathrm{f}}} \int_{\Omega} \mathrm{div}\left(\overline{\overline{\sigma}}_{\mathrm{d}} \mathrm{grad}\left(w_{\mathrm{el},k}\right)\right) \phi' \mathrm{d}\Omega \mathrm{d}t \\
&- \int_{t_{\mathrm{s}}}^{t_{\mathrm{f}}} \int_{\partial \Omega} w_{\mathrm{el},k} \boldsymbol{J}' \cdot \mathrm{d}\boldsymbol{S} \mathrm{d}t - \int_{t_{\mathrm{s}}}^{t_{\mathrm{f}}} \int_{\partial \Omega} \left(\overline{\overline{\sigma}}_{\mathrm{d}} \mathrm{grad}\left(w_{\mathrm{el},k}\right)\right) \phi' \cdot \mathrm{d}\boldsymbol{S} \mathrm{d}t \, .
\end{aligned} \tag{6.10}$$

In a similar manner, integral ④ can be rewritten as

$$\begin{aligned}
④ &= \int_{t_{\mathrm{s}}}^{t_{\mathrm{f}}} \int_{\Omega} \mathrm{grad}\left(w_{\mathrm{th},k}\right) \cdot \left(-\frac{\partial \lambda}{\partial p_j} \mathrm{grad}\left(\theta\right) - \frac{\partial \lambda}{\partial \theta} \theta' \, \mathrm{grad}\left(\theta\right) \right) \mathrm{d}\Omega \mathrm{d}t \\
&+ \int_{t_{\mathrm{s}}}^{t_{\mathrm{f}}} \int_{\Omega} \mathrm{div}\left(\lambda \, \mathrm{grad}\left(w_{\mathrm{th},k}\right)\right) \theta' \, \mathrm{d}\Omega \mathrm{d}t \\
&- \int_{t_{\mathrm{s}}}^{t_{\mathrm{f}}} \int_{\partial \Omega} w_{\mathrm{th},k} \dot{\boldsymbol{q}}' \cdot \mathrm{d}\boldsymbol{S} \mathrm{d}t - \int_{t_{\mathrm{s}}}^{t_{\mathrm{f}}} \int_{\partial \Omega} \theta' \lambda \, \mathrm{grad}\left(w_{\mathrm{th},k}\right) \cdot \mathrm{d}\boldsymbol{S} \mathrm{d}t \, .
\end{aligned} \tag{6.11}$$

Next, the third integral ③ is investigated. The differential operator is shifted from $\frac{\partial \boldsymbol{D}'}{\partial t}$ to the adjoint variable, $w_{\mathrm{el},k}$, using integration by parts,

$$③ = -\int_{t_{\mathrm{s}}}^{t_{\mathrm{f}}} \int_{\Omega} w_{\mathrm{el},k} \, \mathrm{div}\left(\frac{\partial \boldsymbol{D}'}{\partial t} \right) \mathrm{d}\Omega \mathrm{d}t \tag{6.12}$$

$$= \int_{t_{\mathrm{s}}}^{t_{\mathrm{f}}} \int_{\Omega} \mathrm{grad}\left(w_{\mathrm{el},k}\right) \cdot \frac{\partial \boldsymbol{D}'}{\partial t} \mathrm{d}\Omega \mathrm{d}t - \int_{t_{\mathrm{s}}}^{t_{\mathrm{f}}} \oint_{\partial \Omega} w_{\mathrm{el},k} \frac{\partial \boldsymbol{D}'}{\partial t} \cdot \mathrm{d}\boldsymbol{S} \mathrm{d}t \, . \tag{6.13}$$

Integration by parts in time removes the time derivative from $\boldsymbol{D}'$, i.e.,

$$\begin{aligned}
③ &= \int_{\Omega} \mathrm{grad}\left(w_{\mathrm{el},k}\right) \cdot \boldsymbol{D}' \, \mathrm{d}\Omega \Big|_{t=t_{\mathrm{f}}} - \int_{\Omega} \mathrm{grad}\left(w_{\mathrm{el},k}\right) \cdot \boldsymbol{D}' \, \mathrm{d}\Omega \Big|_{t=t_{\mathrm{s}}} \\
&- \int_{t_{\mathrm{s}}}^{t_{\mathrm{f}}} \int_{\Omega} \frac{\partial}{\partial t} \mathrm{grad}\left(w_{\mathrm{el},k}\right) \cdot \boldsymbol{D}' \, \mathrm{d}\Omega \mathrm{d}t - \int_{t_{\mathrm{s}}}^{t_{\mathrm{f}}} \oint_{\partial \Omega} w_{\mathrm{el},k} \frac{\partial \boldsymbol{D}'}{\partial t} \cdot \mathrm{d}\boldsymbol{S} \mathrm{d}t \, ,
\end{aligned} \tag{6.14}$$

where the integral evaluated at $t = t_{\mathrm{s}}$ is given through the sensitivity of the initial condition (6.2g). The third integral of (6.14) is further unravelled by inserting (6.2c) and (6.2d)

and integrating by parts, i.e.,

$$-\int_{t_\mathrm{s}}^{t_\mathrm{f}} \int_\Omega \frac{\partial}{\partial t}\,\mathrm{grad}\left(w_{\mathrm{el},k}\right)\cdot \boldsymbol{D}'\,\mathrm{d}\Omega\mathrm{d}t \tag{6.15}$$

$$=-\int_{t_\mathrm{s}}^{t_\mathrm{f}} \int_\Omega \frac{\partial}{\partial t}\,\mathrm{grad}\left(w_{\mathrm{el},k}\right)\left(\frac{\partial \varepsilon}{\partial p_j}\boldsymbol{E}-\bar{\bar{\varepsilon}}_\mathrm{d}\,\mathrm{grad}\left(\phi'\right)+\frac{\partial \varepsilon}{\partial \theta}\theta'\boldsymbol{E}\right)\,\mathrm{d}\Omega\mathrm{d}t \tag{6.16}$$

$$=-\int_{t_\mathrm{s}}^{t_\mathrm{f}} \int_\Omega \frac{\partial}{\partial t}\,\mathrm{grad}\left(w_{\mathrm{el},k}\right)\cdot\left(\frac{\partial \varepsilon}{\partial p_j}\boldsymbol{E}+\frac{\partial \varepsilon}{\partial \theta}\theta'\boldsymbol{E}\right)+\mathrm{div}\left(\bar{\bar{\varepsilon}}_\mathrm{d}\frac{\partial}{\partial t}\,\mathrm{grad}\left(w_{\mathrm{el},k}\right)\right)\phi'\,\mathrm{d}\Omega\mathrm{d}t$$

$$+\int_{t_\mathrm{s}}^{t_\mathrm{f}} \int_{\partial\Omega} \bar{\bar{\varepsilon}}_\mathrm{d}\frac{\partial}{\partial t}\,\mathrm{grad}\left(w_{\mathrm{el},k}\right)\phi'\cdot\mathrm{d}\boldsymbol{S}\mathrm{d}t\,.$$

$$\tag{6.17}$$

The boundary integrals occurring in (6.10),(6.11),(6.14) and (6.17) can be simplified using (6.2e), (6.2f), (6.4c) and (6.4d), i.e.

$$-\int_{\partial\Omega} w_{\mathrm{el},k}\left(\boldsymbol{J}+\frac{\partial \boldsymbol{D}''}{\partial t}\right)\cdot\mathrm{d}\boldsymbol{S} \overset{(6.2\mathrm{f})}{=} -\int_{t_\mathrm{s}}^{t_\mathrm{f}} \int_{\Gamma_{\mathrm{D,el}}} w_{\mathrm{el},k}\left(\boldsymbol{J}'+\frac{\partial \boldsymbol{D}'}{\partial t}\right)\cdot\mathrm{d}\boldsymbol{S}\mathrm{d}t\,; \tag{6.18}$$

$$-\int_{\partial\Omega} \left(\bar{\bar{\sigma}}_\mathrm{d}\,\mathrm{grad}\left(w_{\mathrm{el},k}\right)\right)\phi'\cdot\mathrm{d}\boldsymbol{S} \overset{(6.2\mathrm{e})}{=} -\int_{\Gamma_{\mathrm{N,el}}} \left(\bar{\bar{\sigma}}_\mathrm{d}\,\mathrm{grad}\left(w_{\mathrm{el},k}\right)\right)\phi'\cdot\mathrm{d}\boldsymbol{S}\,; \tag{6.19}$$

$$\int_{\partial\Omega} \left(\bar{\bar{\varepsilon}}_\mathrm{d}\frac{\partial}{\partial t}\,\mathrm{grad}\left(w_{\mathrm{el},k}\right)\right)\phi'\cdot\mathrm{d}\boldsymbol{S} \overset{(6.2\mathrm{e})}{=} \int_{\Gamma_{\mathrm{N,el}}} \left(\bar{\bar{\varepsilon}}_\mathrm{d}\frac{\partial}{\partial t}\,\mathrm{grad}\left(w_{\mathrm{el},k}\right)\right)\phi'\cdot\mathrm{d}\boldsymbol{S}\,; \tag{6.20}$$

$$-\int_{\partial\Omega} w_{\mathrm{th},k}\dot{\boldsymbol{q}}'\cdot\mathrm{d}\boldsymbol{S} \overset{(6.4\mathrm{d})}{=} -\int_{\Gamma_{\mathrm{D,th}}} w_{\mathrm{th},k}\dot{\boldsymbol{q}}'\cdot\mathrm{d}\boldsymbol{S}\,; \tag{6.21}$$

$$-\int_{\partial\Omega} \theta'\lambda\,\mathrm{grad}\left(w_{\mathrm{th},k}\right)\cdot\mathrm{d}\boldsymbol{S} \overset{(6.4\mathrm{c})}{=} -\int_{\Gamma_{\mathrm{N,th}}} \theta'\lambda\,\mathrm{grad}\left(w_{\mathrm{th},k}\right)\cdot\mathrm{d}\boldsymbol{S}\,. \tag{6.22}$$

Next, integral ⑤ is investigated. Integration by parts in time removes the time derivative from θ', i.e.,

$$⑤ = -\int_{t_\mathrm{s}}^{t_\mathrm{f}} \int_\Omega w_{\mathrm{th},k}\left(\frac{\partial}{\partial t}\left(\left(\frac{\partial c_\mathrm{V}}{\partial p_j}+\frac{\partial c_\mathrm{V}}{\partial \theta}\theta'\right)\theta+c_\mathrm{V}\theta'\right)\right)\,\mathrm{d}\Omega\mathrm{d}t$$

$$=\int_{t_\mathrm{s}}^{t_\mathrm{f}} \int_\Omega \frac{\partial w_{\mathrm{th},k}}{\partial t}\left(\left(\frac{\partial c_\mathrm{V}}{\partial p_j}+\frac{\partial c_\mathrm{V}}{\partial \theta}\theta'\right)\theta+c_\mathrm{V}\theta'\right)\,\mathrm{d}\Omega\mathrm{d}t$$

$$-\int_\Omega w_{\mathrm{th},k}\left(c_\mathrm{V}\theta\right)'\,\mathrm{d}\Omega\bigg|_{t=t_\mathrm{f}}+\int_\Omega w_{\mathrm{th},k}\left(c_\mathrm{V}\theta\right)'\,\mathrm{d}\Omega\bigg|_{t=t_\mathrm{s}}$$

$$= \int_{t_s}^{t_f} \int_\Omega \frac{\partial w_{\text{th},k}}{\partial t} \left(\left(\frac{\partial c_V}{\partial p_j} + \frac{\partial c_V}{\partial \theta} \theta' \right) \theta + c_V \theta' \right) \, \mathrm{d}\Omega \mathrm{d}t$$

$$- \int_\Omega w_{\text{th},k} \left(c_V \theta \right)' \, \mathrm{d}\Omega \Big|_{t=t_f}$$

$$+ \int_\Omega w_{\text{th},k} \left(\left(\frac{\partial c_V}{\partial p_j} + \frac{\partial c_V}{\partial \theta} \theta' \right) \theta + c_V \theta' \right) \, \mathrm{d}\Omega \Big|_{t=t_s}, \tag{6.23}$$

where the sensitivity of the temperature at $t = t_s$ is given by (6.4e). The sensitivity can now be written as

$$G_k'(\boldsymbol{p}_0) = \int_{t_s}^{t_f} \int_\Omega \frac{\partial g_k}{\partial p_j} + \mathrm{grad}\, (w_{\text{el},k}) \cdot \frac{\partial \sigma}{\partial p_j} \boldsymbol{E} - \frac{\partial}{\partial t} \mathrm{grad}\, (w_{\text{el},k}) \cdot \frac{\partial \varepsilon}{\partial p_j} \boldsymbol{E} \, \mathrm{d}\Omega \mathrm{d}t$$

$$+ \int_{t_s}^{t_f} \int_\Omega - \mathrm{grad}\, (w_{\text{th},k}) \cdot \frac{\partial \lambda}{\partial p_j} \mathrm{grad}\, (\theta) + w_{\text{th},k} \frac{\partial \sigma}{\partial p_j} E^2 + \frac{\partial w_{\text{th},k}}{\partial t} \frac{\partial c_V}{\partial p_j} \theta \, \mathrm{d}\Omega \mathrm{d}t$$

$$+ \int_{t_s}^{t_f} \int_\Omega \frac{\partial g_k}{\partial \phi} \phi' + \mathrm{div}\, \left(\bar{\bar{\sigma}}_d \, \mathrm{grad}\, (w_{\text{el},k}) \right) \phi' \, \mathrm{d}\Omega \mathrm{d}t$$

$$+ \int_{t_s}^{t_f} \int_\Omega - \mathrm{div}\, \left(\bar{\bar{\varepsilon}}_d \frac{\partial}{\partial t} \mathrm{grad}\, (w_{\text{el},k}) \right) \phi' \, \mathrm{d}\Omega \mathrm{d}t$$

$$+ \int_{t_s}^{t_f} \int_\Omega - \mathrm{div}\, \left(w_{\text{th},k} \left(\bar{\bar{\sigma}}_d \boldsymbol{E} + \boldsymbol{J} \right) \right) \phi' \, \mathrm{d}\Omega \mathrm{d}t$$

$$+ \int_{t_s}^{t_f} \int_\Omega \frac{\partial g_k}{\partial \theta} \theta' + \mathrm{div}\, \left(\lambda \, \mathrm{grad}\, (w_{\text{th},k}) \right) \theta' \, \mathrm{d}\Omega \mathrm{d}t$$

$$+ \int_{t_s}^{t_f} \int_\Omega + w_{\text{th},k} \frac{\partial \sigma}{\partial \theta} E^2 \theta' + \frac{\partial w_{\text{th},k}}{\partial t} \frac{\partial c_V}{\partial \theta} \theta \theta' + \frac{\partial w_{\text{th},k}}{\partial t} c_V \theta' \, \mathrm{d}\Omega \mathrm{d}t$$

$$+ \int_{t_s}^{t_f} \int_\Omega \mathrm{grad}\, (w_{\text{el},k}) \cdot \frac{\partial \sigma}{\partial \theta} \boldsymbol{E} \theta' - \frac{\partial}{\partial t} \mathrm{grad}\, (w_{\text{el},k}) \cdot \frac{\partial \varepsilon}{\partial \theta} \boldsymbol{E} \theta' \, \mathrm{d}\Omega \mathrm{d}t$$

$$+ \int_{t_s}^{t_f} \int_\Omega - \mathrm{grad}\, (w_{\text{th},k}) \cdot \frac{\partial \lambda}{\partial \theta} \mathrm{grad}\, (\theta) \, \theta' \, \mathrm{d}\Omega \mathrm{d}t$$

$$+ \int_{t_s}^{t_f} \int_{\Gamma_{\text{D,el}}} - w_{\text{el},k} \left(\boldsymbol{J}' + \frac{\partial \boldsymbol{D}'}{\partial t} \right) \cdot \mathrm{d}\boldsymbol{S} \mathrm{d}t$$

$$+ \int_{t_s}^{t_f} \int_{\Gamma_{\text{N,el}}} \left(-\bar{\bar{\sigma}}_d \, \mathrm{grad}\, (w_{\text{el},k}) \, \phi' + \bar{\bar{\varepsilon}}_d \frac{\partial}{\partial t} \mathrm{grad}\, (w_{\text{el},k}) \, \phi' \right) \cdot \mathrm{d}\boldsymbol{S} \mathrm{d}t$$

$$+ \int_{t_\mathrm{s}}^{t_\mathrm{f}} \int_{\Gamma_{\mathrm{N,el}}} \textcolor{red}{\phi'} w_{\mathrm{th},k} \left(\overline{\overline{\sigma}}_\mathrm{d} \boldsymbol{E} + \boldsymbol{J} \right) \cdot \mathrm{d}\boldsymbol{S}\mathrm{d}t$$

$$- \int_{t_\mathrm{s}}^{t_\mathrm{f}} \int_{\Gamma_{\mathrm{D,th}}} w_{\mathrm{th},k} \textcolor{red}{\dot{\boldsymbol{q}}'} \cdot \mathrm{d}\boldsymbol{S}\mathrm{d}t - \int_{t_\mathrm{s}}^{t_\mathrm{f}} \int_{\Gamma_{\mathrm{N,th}}} \textcolor{red}{\theta'} \lambda \,\mathrm{grad}\,(w_{\mathrm{th},k}) \cdot \mathrm{d}\boldsymbol{S}\mathrm{d}t$$

$$+ \int_\Omega \mathrm{grad}\,(w_{\mathrm{el},k}) \cdot \textcolor{red}{\boldsymbol{D}'} \,\mathrm{d}\Omega \bigg|_{t=t_\mathrm{f}} - \int_\Omega \mathrm{grad}\,(w_{\mathrm{el},k}) \cdot \textcolor{red}{\boldsymbol{D}'} \,\mathrm{d}\Omega \bigg|_{t=t_\mathrm{s}}$$

$$- \int_\Omega w_{\mathrm{th},k} \left(c_\mathrm{V}\theta \right)' \,\mathrm{d}\Omega \bigg|_{t=t_\mathrm{f}}$$

$$+ \int_\Omega w_{\mathrm{th},k} \left(\left(\frac{\partial c_\mathrm{V}}{\partial p_j} + \frac{\partial c_\mathrm{V}}{\partial \theta} \textcolor{red}{\theta'} \right) \theta + c_\mathrm{V} \textcolor{red}{\theta'} \right) \mathrm{d}\Omega \bigg|_{t=t_\mathrm{s}}, \tag{6.24}$$

where all unknown terms are highlighted in red and blue, respectively. The aim is for all unknown terms to vanish and cancel each other out. This yields the so-called adjoint problem, which is a linear coupled system of PDEs for the test functions $w_{\mathrm{el},k}$ and $w_{\mathrm{th},k}$, i.e.,

$$\mathrm{div} \left(\overline{\overline{\varepsilon}}_\mathrm{d} \frac{\partial}{\partial t} \,\mathrm{grad}\,(w_{\mathrm{el},k}) \right)$$

$$- \mathrm{div} \left(\overline{\overline{\sigma}}_\mathrm{d} \,\mathrm{grad}\,(w_{\mathrm{el},k}) \right)$$

$$+ \mathrm{div} \left(w_{\mathrm{th},k} \left(\overline{\overline{\sigma}}_\mathrm{d} \boldsymbol{E} + \boldsymbol{J} \right) \right) = \frac{\partial g_k}{\partial \phi}, \; t \in [t_\mathrm{s}, t_\mathrm{f}], \; \boldsymbol{r} \in \Omega \,; \tag{6.25a}$$

$$w_{\mathrm{el},k} = 0 \quad , \; t \in [t_\mathrm{s}, t_\mathrm{f}], \; \boldsymbol{r} \in \Gamma_{\mathrm{D,el}} \,; \tag{6.25b}$$

$$\left(-\overline{\overline{\sigma}}_\mathrm{d} \,\mathrm{grad}\,(w_{\mathrm{el},k}) + \overline{\overline{\varepsilon}}_\mathrm{d} \frac{\partial}{\partial t} \,\mathrm{grad}\,(w_{\mathrm{el},k}) \right.$$

$$\left. + w_{\mathrm{th},k} \left(\overline{\overline{\sigma}}_\mathrm{d} \boldsymbol{E} + \boldsymbol{J} \right) \right) \cdot \boldsymbol{n}_{\mathrm{el}} = 0 \quad , \; t \in [t_\mathrm{s}, t_\mathrm{f}], \; \boldsymbol{r} \in \Gamma_{\mathrm{N,el}} \,; \tag{6.25c}$$

$$w_{\mathrm{el},k} = 0 \quad , \; t = t_\mathrm{f} \quad , \; \boldsymbol{r} \in \Omega \,, \tag{6.25d}$$

and

$$
\begin{aligned}
&\frac{\partial}{\partial t}\operatorname{grad}\left(w_{\mathrm{el},k}\right)\cdot\frac{\partial\varepsilon}{\partial\theta}\boldsymbol{E}\\
&-\operatorname{grad}\left(w_{\mathrm{el},k}\right)\cdot\frac{\partial\sigma}{\partial\theta}\boldsymbol{E}\\
&-\frac{\partial w_{\mathrm{th},k}}{\partial t}\left(c_{\mathrm{V}}+\frac{\partial c_{\mathrm{V}}}{\partial\theta}\theta\right)\\
&-\operatorname{div}\left(\lambda\operatorname{grad}\left(w_{\mathrm{th},k}\right)\right)\\
&+\operatorname{grad}\left(w_{\mathrm{th},k}\right)\cdot\frac{\partial\lambda}{\partial\theta}\operatorname{grad}\left(\theta\right)\\
&\qquad -w_{\mathrm{th},k}\frac{\partial\sigma}{\partial\theta}E^{2}=\frac{\partial g_{k}}{\partial\theta},\ \ t\in[t_{\mathrm{s}},t_{\mathrm{f}}],\ \boldsymbol{r}\in\Omega\,;
\end{aligned}
\tag{6.26a}
$$

$$
w_{\mathrm{th},k}=0 \quad,\ t\in[t_{\mathrm{s}},t_{\mathrm{f}}],\ \boldsymbol{r}\in\Gamma_{\mathrm{D,th}}\,;
\tag{6.26b}
$$

$$
-\lambda\operatorname{grad}\left(w_{\mathrm{th},k}\right)\cdot\boldsymbol{n}_{\mathrm{th}}=0 \quad,\ t\in[t_{\mathrm{s}},t_{\mathrm{f}}],\ \boldsymbol{r}\in\Gamma_{\mathrm{N,th}}\,;
\tag{6.26c}
$$

$$
w_{\mathrm{th},k}=0 \quad t=t_{\mathrm{f}} \quad,\ \boldsymbol{r}\in\Omega\,.
\tag{6.26d}
$$

Once the test functions $w_{\mathrm{el},k}$ and $w_{\mathrm{th},k}$ are computed as the solution of the adjoint problem, the sensitivity simplifies from (6.24) to

$$
\begin{aligned}
G_{k}(\boldsymbol{p}_{0})'=&\int_{t_{\mathrm{s}}}^{t_{\mathrm{f}}}\int_{\Omega}\frac{\partial g_{k}}{\partial p_{j}}\,\mathrm{d}\Omega\mathrm{d}t\\
&+\int_{t_{\mathrm{s}}}^{t_{\mathrm{f}}}\int_{\Omega}-\frac{\partial}{\partial t}\operatorname{grad}\left(w_{\mathrm{el},k}\right)\cdot\frac{\partial\varepsilon}{\partial p_{j}}\boldsymbol{E}+\operatorname{grad}\left(w_{\mathrm{el},k}\right)\cdot\frac{\partial\sigma}{\partial p_{j}}\boldsymbol{E}\,\mathrm{d}\Omega\mathrm{d}t\\
&+\int_{t_{\mathrm{s}}}^{t_{\mathrm{f}}}\int_{\Omega}\frac{\partial w_{\mathrm{th},k}}{\partial t}\frac{\partial c_{\mathrm{V}}}{\partial p_{j}}\theta\,\mathrm{d}\Omega\mathrm{d}t\\
&+\int_{t_{\mathrm{s}}}^{t_{\mathrm{f}}}\int_{\Omega}w_{\mathrm{th},k}\frac{\partial\sigma}{\partial p_{j}}E^{2}-\operatorname{grad}\left(w_{\mathrm{th},k}\right)\cdot\frac{\partial\lambda}{\partial p_{j}}\operatorname{grad}\left(\theta\right)\,\mathrm{d}\Omega\mathrm{d}t\\
&-\int_{\Omega}\operatorname{grad}\left(w_{\mathrm{el},k}\right)\cdot\boldsymbol{D}'\,\mathrm{d}\Omega\bigg|_{t=t_{\mathrm{s}}}\\
&+\int_{\Omega}w_{\mathrm{th},k}\left(\left(\frac{\partial c_{\mathrm{V}}}{\partial p_{j}}+\frac{\partial c_{\mathrm{V}}}{\partial\theta}\theta'\right)\theta+c_{\mathrm{V}}\theta'\right)\,\mathrm{d}\Omega\bigg|_{t=t_{\mathrm{s}}}.
\end{aligned}
\tag{6.27}
$$

This means that once the test functions $w_{\mathrm{el},k}$ and $w_{\mathrm{th},k}$ are available, the sensitivity of a QoI G_{k} with respect to any parameter p_{j} can be computed simply by post-

processing, i.e. by evaluating (6.27). Since the the adjoint problem (6.25) and (6.26) depends only on the QoI and not on the parameter under investigation, the AVM requires the solution of just one additional linear PDE system for each QoI, regardless of the number of parameters, N_p.

6.3 Numerical Approach

The electric scalar potential and the temperature are discretized according to (4.5) and (4.6), respectively. Furthermore, the following spatial discretizations are applied:

$$\phi'(\boldsymbol{r}, t) \approx \sum_r u'_r(t) N_r(\boldsymbol{r}) \,; \tag{6.28a}$$

$$\theta'(\boldsymbol{r}, t) \approx \sum_r v'_r(t) N_r(\boldsymbol{r}) \,; \tag{6.28b}$$

$$w_{\mathrm{el},k}(\boldsymbol{r}, t) \approx \sum_r w_{\mathrm{el},k,j}(t) N_r(\boldsymbol{r}) \,; \tag{6.28c}$$

$$w_{\mathrm{th},k}(\boldsymbol{r}, t) \approx \sum_r w_{\mathrm{th},k,j}(t) N_r(\boldsymbol{r}) \,. \tag{6.28d}$$

The semi-discrete counterpart of the adjoint formulation, (6.25) and (6.26), reads

$$-\boldsymbol{K}_{\bar{\bar{\varepsilon}}_\mathrm{d}} \frac{\partial}{\partial t} \boldsymbol{w}_{\mathrm{el},\boldsymbol{k}} + \boldsymbol{K}_{\bar{\bar{\sigma}}_\mathrm{d}} \boldsymbol{w}_{\mathrm{el},\boldsymbol{k}} - \boldsymbol{A}^T_{\boldsymbol{J}+\bar{\bar{\sigma}}_\mathrm{d} \boldsymbol{E}} \boldsymbol{w}_{\mathrm{th},\boldsymbol{k}} = \boldsymbol{x}_{\mathrm{el}} \,; \tag{6.29a}$$

$$\boldsymbol{A}_{\frac{\partial \varepsilon}{\partial \theta} \boldsymbol{E}} \frac{\partial}{\partial t} \boldsymbol{w}_{\mathrm{el},\boldsymbol{k}} - \boldsymbol{A}_{\frac{\partial \sigma}{\partial \theta} \boldsymbol{E}} \boldsymbol{w}_{\mathrm{el},\boldsymbol{k}} - \boldsymbol{M}_{c_\mathrm{V}+\frac{\partial c_\mathrm{V}}{\partial \theta} \theta} \frac{\partial}{\partial t} \boldsymbol{w}_{\mathrm{th},\boldsymbol{k}}$$
$$+ \left(\boldsymbol{K}_\lambda - \boldsymbol{A}_{-\frac{\partial \lambda}{\partial \theta} \mathrm{grad}(\theta)} - \boldsymbol{M}_{\frac{\partial \sigma}{\partial \theta} E^2} \right) \boldsymbol{w}_{\mathrm{th},\boldsymbol{k}} = \boldsymbol{x}_{\mathrm{th}} \,, \tag{6.29b}$$

with the FE operators

$$[\boldsymbol{A}_{(\cdot)}]_{rs} = \int_\Omega (\cdot) \cdot \mathrm{grad}\,(N_s)\, N_r\, \mathrm{d}\Omega \,; \tag{6.30a}$$

$$[\boldsymbol{x}_{\mathrm{el}}]_r = \int_\Omega \frac{\partial g_k}{\partial u_r}\, \mathrm{d}\Omega \,; \tag{6.30b}$$

$$[\boldsymbol{x}_{\text{th}}]_r = \int_{\Omega} \frac{\partial g_k}{\partial v_r} \, \mathrm{d}\Omega \,, \tag{6.30c}$$

which are assembled for $r, s = 1, ..., N_{\text{node}}$. The adjoint problem is implemented for axisymmetric problems in *Pyrit* [19]. A multi-rate coupling scheme with implicit Euler time-stepping is performed [44]. The coupling between (6.29a) and (6.29b) is resolved using the successive substitution method. Since the adjoint problem provides terminal conditions instead of initial conditions, i.e. (6.25d), (6.26d) are defined at the terminal simulation time t_{f}, the time-stepping is performed backwards in time [52, 49]. The semi-discrete counterpart of (6.27) is given by

$$
\begin{aligned}
\frac{\mathrm{d}G_k}{\mathrm{d}p_j}(\boldsymbol{p}_0) = {} & \int_0^{t_{\text{f}}} \int_{\Omega} \frac{\partial g}{\partial p_j} \, \mathrm{d}\Omega \mathrm{d}t \\
& - \int_0^{t_{\text{f}}} \boldsymbol{u}^T K_{\frac{\partial \sigma}{\partial p_j}} \boldsymbol{w}_{\text{el},\boldsymbol{k}} \mathrm{d}t \\
& + \int_0^{t_{\text{f}}} \boldsymbol{u}^T K_{\frac{\partial \varepsilon}{\partial p_j}} \frac{\partial}{\partial t} \boldsymbol{w}_{\text{el},\boldsymbol{k}} \mathrm{d}t \\
& + \int_0^{t_{\text{f}}} \boldsymbol{v}^T \boldsymbol{M}_{\frac{\partial c_{\text{V}}}{\partial p_j}} \frac{\partial}{\partial t} \boldsymbol{w}_{\text{th},\boldsymbol{k}} \mathrm{d}t \\
& + \int_0^{t_{\text{f}}} \frac{\partial}{\partial t} \boldsymbol{w}_{\text{th},\boldsymbol{k}}^T \boldsymbol{s}_{\frac{\partial \sigma}{\partial p_j} E^2} \mathrm{d}t \\
& + \int_0^{t_{\text{f}}} -\boldsymbol{v}^T K_{\frac{\partial \lambda}{\partial p_j}} \boldsymbol{w}_{\text{th},\boldsymbol{k}} \mathrm{d}t \\
& + \boldsymbol{u}^T K_{\frac{\partial \varepsilon}{\partial p_j}} \boldsymbol{w}_{\text{el},\boldsymbol{k}} \Big|_{t=t_{\text{s}}} + (\boldsymbol{u}')^T K_{\overline{\overline{\varepsilon}}_{\text{d}}} \boldsymbol{w}_{\text{el},\boldsymbol{k}} \Big|_{t=t_{\text{s}}} \\
& + \boldsymbol{u}^T K_{\frac{\partial \varepsilon}{\partial \theta} \frac{\mathrm{d}T}{\mathrm{d}p}} \boldsymbol{w}_{\text{el},\boldsymbol{k}} \Big|_{t=t_{\text{s}}} \\
& + \boldsymbol{v}^T \boldsymbol{M}_{\frac{\partial c_{\text{V}}}{\partial p_j} + \frac{\partial c_{\text{V}}}{\partial T} \frac{\mathrm{d}T}{\mathrm{d}p_j}} \boldsymbol{w}_{\text{th},\boldsymbol{k}} \Big|_{t=t_{\text{s}}} \\
& + (\boldsymbol{v}')^T \boldsymbol{M}_{c_{\text{V}}} \boldsymbol{w}_{\text{th},\boldsymbol{k}} \Big|_{t=t_{\text{s}}} \tag{6.31}
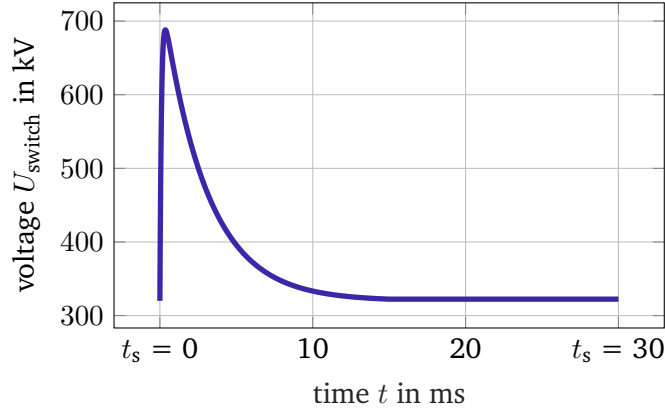\end{aligned}
$$

Figure 6.1: The switching impulse over the simulated time span $[t_s, t_f] = [0, 30\,\text{ms}]$.

6.4 Method Validation

In this section, the AVM presented in the previous section is validated. The method is applied to the 320 kV cable joint specimen and the results are compared to results obtained via the DSM as well as results obtained via finite difference computations in COMSOL Multiphysics®.

The cable joint is investigated during the switching overvoltage event described in Ch. 5. The impulse over the simulated time span $[t_s, t_f] = [0, 30\,\text{ms}]$ is shown in Fig. 6.1. Furthermore, a fixed conductor temperature of 65°C is assumed, which is the mean conductor temperature obtained in the simulation results of Ch. 5.

The validation is performed by investigating the sensitivity of the Joule heat, $G_{\text{Joule}} = \int_{t_s}^{t_f} P_{\text{Joule}}\,\mathrm{d}t$, with respect to the material parameters of the FGM, i.e. p_1 to p_5 of (3.1). This is motivated by the findings of [38] and [12], where it has been demonstrated that inappropriate choices for p_1 to p_5 can result in a substantial elevation of the Joule heat and consequently a significant temperature increase (see Fig. 6.2). To apply the AVM, the Joule heat is written in terms of a functional g_{Joule},

$$G_{\text{Joule}}(\phi, \theta, \boldsymbol{p}) = \int_{t_s}^{t_f} \int_{\Omega} g_{\text{Joule}}(\phi, \theta, \boldsymbol{r}, t, \boldsymbol{p})\,\mathrm{d}\Omega\,\mathrm{d}t = \int_{t_s}^{t_f} \int_{\Omega} p_{\text{Joule}}\,\mathrm{d}\Omega\,\mathrm{d}t\,. \qquad (6.32)$$
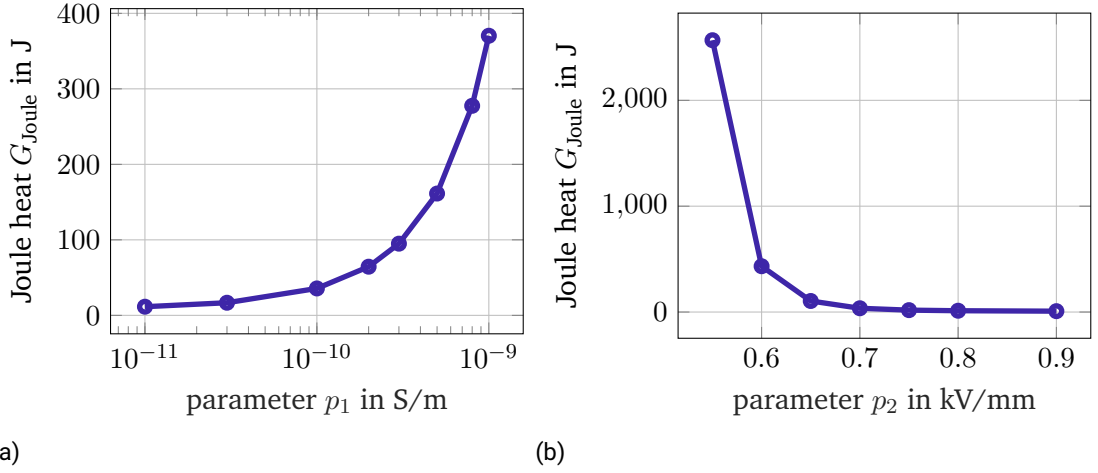
Figure 6.2: Joule heat as an exemplary QoI for (a) different values of p_1 and (b) different values of p_2.

Note that this integral notation does not restrict the choice of QoIs. QoIs that may not inherently be expressed as integral can be effectively represented using Dirac delta functions, δ, within the integral expression. For example, the temperature $\theta(\boldsymbol{r}_{\mathrm{QoI}}, t_{\mathrm{QoI}})$ at a particular position, $\boldsymbol{r}_{\mathrm{QoI}}$, and time instance, t_{QoI}, reads in integral notation:

$$G_{\theta(\boldsymbol{r}_{\mathrm{QoI}}, t_{\mathrm{QoI}})}(\phi, \theta, \boldsymbol{p}) = \int_{\Omega} \int_{t_{\mathrm{s}}}^{t_{\mathrm{f}}} \theta(\boldsymbol{r}, t)\delta(\boldsymbol{r} - \boldsymbol{r}_{\mathrm{QoI}})\delta(t - t_{\mathrm{QoI}}) \, \mathrm{d}\Omega \, \mathrm{d}t \,. \tag{6.33}$$

For more information on QoIs that are evaluated at specific points in space or time and the numeric implications, see [21]. The QoI-dependent parts of the FE formulation are defined by

$$\int_{\Omega} \frac{\partial g_{\mathrm{Joule}}}{\partial p_j} \, \mathrm{d}\Omega \approx \boldsymbol{u}^T \boldsymbol{K}_{\frac{\partial \sigma}{\partial p}} \boldsymbol{u} \tag{6.34a}$$

$$\boldsymbol{x}_{\mathrm{el}} = \boldsymbol{u}^T (\boldsymbol{K}_{\sigma} + \boldsymbol{K}_{\overline{\overline{\sigma}}_{\mathrm{d}}}) \tag{6.34b}$$

$$\boldsymbol{x}_{\mathrm{th}} = \boldsymbol{s}_{\frac{\partial \sigma}{\partial T} E^2} \tag{6.34c}$$

The results are collected in Table 6.1. The sensitivities are both positive and negative and their absolute values vary substantially. Comparing the absolute value of the sensitivity to p_1 and p_2, respectively, indicates that the QoI is much more sensitive to changes in p_1 compared to p_2. However, the comparison of the sensitivities should take the absolute value of the parameters into account. This can be done for example by using a first order Taylor series approximation of the QoI's dependence on the parameters,

$$G_{\text{Joule}}(p_j) \approx G_{\text{Joule}}(p_{0,j}) + \frac{\mathrm{d}G_{\text{Joule}}}{\mathrm{d}p_j}(p_{0,j})\Delta p_j, \quad j = 1,...,5\,,$$

where $\Delta p_j = p_j - p_{0,j}$ is the perturbation of the j-th parameter. The Taylor series can be used to estimate the relative change of a QoI that occurs for an increase of a parameter $\Delta p_j = 1\% p_{0,j}$, i.e.

$$\Delta G_{1\%,j} := \frac{\Delta G_{\text{Joule}}}{G_{\text{Joule}}(p_{0,j}} \approx \frac{\mathrm{d}G_{\text{Joule}}}{\mathrm{d}p_j}(p_{0,j})\frac{1\% p_{0,j}}{G_{\text{Joule}}(p_{0,j})}\,, \tag{6.35}$$

with $\Delta G_{\text{Joule}} = G_{\text{Joule}}(p_{0,j} + \Delta p_j) - G_{\text{Joule}}(p_{0,j})$. The normalized sensitivities are brought together in Table 6.2. Comparing the normalized value of the sensitivity to p_1 and p_2 now shows that the QoI actually is much more sensitive towards relatively small changes in p_2 compared to p_1 (see Fig. 6.4a and Fig. 6.4b). In fact, p_2 appears to be the most influential design parameter. The significant impact of p_2 can be understood by considering its influence on the nonlinear conductivity characteristic. Figure 6.3 shows that p_2 determines the field strength at which the electric conductivity transitions from the constant base conductivity to the nonlinear region. Additionally, small values of p_2 increase the slope of the conductivity rise. Consequently, reducing p_2 results in a local increase of the conductivity by several orders of magnitude and, therefore, significantly greater Joule heat.

Finally, the adjoint formulation (6.25) and (6.26) is validated by comparing the sensitivities of the Joule heat obtained by the AVM to two reference solutions. The first reference solution is obtained by finite difference computations using

Table 6.1: Sensitivities of the Joule heat with respect to the parameters p_1 to p_5 of the nonlinear FGM conductivity defined by (3.1).

Parameter p_j	Value $p_{0,j}$	Sensitivity $\frac{\mathrm{d}G}{\mathrm{d}p_j}(\boldsymbol{p}_0)$
p_1	1.0e-10 S/m	2.76e+11 kJ/(S/m)
p_2	0.70 kV/mm	-6.28e-4 kJ/(kV/mm)
p_3	2.4 kV/mm	2.38e-8 kJ/(kV/mm)
p_4	1900	1.65e+2 kJ
p_5	3700	1.01e+2 kJ

COMSOL Multiphysics®. The second reference solution is computed using the DSM which is also implemented in *Pyrit*. Fig. 6.5 shows that the results agree for all parameters. Hence, the method is successfully validated.

Figure 6.6 investigates the convergence behavior of the AVM. Figure 6.6a shows that the relative error, ϵ_{rel}, of the sensitivity $\frac{\mathrm{d}G}{\mathrm{d}p_2}(\boldsymbol{p}_0)$ of the Joule losses to p_2 converges quadratically with respect to the maximum edge length inside the 2D triangular mesh. In order to achieve a relative error below one 1%, mesh consisting of 24722 nodes and 52544 elements is selected for all computations.

Figure 6.6b shows the relative error, ϵ_{rel}, of the sensitivity $\frac{\mathrm{d}G}{\mathrm{d}p_1}(\boldsymbol{p}_0)$ of the Joule losses to p_2 with respect to the time step size. As expected for the implicit Euler method, the relative error converges quadratically with respect to the time step size. With a maximum step size of $\Delta t_{\mathrm{max}} = \Delta t_{\mathrm{el,max}} = \Delta t_{\mathrm{th,max}} = 0.56\,\mathrm{ms}$, a relative error below $0.1\,\%$ can be achieved. It furthermore shows the convergence of the sensitivity with respect to the maximum thermal time step, $\Delta t_{\mathrm{th,max}}$, while the maximum electric time step is fixed at $\Delta t_{\mathrm{el,max}} = 0.56\,\mathrm{ms}$. The thermal time step can be chosen approximately 5.4 times larger than the electric time step without loss of accuracy, demonstrating the benefits of a multi-rate time-integration approach. The AVM is, thus, successfully validated, which is an important step towards the optimization of FGMs in HVDC cable joints.

Table 6.2: Normalized sensitivities according to (6.35) of the Joule heat with respect to the parameters p_1 to p_5 of the nonlinear FGM conductivity defined by (3.1).

Parameter	Normalized sensitivity
p_j	$\Delta G_{1\%,j}$
p_1	$0.780\,\%$
p_2	$-12.4\,\%$
p_3	$1.61\text{e-}3\,\%$
p_4	$0.870\,\%$
p_5	$1.06\,\%$
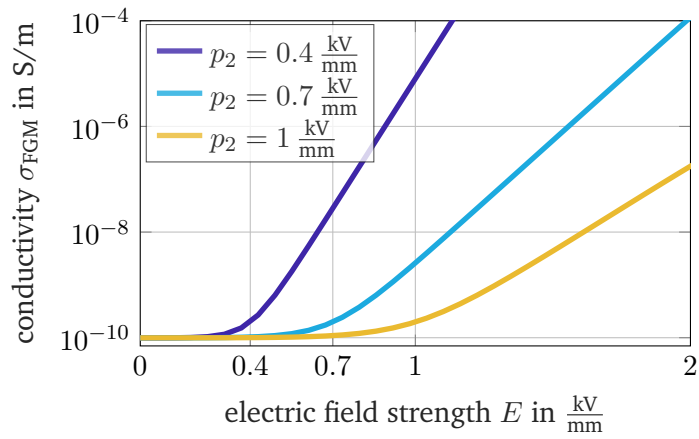
Figure 6.3: Field-dependence of the nonlinear conductivity defined for different values of the switching field strength, p_2.

(a)

(b)
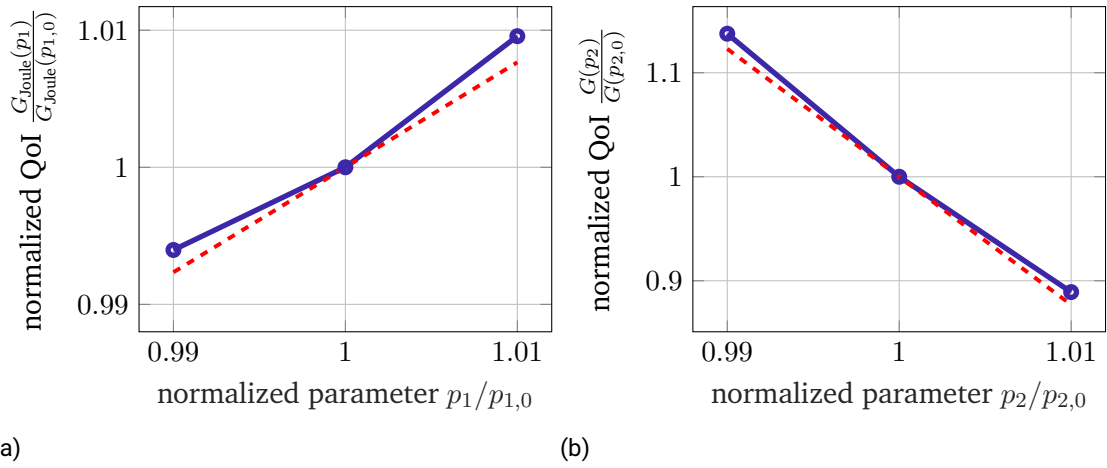
Figure 6.4: The QoI, i.e. the Joule heat, for different values of (ab) p_1 and (b) p_2. The red lines indicate the slope of the tangents as computed by the AVM.
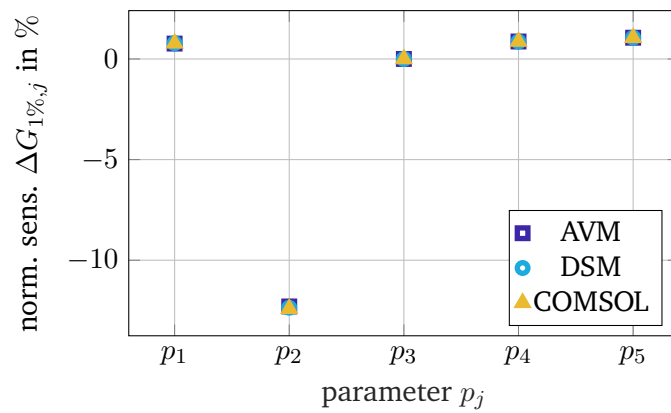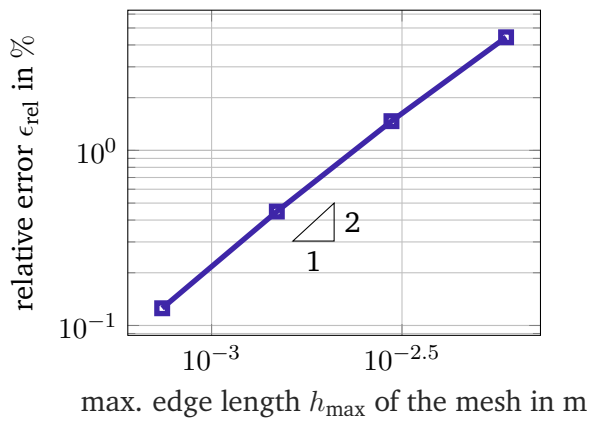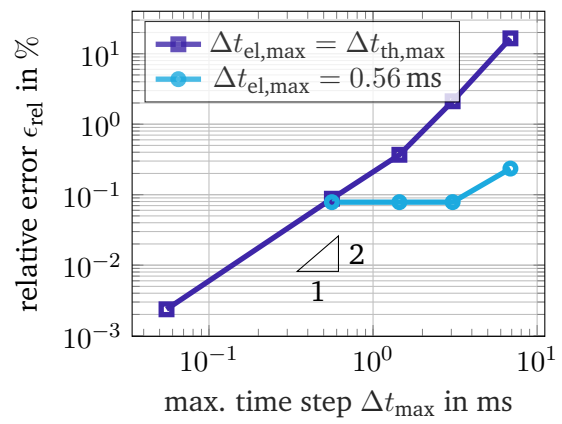

Figure 6.5: Comparison of the sensitivities of the Joule heat computed by the AVM and the reference solutions, respectively.

(a)

(b)

Figure 6.6: Convergence of the sensitivity $\frac{\mathrm{d}G}{\mathrm{d}p_2}$ of the Joule heat to p_2 with respect to (a) the mesh size and (b) the time step size.

7 Parameter Identification from Measurement Data

The accuracy and predictive capabilities of a simulation depend significantly on the quality of its model parameters, which are often not precisely known. This chapter illustrates how simulations can estimate unknown material parameters from measurement data using an inverse problem approach [53, 54]. This study utilizes code originally developed for parameter identification in electrical machines [55], which has been adapted for use with HVDC cable joints.

7.1 Model Formulation

In this study, the thermal conductivities of the 320 kV cable joint specimen presented in Ch. 3 are estimated using temperature measurements.

Firstly, a mathematical model of the cable joint is formulated dependent on the parameters to be estimated, namely the thermal conductivities, $\boldsymbol{\lambda}$. The thermal steady-state of the cable joint is described by the static heat conduction equation (4.3), which is considered in a 2D axisymmetric FE simulation (see (4.8)).

Secondly, measurement data capturing the relevant aspects of the systems behavior are collected. Since no experimental data is available, mock-up measurement data is generated by a forward thermal steady-state simulation of the cable joint to which a synthetic noise is added [55], i.e.,

$$\boldsymbol{\theta}_{\mathrm{meas}} = \boldsymbol{\theta}_{\mathrm{sim}}(\boldsymbol{\lambda}_{\mathrm{exact}}) + \eta\,, \tag{7.1}$$

where $\boldsymbol{\theta}_{\mathrm{sim}} = [\theta_{\mathrm{sim},1}, ..., \theta_{\mathrm{sim},N_{\mathrm{meas}}}]$ represents the temperatures obtained by a forward simulation, $\boldsymbol{\lambda}_{\mathrm{exact}}$ are the thermal conductivities of the forward simulation, and $\eta(0, \sigma_\eta)$ is a standard-distributed noise with a standard deviation of σ_η. A purely thermal experimental setup is selected, assuming a constant conductor temperature of 65°C and an ambient temperature of 20°C, no voltage is applied to the joint.

Lastly, the inverse problem is defined as a least square optimization problem [55],

$$\operatorname*{argmin}_{\boldsymbol{\lambda}} \sum_{i=0}^{N_{\mathrm{meas}}} (\theta_{\mathrm{meas},i} - \theta_{\mathrm{sim},i}(\boldsymbol{\lambda}))^2, \qquad (7.2)$$

aiming to minimize the difference between measured and simulated temperatures. Both the forward and inverse problem are implemented and solved within the FE framework *Pyrit*. The optimization problem (7.2) is solved using the "scipy"-library with the default optimizing method L-BFGS-B. An initial guess of 1 W/(m·K) is assumed for all thermal conductivities. The optimization problem is bounded to search for thermal conductivities between 0.01 W/(m·K) and 20 W/(m·K).

7.2 Noise-Free Virtual Measurements at all Mesh Nodes

Table 7.1: Exact thermal conductivities of the forward problem.

Material	Symbol	Thermal Conductivity in W/(m·K)
FGM	λ_{FGM}	0.5
XLPE	λ_{XLPE}	0.3
insulating SiR	$\lambda_{\mathrm{SiR,\ insul.}}$	0.22
conductive SiR	$\lambda_{\mathrm{SiR,\ cond.}}$	0.25
housing	$\lambda_{\mathrm{housing}}$	0.25
soil	λ_{soil}	0.79
sand	λ_{sand}	0.54

In a first step, it is verified that the inverse problem is able to correctly recover the thermal conductivities if the temperature solution of the forward simulation is available at every node of the FE mesh and no noise is added. The exact thermal conductivities, $\boldsymbol{\lambda}_{\text{exact}}$, of the forward problem are listed in Table 7.1.

In [56], it was demonstrated that in a purely thermal setting, the solution of the inverse problem lacks uniqueness, with thermal conductivities recoverable only up to a factor. Two solutions address this issue. One introduces additional source terms in the form of Joule heating, i.e. by choosing an electrothermal steady-state setting. The other fixes one or more thermal conductivities beforehand. Both approaches are able to recover the thermal conductivities perfectly. Since the latter approach is computationally more efficient, in the following the thermal conductivities of the FGM, XLPE and insulating SiR will be estimated while the others are provided as input in the simulation.
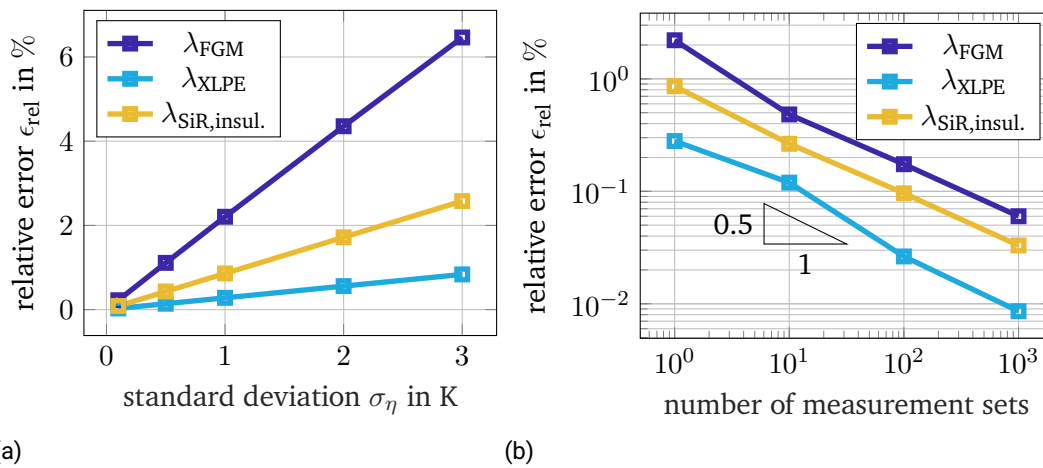

(a) (b)

Figure 7.1: Relative error, ϵ_{rel}, in % for (a) different standard deviations, σ_η, and (b) different numbers of measurement sets. In (b), a standard deviation of $\sigma_\eta = 1\,\text{K}$ has been adopted.

7.3 Noisy Virtual Measurements at all Mesh Nodes

It is investigated how noise influences the estimation of the thermal conductivities. Figure 7.1a shows the relative error,

$$\epsilon_{\text{rel}} = \frac{|\lambda_{\text{est}} - \lambda_{\text{exact}}|}{\lambda_{\text{exact}}}, \tag{7.3}$$

of the estimated thermal conductivities, $\boldsymbol{\lambda}_{\text{est}}$, for standard deviations ranging from $0.1\,\text{K}$ to $3\,\text{K}$. A standard deviation of $3\,\text{K}$ means that according to the $2\sigma_\eta$-interval, $95.45\,\%$ of the measurement data have a deviation of $6\,\text{K}$ or less. To increase the level of randomness, the parameter estimation has been repeated using ten different random seeds for the noise generation after which the results have been averaged. For all three parameters a linear increase of the relative error with respect to the standard deviation can be observed. Figure 7.1a furthermore shows that not all parameters are estimated equally well. This is due to the fact that the quality of a parameter destination depends on the sensitivity of the measurement data to the estimated parameter [56]. Figure 7.2 illustrates that the temperature inside the cable joint is much more sensitive towards λ_{XLPE} and $\lambda_{\text{SiR,insul.}}$ compared to λ_{FGM}. Figure 7.1b shows that the quality of the estimation can be improved and the influence of the noise reduced by conducting multiple sets of measurements. It shows the convergence of the relative error of an estimation with a standard deviation of $\sigma_\nu = 1\,\text{K}$ with respect to an increasing number of measurement sets. A convergence order of 0.5 with respect to the number of measurement sets is observed, which is in agreement with the results of [56]. Naturally, one thousand measurement sets are unrealistic in an experimental setting. However, even by conducting ten sets of measurements, a relative error below one percent can be achieved for all estimated thermal conductivities.
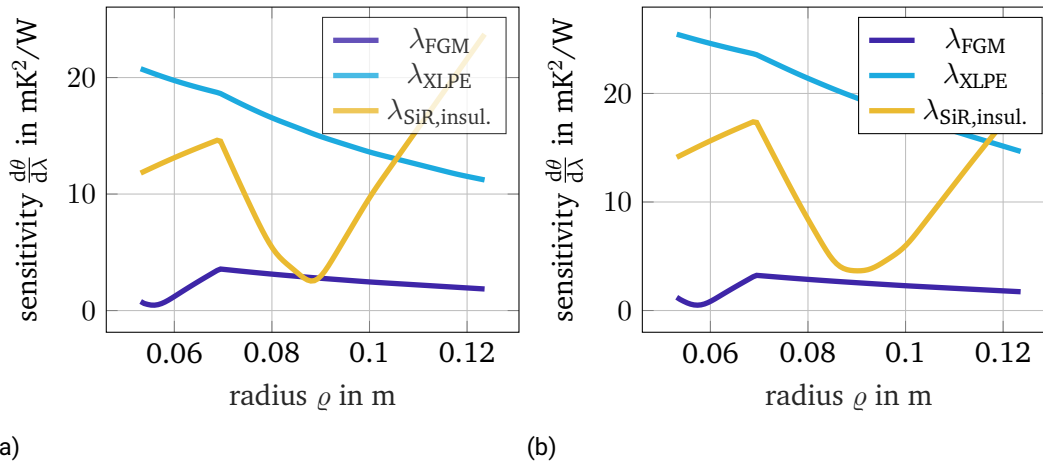
Figure 7.2: Sensitivity of the temperature to the different thermal conductivities inside the insulation materials of the cable joint at (a) $z = 0.2\,\text{m}$ and (b) $z = 0.4\,\text{m}$.

7.4 Virtual Measurements at Selected Positions

Since experimental data are often only available at a few sensor positions, the parameter estimation is now performed using 17 artificial measurement data points. The positions of the data points are illustrated in Fig. 7.3. Again, after successfully confirming that the correct thermal conductivities are recovered for noise free measurement data, the influence of noise corruption is investigated. Figure 7.4a shows that, due to the small number of measurement samples, the relative error now strongly depends on the standard deviation. A standard deviation of $1\,\text{K}$ leads to a relative error of $30\,\%$ of the FGM's thermal conductivity. The estimation can be improved by either inserting more sensors and thereby increasing the size of the measurement data or, again, by conducting multiple sets of measurements. Figure 7.4b shows the convergence of the relative error with respect to the number of measurement sets. A convergence rate of 0.5 is observed and it can be seen that by conducting ten sets of measurement sets the relative error of the FGM's thermal conductivity can be effectively reduced from $30\,\%$ to $6\,\%$.
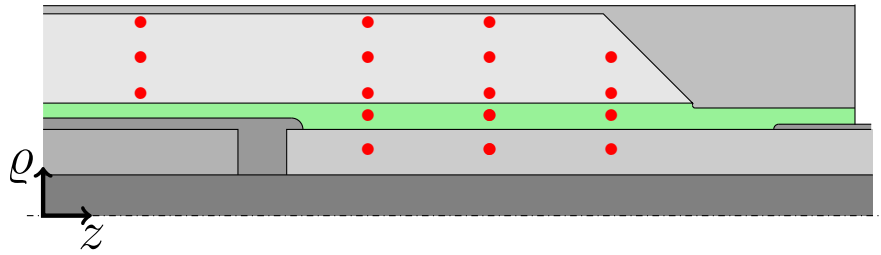
Figure 7.3: Positions of the artificial measurement data points used for the inverse problem in Sec. 7.4.

7.5 Conclusion

This study has demonstrated the effectiveness of inverse problem solving in recovering unknown material properties from experimental data. It highlights the critical role played by the quality of the measurement data for accurately estimating parameters. Factors such as measurement sensitivity, the number of data points, and noise corruption significantly influence the estimation process.

The methodology presented here offers a flexible approach suitable for investigating various parameters defining cable joint problems across different operational scenarios.
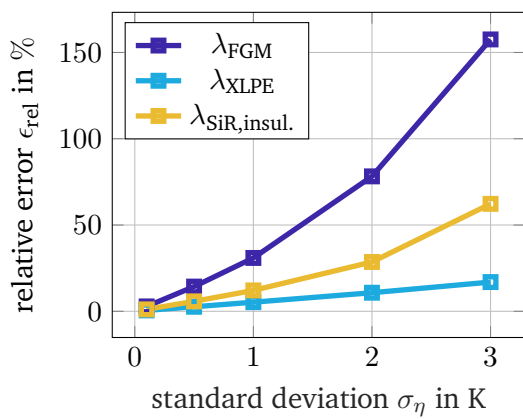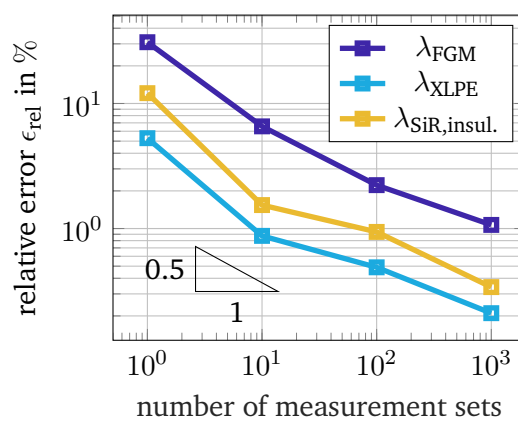
Figure 7.4: Relative error, ϵ_{rel}, in % for (a) different standard deviations, σ_η, and (b) different numbers of measurement sets. In (b), a standard deviation of $\sigma_\eta = 1\,\text{K}$ has been adopted.

8 Simulation of Slow Polarization Processes

In HVDC cable joints, slow polarization phenomena play a more pronounced role compared to HVAC systems due to the prolonged exposure to a unidirectional electric field [57]. Standard EQS or electroquasistatic-thermal (EQST) simulations of HVDC insulation systems typically account for fast polarization processes through the relative permittivity but may not fully capture slower polarization effects.

This chapter reviews various modeling and simulation approaches for slow polarization processes in time-domain, focusing on their applicability to HVDC cable joints. By presenting and comparing different methodologies from the literature, this chapter aims to enhance the accuracy of simulations and analyses for HVDC insulation systems.

8.1 Background on Polarization

Dielectric polarization is a phenomenon that occurs in insulating materials (dielectrics) when they are subjected to an external electric field. It refers to the alignment of atoms or molecules or the separation of positive and negative charge carriers according to an applied electric field [58]. The polarization caused by the external electric field, $\boldsymbol{E}_{\text{ext}}$, generates an electric field, $\boldsymbol{E}_{\text{P}}$, which is superimposed on the external field. The total electric field $\boldsymbol{E}$ then results in

$$\boldsymbol{E} = \boldsymbol{E}_{\text{ext}} + \boldsymbol{E}_{\text{P}} \, . \tag{8.1}$$

A distinction can be made between several polarization mechanisms [5]:

- Deformation polarization refers to the displacement of an atom's electron shell or charged atoms within a molecule in response to an external electric field (see Fig. 8.1a).

- During lattice polarization, the charged lattice elements are displaced in the crystal lattice. Dipoles are formed within the lattice, which are aligned with the external field (see Fig. 8.1b).

- In orientation polarization, charged molecular groups are aligned under the action of an external electric field (see Fig. 8.1c).

- During interfacial polarization, charge carriers accumulate at the interfaces between substances of different conductivity. These align themselves against the external electric field (see Fig. 8.1c)[57].

(a) Deformation polarization.

(b) Lattice polarization.

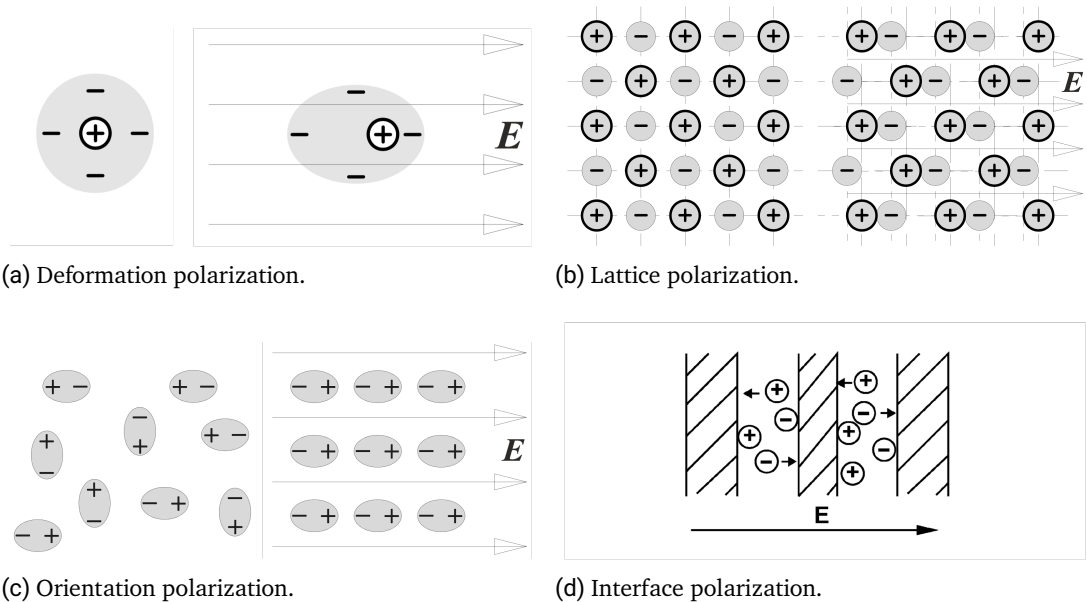(c) Orientation polarization.

(d) Interface polarization.

Figure 8.1: Overview of different polarization mechanisms. Figures (a)-(c) are adapted from [5], and figure (d) is adapted from [59].

Since the polarization mechanisms do not only occur individually, but often simultaneously, the total polarizability of a material can be seen as the sum of all processes [58]. The occurrence of individual polarization mechanisms depends on the frequency of the excitation. At low frequencies, the material's polarization processes have sufficient time to respond to the changing electric field. However, as the frequency increases, the polarization mechanisms within the material cannot keep pace with the rapidly oscillating electric field. This can be interpreted as a frequency dependent relative permittivity and is illustrated in Fig. 8.2. Therefore, in the presence of a DC excitation, all polarization mechanisms need to be considered.

In addition to its frequency dependence, polarization also varies with temperature [5]. The temperature dependence is primarily due to orientation polarization. At higher temperatures, dipoles become more mobile, which facilitates orientation polarization (see Fig. 8.3). Additionally, increased temperature can lead to changes in conductivities and the initiation of interfacial polarization mechanisms. The presence of temperature gradients in HVDC cable joints, hence, motivates a coupled electrothermal simulation approach.
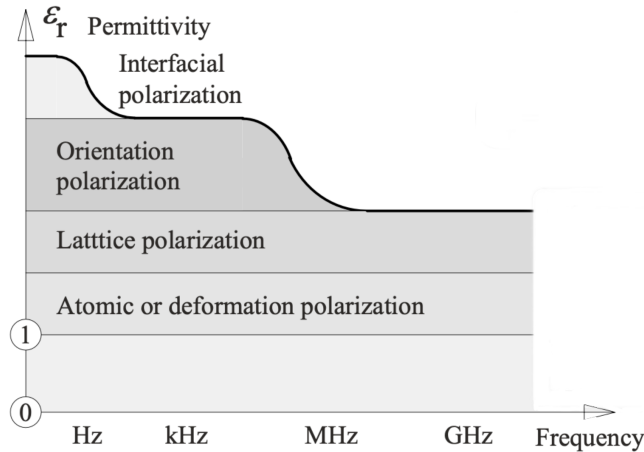
Figure 8.2: Frequency dependence of the relative permittivity. (Figure taken from [5])
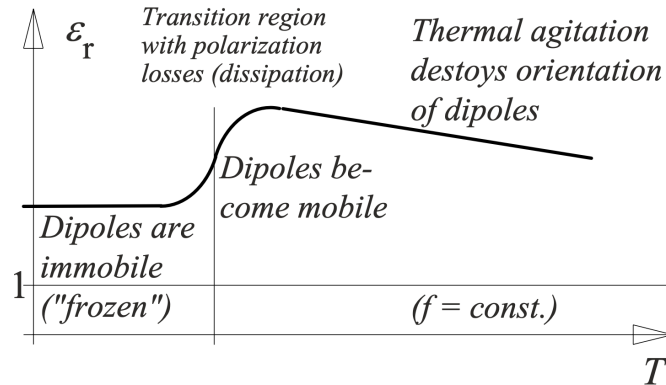
Figure 8.3: Illustration of the temperature dependence of dipole polarization. (Figure taken from [5], here T denotes the temperature and f the frequency.)

8.2 Modeling Approaches

As described in Ch. 5, the transient electric behavior of HVDC equipment is conventionally described by the transient EQS equation (5.1). The EQS equation can also be expressed as

$$\operatorname{div}(\boldsymbol{J}_{\text{tot}}) = 0\,, \tag{8.2}$$

where $\boldsymbol{J}_{\text{tot}}$ represents the total current density, which is composed of the conduction current density, $\boldsymbol{J}_{\text{C}}$, and the displacement current density, $\boldsymbol{J}_{\text{D}}$, i.e.

$$\boldsymbol{J}_{\text{tot}} = \boldsymbol{J}_{\text{C}} + \boldsymbol{J}_{\text{D}}\,. \tag{8.3}$$

The conduction current density arises from the movement of mobile charge carriers in the electric field and is described by the material law [5, p. 269]

$$\boldsymbol{J}_{\text{C}} = \sigma \boldsymbol{E}\,. \tag{8.4}$$

The displacement current density, $\boldsymbol{J}_{\text{D}}$, on the other hand, accounts for the current density due to transient polarization processes, i.e. the displacement of immobile positive and negative charge carriers relative to each other [5, p. 79]:

$$\boldsymbol{J}_{\text{D}} = \partial_t \boldsymbol{D} = \partial_t \left(\varepsilon_0 \boldsymbol{E} + \boldsymbol{P}\right)\,. \tag{8.5}$$

Here, ε_0 represents the vacuum permittivity, and $\boldsymbol{P}$ represents the dielectric polarization. The polarization is typically modeled by the relative permittivity , ε_r, i.e.,

$$\boldsymbol{D} = \varepsilon_0 \boldsymbol{E} + \boldsymbol{P} = \varepsilon_0 \varepsilon_r \boldsymbol{E} \,. \tag{8.6}$$

When a constant permittivity is assumed, typically determined at a frequency of 50 Hz, the absolute permittivity $\varepsilon = \varepsilon_0 \varepsilon_r$ often only reflects fast polarization processes, while neglecting slower polarization currents, such as those caused by the orientation of large molecules. Hence, the total current density is extended by a term, $\boldsymbol{J}_\mathrm{P}$, that represents slow polarization currents [57, p. 17], [60] i.e.,

$$\boldsymbol{J}_\mathrm{ext} = \boldsymbol{J}_\mathrm{C} + \boldsymbol{J}_\mathrm{D} + \boldsymbol{J}_\mathrm{P} \,. \tag{8.7}$$

In the following, several approaches for the modeling and simulation of the slow polarization currents, $\boldsymbol{J}_\mathrm{P}$, are discussed. In general, slow polarization phenomena can be modeled either by additional free charge densities or by bound charges. Free charges appear in Gauss' law as the charge density on the righthandside. Bound charges are not counted there, but are considered by adapting the relative permittivity. In both cases, the result for the electric field will remain the same, since it is directly related to the forces acting on electric charges. The different models will, however, exhibit different charge densities, different electric displacement fields and, obviously different permittivities.

8.2.1 Debye Approach and Network Model

For materials with linear polarization behavior, the transient polarization, $\boldsymbol{P}(t)$, is assumed to be the result of the linear superposition of all individual polarization processes, $\boldsymbol{P}_k(t)$ [5, p. 269]:

$$\boldsymbol{P}(t) = \sum_k^n \boldsymbol{P}_k(t) \,. \tag{8.8}$$

The Debye model assumes that the rate of change, $\partial_t \boldsymbol{P}_k(t)$, for each polarization process is proportional to the difference between $\boldsymbol{P}_k(t)$ and the steady-state end

value $\boldsymbol{P}_k(\infty)$, as expressed by the differential equation [61]:

$$\partial_t \boldsymbol{P}_k(t) = \frac{1}{\tau_k} \left(\boldsymbol{P}_k(\infty) - \boldsymbol{P}_k(t) \right) . \qquad (8.9)$$

This equation describes a polarization that decays exponentially with the time constant τ_k towards the steady-state value $\boldsymbol{P}_k(\infty)$:

$$\boldsymbol{P}_k(t) = \boldsymbol{P}_k(\infty) \left(1 - \exp\left(-\frac{t}{\tau_k} \right) \right) \qquad (8.10)$$

This transient behavior can also be represented by a network model as shown in Fig. 8.4 [62]. The initial displacement field due to the vacuum capacitance corresponds to charging the capacitor C_0, while the resistive steady-state corresponds to the steady-state conduction through the resistor R_∞. Dielectric properties for rapid transient or high-frequency loads are simplified using an RC-element. In this element, the geometric capacitance or high-frequency capacitance, $C_{\mathrm{Geo}} = \varepsilon_r C_0$, represents the relative permittivity ε_r, and the resistance $R_{\tan(\delta)}$ the corresponding losses, where $\tan(\delta)$ refers to the loss factor. The delayed exponential polarization processes described by (8.10) can then be modeled by additional RC-elements with the parameters R_k and C_k such that $\tau_k = R_k C_k$. This approach has been applied to HV bushings in [63] However, the representation of more complex insulation systems quickly leads to a prohibitively large computational effort [62].

8.2.2 Curie-von Schweidler Approach

The Curie-von Schweidler law is an empirical expression that characterizes the time-dependent response of a dielectric material to a step change in the electric field [64, pp. 1955-1960][65, p. 715 ff.]. According to the Curie-von Schweidler law, the slow depolarization current in a dielectric material after a constant field is abruptly turned off is described by a power function, i.e. [65]

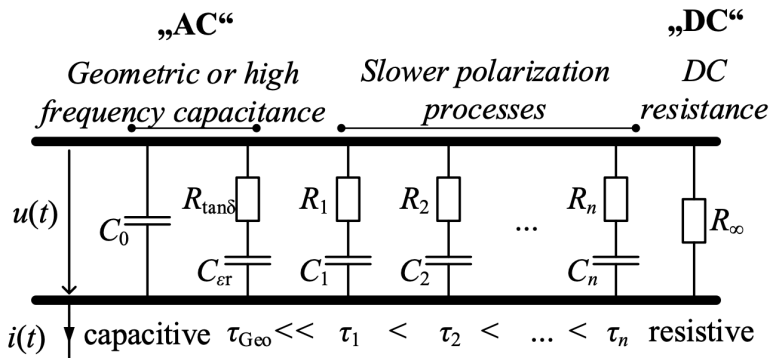$$\boldsymbol{J}_{\mathrm{P}}(t) \propto t^{-\beta} , \qquad (8.11)$$

Figure 8.4: Network model of a dielectric according to the Debye approach [62].

with the exponent $\beta \in [0, 1]$. Since the power law can be expressed as

$$t^{-\beta} = \frac{1}{\Gamma(\beta)} \int_0^\infty \tau^{-(\beta+1)} \exp\left(-\frac{t}{\tau}\right) \mathrm{d}\tau \,, \tag{8.12}$$

with the Gamma function $\Gamma(\beta)$, the Curie-von Schweidler law is often interpreted as the weighted sum of an infinite number of Debye functions [66]. The Curie-von Schweidler ansatz is implemented in FE simulations by defining an "effective" time-dependent electric conductivity [67, 68, 69, 70].

The Curie-von Schweidler's power law has the disadvantage that it is a purely empirical approach [64, pp. 1955-1960]. Although it can be interpreted as a superposition of many polarization mechanisms according to Debye, a specific physical interpretation is missing. An polarization behavior according to Curie-von Schweidler's power law can be observed approximately for many solids, but lacks a general validity. Furthermore, this approach lacks a storage term for charges [60]. This means that the charge stored in the dielectric material caused by polarization is not taken into account. In some cases, the solutions deviate substantially from the Debye theory [64, pp. 1956].

8.2.3 Poisson-Nernst-Planck Equation

In the case of charge carrier transport processes inside liquid media, it is also possible to describe the movement by diffusion, drift and displacement current density using the Poisson-Nernst-Planck (PNP) equation [71]. The total current density is described by the terms of the fast polarization ("displacement"), the conduction current ("drift") and by charge carrier gradients ("diffusion"),

$$
\boldsymbol{J}(t) = \underbrace{\sum_i z_i e \mu_i \boldsymbol{E}(t)}_{\text{Drift current density}} + \underbrace{\sum_i z_i e D_i \operatorname{grad}(n_i(t))}_{\text{Diffusion current density}} + \underbrace{\varepsilon \partial_t \boldsymbol{E}(t)}_{\text{Displacement current density}} \quad . \quad (8.13)
$$

Here, z_i corresponds to the valence of the i-th charge carrier species, μ_i to the mobility and n_i to the particle density. The diffusion coefficient of the i-th charge carrier species is denoted as D_i. The slow polarization mechanisms are not taken into account by (8.13) [71].

Since the PNP modeling approach only describes the charge carrier transport in liquid media and does not consider slow polarization processes, it is not suitable for the modeling of slow polarization processes in HVDC cable joints. Furthermore, while the PNP modeling approach has been successfully applied to simple one-dimensional (1D) and 2D objects, its extension to complex geometries of high-voltage components is currently hindered by computational limitations [71]. Another challenge lies in the determination of material parameters, including the mobility μ_i and diffusivity D_i [71, 60].

8.2.4 Debye-FEM Approach

As outlined in Section 8.2.1, the use of network elements is common in calculations aiming to capture polarization effects in accordance with the physically motivated Debye approach. However, the network-based approach encounters challenges in efficiently discretizing complex insulation systems. To address this limitation, [62] and [60] propose a hybrid methodology combining the Debye approach with the

FEM for a more adaptable spatial discretization. In this approach, the necessary differential equations are set up and implemented directly in the FEM.

According to (8.8), the transient polarization is a linear superposition of all individual polarization processes. Hence, $\boldsymbol{J}_\mathrm{P}$ in (8.7) can be written as the sum of n current densities, which represent the different polarization mechanisms or different RC-elements, respectively, i.e.,

$$\boldsymbol{J}_\mathrm{P} = \sum_{k=1}^{n} \boldsymbol{J}_k \,. \tag{8.14}$$

Based on a one-dimensional model of an infinitesimal RC-element, [62] derives a differential equation for the polarization current density corresponding to the k-th polarization process, $\boldsymbol{J}_k$, i.e.,

$$\partial_t \boldsymbol{E} = \frac{1}{\sigma_k} \partial_t \boldsymbol{J}_k + \frac{1}{\varepsilon_k} \boldsymbol{J}_k \,. \tag{8.15}$$

Here, the quantities σ_k and ε_k are material data that are obtained by curve fitting Polarization-Depolarization-Current (PDC) measurements [60, p. 54]. Equation (8.15) yields n differential equations that must be solved in addition to the EQS formulation,

$$\mathrm{div}\left(\boldsymbol{J}_\mathrm{C} + \boldsymbol{J}_\mathrm{D} + \sum_{k}^{n} \boldsymbol{J}_k \right) = 0 \,, \tag{8.16}$$

with regard to the unknowns $\boldsymbol{E}$, $\boldsymbol{J}_1$ to $\boldsymbol{J}_n$.

The system of PDEs comprised of (8.15) and (8.16) can be directly implemented into the FEM. For this purpose, the scalar potential and the polarization current densities are discretized using linear nodal shape functions, $N(\boldsymbol{r})$, and Raviart-Thomas shape functions [72], $\boldsymbol{z}_q$, respectively, i.e.,

$$\phi(\boldsymbol{r}, t) \approx \sum_{i=1}^{N_\mathrm{node}} u_i(t) N_i(\boldsymbol{r}) \,, \tag{8.17}$$

$$\boldsymbol{J}_k(\boldsymbol{r}, t) \approx \sum_{q=1}^{N_\mathrm{edge}} v_{k,q}(t) \boldsymbol{z}_q(\boldsymbol{r}) \,. \tag{8.18}$$

Here, N_node and N_edge denote the number of mesh nodes and mesh edges, respectively. Raviart-Thomas shape functions are associated with the edges of the FE mesh and ensure normal continuity of the polarization current densities [72]. The semi-discrete version of the PDEs system is then obtained by a weighted residual approach using linear nodal shape functions for testing (8.16) and Raviart-Thomas shape functions for testing (8.15). The semi-discrete system reads:

$$\boldsymbol{K}_\sigma \boldsymbol{u} + \boldsymbol{K}_\varepsilon \partial_t \boldsymbol{u} + \sum_{k=1}^n \boldsymbol{X} \boldsymbol{v}_k = \boldsymbol{0}\,, \tag{8.19}$$

$$\boldsymbol{X}^T \boldsymbol{u} + \boldsymbol{B}_{\frac{1}{\sigma_k}} \partial_t \boldsymbol{v}_k + \boldsymbol{B}_{\frac{1}{\varepsilon_k}} \boldsymbol{v}_k = 0\,, \tag{8.20}$$

with

$$\boldsymbol{X}_{iq} = -\int_\Omega \boldsymbol{z}_q \cdot \operatorname{grad}\left(N_i\right) \mathrm{d}V\,, \tag{8.21}$$

$$\boldsymbol{B}_{(\cdot),pq} = \int_\Omega (\cdot)\boldsymbol{z}_p \cdot \boldsymbol{z}_q \,\mathrm{d}V\,. \tag{8.22}$$

8.2.5 Summary

In summary, both the Curie-von Schweidler approach as well as the Debye-FEM approach are promising methods for modeling slow polarization within a finite element setting. The Debye-FEM approach appeals through its physical motivation, while the Curie-von Schweidler approach is of heuristic nature. Nevertheless, according to [73], in scenarios involving polarization processes with varying time constants, the Debye approach may simplify and overlook memory effects. Both methods can be implemented efficiently into the FEM. The implementation of a time-dependent conductivity, as seen in the Curie-von Schweidler approach, proves more straightforward compared to the discretization of the additional differential equation inherent to the Debye approach.

9 Conclusion and Outlook

9.1 Conclusion

Germany's Energiewende initiative underscores the country's critical transition to green energy, pivotal for combating climate change and achieving sustainable energy independence. Emphasizing substantial increases in renewable energy production, particularly from wind energy in the northern region, this strategy necessitates the development of new transmission infrastructure, including High-Voltage Direct Current (HVDC) technology, for efficient long-distance power transportation.

A key decision in this transition was the prioritization of underground HVDC cable systems over overhead lines, driven by public resistance and aesthetic concerns. Cable joints, being the most vulnerable components due to factors such as installation errors and electric field stresses, are integral to the overall reliability of the transmission network.

This dissertation aims to support the advancement of future cable joint technology by developing simulation tools tailored for joint design and analysis.

The dissertation began with a discussion on the electrothermal modeling of HVDC cable joints during both steady-state and transient operations. A freely-available electrothermal solver was implemented in the Python-based finite element framework *Pyrit* , specifically tailored for HVDC cable joint simulation. This solver successfully addressed numerical challenges inherent in cable joints, including strong field- and temperature-dependent material properties, and the multi-rate nature of the transient electrothermal problem. The solver's accuracy

was validated against commercial software using a 320 kV HVDC cable joint specimen as a lead example, with brief electrothermal analyses conducted during both steady-state operation and transient switching impulse operation.

The dissertation then focused on the development of simulation tools for the efficient computation of sensitivities. Sensitivities, which quantify how a quantity of interest is influenced by small changes in a design parameter, play a vital role in the design and optimization of HVDC cable joints. Two complementary methods for sensitivity computation were implemented within the *Pyrit* framework: The direct sensitivity method, which scales with the number of investigated design parameters, and the adjoint variable method, which scales with the number of investigated quantities of interest but is independent of the number of design parameters. The derivation of the adjoint variable method for transient electroquasistatic-thermal problems represented the main contribution of this thesis.

Furthermore, the dissertation demonstrated how simulation could estimate model parameters from experimental data using an inverse problem approach. It highlighted the critical role of measurement data quality in accurately estimating parameters and discussed the influence of factors such as measurement sensitivity, the number of data points, and noise corruption on the estimation process.

Finally, the dissertation provided a comprehensive literature review on modeling and simulation approaches for slow polarization processes in HVDC cable joints. This chapter reviewed various methodologies from the literature, aiming to enhance the accuracy of simulations and analyses for HVDC insulation systems exposed to prolonged unidirectional electric fields.

This dissertation developed several tools for the design and optimization of HVDC cable joints, supporting the goal of advancing simulation-aided design methods to improve joint reliability and performance.

9.2 Outlook

Future research may expand the existing simulation toolbox to further advance simulation-aided design and investigation of HVDC cable joints.

One example is the implementation of tools for building surrogate models that relate crucial quantities of interest to influential design parameters. The aim is to achieve a good compromise between the surrogate's size and its accuracy. To cope with the large number of important design parameters, adaptive sparse polynomial interpolation techniques [74] may be applied. These surrogate models might be offered as a graphical user interface with sliders, serving as rapid evaluation tools to support experimental work and catalyze scientific insights. They could enable quick extraction of material data from macroscopic measurements and expedite uncertainty quantification and optimization processes.

Furthermore, variable material parameters and manufacturing tolerances indicate the need for uncertainty quantification focused on critical parameters. To reduce the number of costly transient FE simulations, uncertainty quantifications are preferably carried out on the surrogate models. Uncertainty quantification enables robust optimization and thereby enhances the reliability and efficiency of HVDC cable joints.

To improve the understanding of the transient behavior of HVDC cable joints, the existing solver should be extended to account for slow polarization processes into the existing electrothermal solver and the results validated against measurement data. Integrating these processes into the solver could improve simulation accuracy and provide a more realistic assessment of joint performance over extended operational lifetimes.

The overall aim being the simulation-aided design of HVDC cable joints, the developed tools should be applied to deepen the understanding of electrothermal joint behavior, planning measurement campaigns and exploring novel cable joint configurations ensuring robust performance and reliability under diverse operational conditions.

Bibliography

[1] Bundesregierung. *Mehr Energie aus erneuerbaren Quellen*. URL: https://www.bundesregierung.de/breg-de/schwerpunkte/klimaschutz/energiewende-beschleunigen-2040310#:~:text=Um%20die%20Klimaschutzziele%20zu%20erreichen%2C%20muss%20der%20Ausbau%20der%20Erneuerbaren,waren%20es%2046%2C2%20Prozent. (visited on 06/25/2024).

[2] A. Abuzayed and N. Hartmann. "Triggering Germany's ambitious dream of a completely renewable electricity sector by 2035". In: *2022 International Conference on Renewable Energies and Smart Technologies (REST)*. Vol. I. 2022, pp. 1–4. DOI: 10.1109/REST54687.2022.10022950.

[3] H. Ghorbani, M. Jeroense, C.-O. Olsson, and M. Saltzer. "HVDC cable systems – highlighting extruded technology". In: *IEEE Trans. Power Deliv.* 29.1 (2014), pp. 414–421. DOI: 10.1109/TPWRD.2013.2278717.

[4] Siemens Energy. *Windstromleitung SuedLink wird mit HGÜ-Technologie von Siemens Energy ausgestattet*. URL: https://www.siemens-energy.com/de/de/home/pressemitteilungen/windstromleitung-suedlink-wird-mit-hgue-technologie-von-siemens-energy-ausgestattet.html (visited on 06/24/2024).

[5] A. Küchler. *High Voltage Engineering: Fundamentals - Technology - Applications*. 1st ed. VDI-Buch. Berlin, Heidelberg, 2018. DOI: 10.1007/978-3-642-11993-4.

[6] C. Jörgens and M. Clemens. "A review about the modeling and simulation of electro-quasistatic fields in HVDC cable systems". In: *Energies* 13.19 (Oct. 2020), p. 5189. DOI: 10.3390/en13195189.

[7] Bundesamt für Justiz. *Gesetz über den Bundesbedarfsplan (Bundesbedarfsplangesetz - BBPlG) § 3 Erdkabel für Leitungen zur Höchstspannungs-Gleichstrom-Übertragung*. URL: https://www.gesetze-im-internet.de/bbplg/__3.html (visited on 06/24/2024).

[8] Tennet. *Freileitung und Erdkabel*. URL: https://infomarkt.tennet.eu/pirach-pleinting/freileitung-und-erdkabel#:~:text=Freileitungen%20halten%20zudem%20etwa%2080,nur%20in%20wenigen%20Pilotprojekten%20vorgesehen. (visited on 06/24/2024).

[9] G. Chen, M. Hao, Z. Xu, A. Vaughan, J. Cao, and H. Wang. "Review of high voltage direct current cables". In: *CSEE J. Power Energy Syst.* 1.2 (July 24, 2015), pp. 9–21. DOI: 10.17775/CSEEJPES.2015.00015.

[10]   Cigré Working Group B1.32. *Recommendations for Testing DC Extruded Cable Systems for Power Transmission at a Rated Voltage up to 500 kV*. Technical Brochure TB496. Conseil international des grands réseaux électriques, 2012.

[11]   Cigré Working Group D1.56. *Field grading in electrical insulation systems*. Technical Brochure TB794. Conseil international des grands réseaux électriques, 2020.

[12]   R. Hussain and V. Hinrichsen. "Simulation of thermal behavior of a 320 kV HVDC cable joint with nonlinear resistive field grading under impulse voltage stress". In: *CIGRÉ Winnipeg 2017 Colloquium*. 2017.

[13]   Clean Energy Wire. *Set-up and challenges of Germany's power grid*. URL: https://www.cleanenergywire.org/factsheets/set-and-challenges-germanys-power-grid (visited on 06/24/2024).

[14]   Cigré Working Group B1.10. *Update of Service Experience of HV Underground and Submarine Cable Systems*. Technical Brochure TB379. Conseil international des grands réseaux électriques, 2009.

[15]   G. Mazzanti and M. Marzinotto. *Extruded cables for high-voltage direct-current transmission : advances in research and development*. Piscataway, NJ Hoboken, NJ: IEEE Press Wiley, 2013.

[16]   Bundesnetzagentur. *Netzausbau – Erdkabel*. URL: https://www.netzausbau.de/SharedDocs/Downloads/DE/Infomaterial/BroschuereErdkabel.pdf?__blob=publicationFile (visited on 10/06/2023).

[17]   B. Bayern. *HGÜ-Erdkabel müssen jetzt schnell realisiert werden*. URL: https://www.bauindustrie-bayern.de/themen/energie-und-versorgung/hgue-erdkabel-muessen-jetzt-schnell-realisiert-werden (visited on 06/24/2024).

[18]   Insight - Prysmian Magazine. URL: https://www.prysmian.com/en/insight/projects/innovation-as-the-cornerstone-of-prysmian-group-business-strategy (visited on 06/24/2024).

[19]   J. Bundschuh, M. G. Ruppert, and Y. Späck-Leigsnering. "Pyrit: A finite element based field simulation software written in Python". In: *COMPEL* (Sept. 28, 2023). DOI: 10.1108/compel-01-2023-0013.

[20]   M. G. Ruppert, Y. Späck-Leigsnering, H. De Gersem, and M. Koch. "Analyzing Sensitivities in HVDC Cable Joint Materials". In: *Jicable'23: 11th International Conference on Insulated Power Cables* (Lyon). June 2023.

[21]   M. G. Ruppert, Y. Späck-Leigsnering, J. Buschbaum, and H. De Gersem. "Adjoint Variable Method for Transient Nonlinear Electroquasistatic Problems". In: *Electr. Eng.* 105 (Apr. 1, 2023), pp. 2319–2325. DOI: 10.1007/s00202-023-01797-4.

[22]   M. G. Ruppert, Y. Späck-Leigsnering, and H. De Gersem. "Transient Nonlinear Electrothermal Adjoint Sensitivity Analysis for HVDC Cable Joints". In: *International Journal of Numerical Modelling: Electronic Networks, Devices and Fields* (May 2024). Submitted.

[23]   H. Ye et al. "Review on HVDC cable terminations". In: *High Voltage* 3.2 (Apr. 2018), pp. 79–89. DOI: 10.1049/hve.2017.0144.

[24] D. Fabiani et al. "Polymeric HVDC cable design and space charge accumulation. Part 1: Insulation/semicon interface". In: *IEEE Electr. Insul. Mag.* 23.6 (Nov. 2007), pp. 11–19. DOI: 10.1109/MEI.2007.4389975.

[25] S. Delpino et al. "Polymeric HVDC cable design and space charge accumulation. Part 2: Insulation interfaces". In: *IEEE Electr. Insul. Mag.* 24.1 (Jan. 2008), pp. 14–24. DOI: 10.1109/MEI.2008.4455499.

[26] M. Kahle. *Elektrische Isoliertechnik*. Springer Berlin Heidelberg, Apr. 1989. 360 pp.

[27] S. Qin and S. Boggs. "Design considerations for high voltage DC components". In: *IEEE Electr. Insul. Mag.* 28.6 (Nov. 12, 2012), pp. 36–44. DOI: 10.1109/MEI.2012.6340523.

[28] H. Ye et al. "Design aspects on HVDC cable joints". In: *12th International Conference on the Properties and Applications of Dielectric Materials (ICPADM)*. 2018, pp. 300–304. DOI: 10.1109/ICPADM.2018.8401269.

[29] G. Mazzanti et al. "The insulation of HVDC extruded cable system joints. Part 1: Review of materials, design and testing procedures". In: *IEEE Trans. Dielectr. Electr. Insul.* 26.3 (June 2019), pp. 964–972. DOI: 10.1109/tdei.2019.007916.

[30] T. Tanaka, M. Kozako, N. Fuse, and Y. Ohki. "Proposal of a multi-core model for polymer nanocomposite dielectrics". In: *IEEE Transactions on Dielectrics and Electrical Insulation* 12.4 (Aug. 2005), pp. 669–681. DOI: 10.1109/TDEI.2005.1511092.

[31] T. J. Lewis. "Nano-composite dielectrics: The dielectric nature of the nano-particle environment". In: *IEEE Transactions on Fundamentals and Materials* 126.11 (2006), pp. 1020–1030. DOI: 10.1541/ieejfms.126.1020.

[32] S. Rätzke and J. Kindersberger. "The effect of interphase structures in nanodielectrics". In: *IEEE Transactions on Fundamentals and Materials* 126.11 (2006), pp. 1044–1049. DOI: 10.1541/ieejfms.126.1044.

[33] S. Azizi, E. David, M. F. Fréchette, and C. M. Ouellet-Plamondon. "Numerical simulation of the effective permittivity of low-density polyethylene composite filled by carbon black". In: *IET Nanodielectrics* 2.4 (July 26, 2019), pp. 129–134. DOI: 10.1049/iet-nde.2019.0017.

[34] S. Azizi, E. David, M. F. Fréchette, N.-T. Phuong, and C. M. Ouellet-Plamondon. "Electrical and thermal phenomena in low-density polyethylene/carbon black composites near the percolation threshold". In: *Journal of Applied Polymer Science* 136.6 (Dec. 28, 2018), p. 47043. DOI: 10.1002/app.47043.

[35] R. Hussain, O. Safarowsky, J. Hegge, and V. Hinrichsen. "Development of a liquid silicone rubber for the application in HVDC cable accessories". In: *Fachtagung Hochspannungstechnik 2020 (VDE ETG)*. Berlin, Germany, Nov. 2020, pp. 706–711.

[36] M. Secklehner, R. Hussain, and V. Hinrichsen. "Tailoring of new field grading materials for HVDC systems". In: *13th International Electrical Insulation Conference (INSUCON 2017)*. May 2017. DOI: 10.23919/insucon.2017.8097174.

[37] M. Koch, J. Hohloch, I. Wirth, S. Sturm, M. H. Zink, and A. Küchler. "Experimental and simulative analysis of the thermal behavior of high voltage cable joints". In: *VDE ETG – Fachtagung Hochspannungstechnik 2018*. Nov. 2018.

[38] Y. Späck-Leigsnering, G. Ruppert, E. Gjonaj, H. De Gersem, and M. Koch. "Towards Electrothermal Optimization of a HVDC Cable Joint Based on Field Simulation". In: *Energies* 14.10 (May 14, 2021), p. 2848. DOI: 10.3390/en14102848.

[39] M. G. Ruppert, Y. Späck-Leigsnering, J. Buschbaum, M. Koch, and H. De Gersem. "Efficient Sensitivity Calculation for Insulation Systems in HVDC Cable Joints". In: *27th Nordic Insulation Symposium on Materials, Components and Diagnostics* (Trondheim). June 2022.

[40] J.-M. Jin. *The Finite Element Method in Electromagnetics*. 3rd ed. Wiley, 2014.

[41] A. Bondeson, T. Rylander, and P. Ingelström. *Computational Electromagnetics*. Texts in Applied Mathematics. New York, NY, USA: Springer, 2005. DOI: 10.1007/b136922.

[42] M. Saltzer, T. Christen, T. Sörqvist, and M. Jeroense. "Electro-thermal simulations of HVDC cable joints". In: *Proceedings of the ETG Workshop Feldsteuernde Isoliersysteme*. Berlin, Offenbach: VDE-Verlag, Nov. 2011.

[43] Y. Späck-Leigsnering, E. Gjonaj, H. De Gersem, T. Weiland, M. Gießel, and V. Hinrichsen. "Multi-rate time integration for coupled electrical and thermal modeling of surge arresters". In: *2015 International Conference on Electromagnetics in Advanced Applications (ICEAA)*. Sept. 2015, pp. 264–267. DOI: 10.1109/ICEAA.2015.7297116.

[44] T. Schierz and M. Arnold. "Stabilized overlapping modular time integration of coupled differential-algebraic equations". In: *Applied Numerical Mathematics* 62 (Oct. 2012), pp. 1491–1502. DOI: 10.1016/j.apnum.2012.06.020.

[45] J. Bauer, A. Claudi, S. Kornhuber, S. Kühnel, J. Lambrecht, and S. Wels. "Silicon-Gel-Compound für die Nichtlinear-Resistive Feldsteuerung — zur Technischen Anwendung und Auslegung des Isoliersystems". In: *Fachtagung Hochspannungstechnik 2020 (VDE ETG)*. Berlin, Germany, Nov. 2020, pp. 163–168.

[46] I. G. Ion et al. "Deterministic Optimization Methods and Finite Element Analysis With Affine Decomposition and Design Elements". In: *Electr. Eng.* 100.4 (Dec. 2018), pp. 2635–2647. DOI: 10.1007/s00202-018-0716-6.

[47] N. Nikolova, J. Bandler, and M. Bakr. "Adjoint Techniques for Sensitivity Analysis in High-Frequency Structure CAD". In: *IEEE Trans. Microw. Theor. Tech.* 52.1 (Jan. 2004), pp. 403–419. DOI: 10.1109/tmtt.2003.820905.

[48] H. De Gersem, I. Munteanu, and T. Weiland. "Construction of Differential Material Matrices for the Orthogonal Finite-Integration Technique With Nonlinear Materials". In: *IEEE Trans. Magn.* 44.6 (June 2008), pp. 710–713. DOI: 10.1109/TMAG.2007.915819.

[49] Y. Cao, S. Li, L. Petzold, and R. Serban. "Adjoint sensitivity analysis for differential-algebraic equations: The adjoint DAE system and its numerical solution". In: *SIAM J. Sci. Comput.* 24.3 (2003), pp. 1076–1089. DOI: 10.1137/S1064827501380630.

[50] S. Li and L. Petzold. "Adjoint sensitivity analysis for time-dependent partial differential equations with adaptive mesh refinement". In: *J. Comp. Phys.* 198.1 (July 2004), pp. 310–325. DOI: 10.1016/j.jcp.2003.01.001.

[51] D. Zhang, F. Kasolis, and M. Clemens. "Topology Optimization for a Station Class Surge Arrester". In: *The 12th International Symposium on Electric and Magnetic Fields (EMF 2021)*. 2021.

[52] Y. Cao, S. Li, and L. Petzold. "Adjoint sensitivity analysis for differential-algebraic equations: algorithms and software". In: *J. Comput. Appl. Math.* 149.1 (Dec. 2002), pp. 171–191. DOI: 10.1016/s0377-0427(02)00528-9.

[53] B. v. Harrach. "An Introduction to Finite Element Methods for Inverse Coefficient Problems in Elliptic PDEs". In: *Jahresbericht der Deutschen Mathematiker-Vereinigung* 123.3 (2021), pp. 183–210. DOI: 10.1365/s13291-021-00236-2.

[54] A. Borzì and V. Schulz. *Computational Optimization of Systems Governed by Partial Differential Equations*. Society for Industrial and Applied Mathematics, 2011. DOI: 10.1137/1.9781611972054. eprint: https://epubs.siam.org/doi/pdf/10.1137/1.9781611972054.

[55] L. Blumrich et al. "Thermal Model Calibration of a Squirrel-Cage Induction Machine". In: *26th International Conference on Electrical Machines 2024* (Turin, Italy). Sept. 2024.

[56] L. Blumrich. "Electrothermal measurements and finite-element simulations of an induction machine". Master's Thesis. Darmstadt: Technische Universität Darmstadt, Nov. 2023. Submitted.

[57] B. Lutz. "Einflussfaktoren auf die elektrische Feldverteilung in Isoliersystemen mit polymeren Isolierstoffen bei Gleichspannungsbelastung". PhD thesis. Technische Universität München, 2011.

[58] K. C. Kao. *Dielectric Phenomena in Solids*. Elsevier Science, 2004.

[59] T. Dakin. "Conduction and polarization mechanisms and trends in dielectric". In: *IEEE Electrical Insulation Magazine* 22.5 (2006), pp. 11–28. DOI: 10.1109/MEI.2006.1705854.

[60] I. Wirth. "Berücksichtigung dielektrischer Materialeigenschaften in der Finite-Elemente-Simulation von HGÜ-Isoliersysteme". PhD Thesis. Ilmenau, Germany: Technische Universität Ilmenau, 2020.

[61] P. Debye. *Polar Molecules*. 1929.

[62] I. Wirth, M. H. Zink, A. Kuechler, F. Berger, and T. Schnitzler. "Implementation of conduction and polarization mechanisms in transient FEM simulations of HVDC insulation systems". In: *VDE High Voltage Technology 2018; ETG-Symposium*. 2018, pp. 1–6.

[63] M. H. Zink. "Zustandsbewertung betriebsgealterter Hochspannungstransformatordurchführungen mit Öl-Papier-Dielektrikum mittels dielektrischer Diagnose". PhD thesis. Ilmenau: Universitätsverlag Ilmenau, 2013.

[64]   T. C. Guo and W. W. Guo. "A transient-state theory of dielectric relaxation and the Curie-von Schweidler law". In: *Journal of Physics C: Solid State Physics* 16.10 (Apr. 1983), p. 1955. DOI: 10.1088/0022-3719/16/10/024.

[65]   E. R. v. Schweidler. "Studien über die Anomalien im Verhalten der Dielektrika". In: *Annalen der Physik* 329.14 (1907). DOI: https://doi.org/10.1002/andp.19073291407.

[66]   M. Hering, R. Gremaud, J. Speck, S. Großmann, and U. Riechert. "Flashover behaviour of insulators with inhomogeneous temperature distribution in gas insulated systems under DC voltage stress". In: *2014 ICHVE International Conference on High Voltage Engineering and Application*. 2014, pp. 1–4. DOI: 10.1109/ICHVE.2014.7035430.

[67]   M. Hering, Speck, K. Backhaus, S. Großmann, and U. Riechert. "Capacitive- resistive transition in gas insulated DC systems under the influence of particles on the insulator surface". In: *The 19th international Symposium on High Voltage Engineering*. Pilsen, Czech Republic, 2015, pp. 1–4. DOI: 10.1109/ICHVE.2014.7035430.

[68]   M. Hering. "Überschlagverhalten von Gas-Feststoff-Isoliersystemen unter Gleichspannungsbelastung". PhD thesis. Technische Universität Dresden, 2016.

[69]   R. Gremaud et al. "Solid Insulation in DC Gas-Insulated Systems". In: *CIGRE Paris*. 2014.

[70]   R. Gremaud et al. "Solid-gas insulation in HVDC gas-insulated system: Measurement, modeling and experimental validation for reliable operation". In: (2016).

[71]   K. Backhaus. "Das dielektrische Verhalten der Öl-Papier-Isolierung bei Belastung mit hoher Gleichspannung". PhD thesis. Technische Universität Dresden, 2016.

[72]   S. S. M. Rao, D. R. Wilton, and A. W. Glisson. "Electromagnetic scattering by surfaces of arbitrary shape". In: *IEEE Trans. Antennas Propag.* 30 (1982), 409–418. DOI: 10.1109/TAP.1982.1142818.

[73]   A. Pérez-Madrid, L. C. Lapas, and J. M. Rubí. 2017. DOI: doi:10.1515/zna-2016-0453.

[74]   D. Loukrezis and H. De Gersem. "Approximation and Uncertainty Quantification of Systems with Arbitrary Parameter Distributions using Weighted Leja Interpolation". In: *Algorithms* 13.51 (2020), pp. 1–15. DOI: 10.3390/a13030051. arXiv: 1904.07709.